Doctoral Dissertation

High-power solid-state lithium batteries with silica-gel solid nanocomposite electrolytes

ナノコンポジット固体電解質を用いた高出力全固体電池

Akihiko SAGARA

Graduate School of Materials Science,

Nara Institute of Science and Technology

September 2021

Table of contents

Chapter 1

General Introduction 6

1.1 Lithium-ion batteries (LIBs) 6

1.2 All-solid-state batteries (ASSBs) 8

1.3 Solid electrolytes (SEs) 9

1.4 Ionogels 11

1.5 Solid nanocomposite electrolytes (nano-SCEs) 13

1.6 Aims and outline of the thesis 19

Chapter 2

Pore structure analysis of ionic liquid-templated porous silica using positron annihilation lifetime spectroscopy 22

2.1 Introduction 22

2.2 Experimental 25

2.2.1 Sample preparation 25

2.2.2 Imaging of the silica matrix 26

2.2.3 Nitrogen adsorption and desorption 26

2.2.4 Positron annihilation spectroscopy 27

2.3 Results and discussion 28

2.4 Conclusion 40

Chapter 3

Ion Conduction behaviour in the Nanopores in Silica-gel Solid Nanocomposite Electrolytes 41

3.1 Introduction 41

3.2 Experimental 43

3.2.1 Synthesis of nano-SCE pellets 43

3.2.2 Removing ILE from nano-SCE pellets 44

3.2.3 Imaging of the SCE and silica matrix 45

3.2.4 Density measurement 45

3.2.5 Nitrogen Adsorption and Desorption 45

3.2.6 Positron Annihilation Spectroscopy 46

3.2.7 Conductivity measurement of nano-SCE 47

3.3 Results and discussion 48

3.4 Conclusion 69

Chapter 4

High-rate Performance Solid-State Lithium Batteries with Silica-gel Solid Nanocomposite Electrolytes using Bis(fluorosulfonyl)imide-based Ionic Liquid 71

4.1 Introduction 71

4.2 Experimental 72

4.2.1 Synthesis of nano-SCE pellets 73

4.2.2 Fabrication of the electrode foil 73

4.2.3 Fabrication of the battery cells 74

4.2.4 Conductivity measurement of nano-SCE 75

4.2.5 Pulsed field gradient nuclear magnetic resonance spectroscopy (PFG-NMR) 76
4.2.6 Three-electrode measurements of nano-SCE and ILE 76
4.2.7 Electrochemical stability of nano-SCE 77
4.2.8 Li stripping and plating test in a Li/nano-SCE/Li symmetric cell 77
4.2.9 Electrochemical measurement of the battery cells 78
4.3 Results and discussion 78
4.4 Conclusion 94

Chapter 5
General Conclusion and Future Prospects 96

References 99

List of Achievements 114
Peer-reviewed Journal publications 114
Conferences and Seminars 115
Patents 119

Acknowledgements 121

Chapter 1

General Introduction

1.1 Lithium-ion batteries (LIBs)

In 2019, the Nobel Prize in Chemistry was awarded to three eminent scientists, John B. Goodenough, M. Stanley Whittingham, and Akira Yoshino, for the development of lithium-ion batteries (LIBs). LIBs have been developed as revolutionary rechargeable

Fig. 1.1 Various types of lithium-ion batteries (Source: Panasonic website)

batteries that are suitable for long-term use and are lightweight in comparison with nickel-cadmium, nickel metal hydride, and lead-acid batteries. Since their discovery in 1990, LIBs have dominated the portable battery market in parallel with the increased popularity of mobile phones and laptops. They are also used as power sources for electric vehicles, which are rapidly emerging as a replacement to fuel-powered vehicles.[1–3] LIBs can also store a significant amount of energy from solar and wind power; thus, they may enable progression to a fossil fuel-free society. Currently, LIBs occupy greater than 90% of the battery market. Various types of LIBs, which are suitable for many applications, are shown in Fig. 1.1. LIBs are used ubiquitously to power the electronic devices that we use to communicate, work, study, move, listen to music, and search for knowledge. LIBs play a crucial role in our lives.

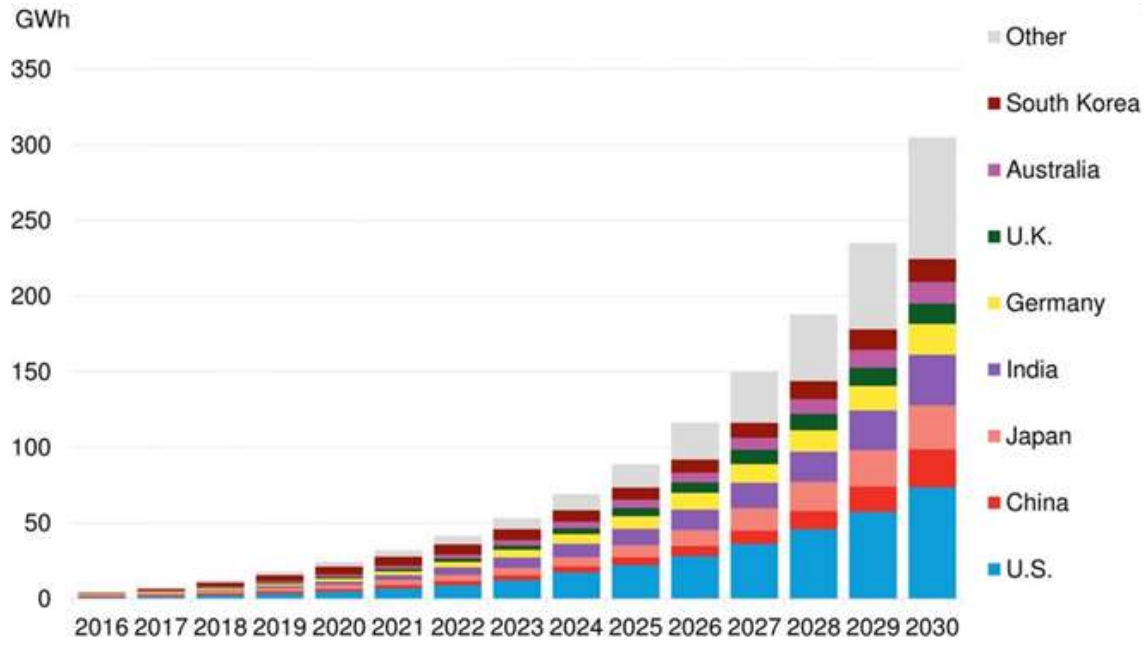

Fig. 1.2 Global cumulative energy storage deployments until 2030 (Source: Bloomberg New Energy Finance)

To realize a green and sustainable society wherein the environment, economy, and A forecast of global cumulative energy storage up to 2030 is shown in Fig. 1.2. The overall energy storage market is predicted to increase by approximately 10 times by 2030. convenience are in harmony, the requirements for energy storage devices are immense. LIBs are undoubtedly one of the most promising candidates to satisfy this demand because of their high energy density.[4–6] Therefore, LIBs are considered to be essential to humankind in the present day and will remain so in the future.

1.2 All-solid-state batteries (ASSBs)

The current LIBs, however, face a potentially fatal safety issue arising from their high energy density. LIBs include a highly reactive material, a volatile and flammable organic solvent, as their liquid electrolyte solution, which poses risks of fire and explosion in the event of internal shorting.[7] Indeed, some accidents involving LIBs have occurred. As such, there are strict rules governing not only their use but also before and after their

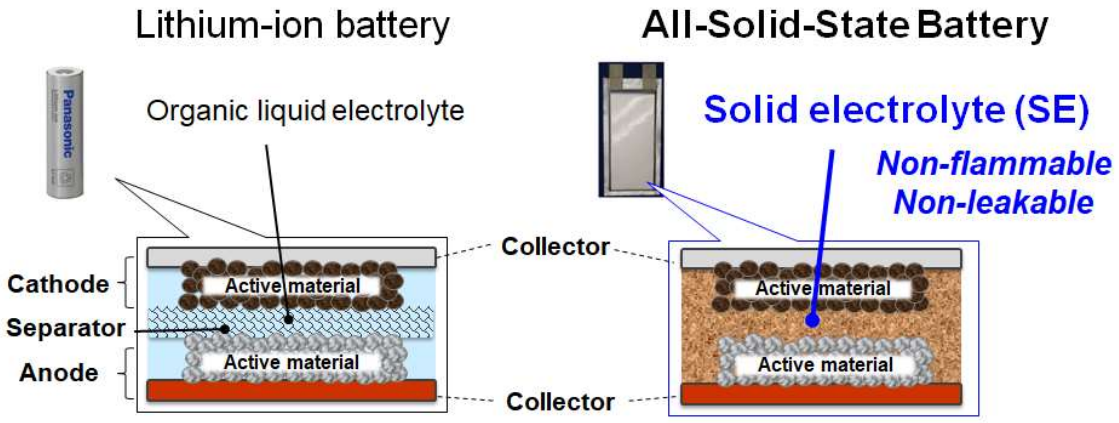

Fig. 1.3 Schematic diagrams of a lithium-ion battery and an all-solid-state battery

use, for example, during transportation, disposal, and recycling. At every step in their lifecycle, ensuring the safety of LIBs is inevitable to expand the applications of energy storage; this is of particular importance in electric vehicles to be used by people.

Consequently, to avoid accidents and ensure safety, all-solid-state batteries (ASSBs) with a solid electrolyte (SE) have been investigated.[8–10] LIBs and ASSBs are compared in Fig. 1.3. Solid materials can remove the risks of electrolyte leakage, volatilization, flammability, and explosions. In addition, SEs are deemed to suppress Li dendrite formation and may therefore enable the development of high-energy density batteries with Li-metal anodes.[11,12] Moreover, multiple all-solid-state cells can be stacked in a bipolar series within a single package. This increases the cell voltage and reduces the weight of the package, potentially yielding an energy density above 1000 Wh L^{-1}.[13,14] ASSBs may be the next breakthrough battery type after conventional LIBs, which were proposed by the Nobel Prize winners and developed by subsequent researchers.

1.3 Solid electrolytes (SEs)

One of the differences between LIBs and ASSBs is the electrolyte material. The key material in the development is the SE for ASSBs. A tremendous amount of research has been directed toward creating SEs with improved performance compared with conventional liquid electrolytes. However, the SEs developed thus far face several issues. A brief summary of the history of the SEs is presented in Fig. 1.4. The SEs developed so far can be classified into three types, i.e., ceramic-based, sulfide-based, and polymer-based. Ceramic-based SEs typically suffer from a low ionic conductivity of 10^{-4} S cm^{-1} and poor interfacial contact with the electrodes. Although high pressures are applied to

decrease the resistance at the interface as an additional process in battery fabrication, the interfacial contact degrades during charging and discharging cycles.[15,16] To date, sulfide-based electrolytes with high conductivities of up to 10^{-2} S cm^{-1} have been developed, but in addition to the required improvements in the interfacial contacts, the potential formation of toxic H_2S gas needs to be resolved for these electrolytes.[17–19] The electrical contact is not a major issue with polymer-based SEs owing to their soft and adhesive nature; however, their ionic conductivity is typically below 10^{-4} S cm^{-1}. Moreover, polymer electrolytes have relatively low thermal stability and mechanical

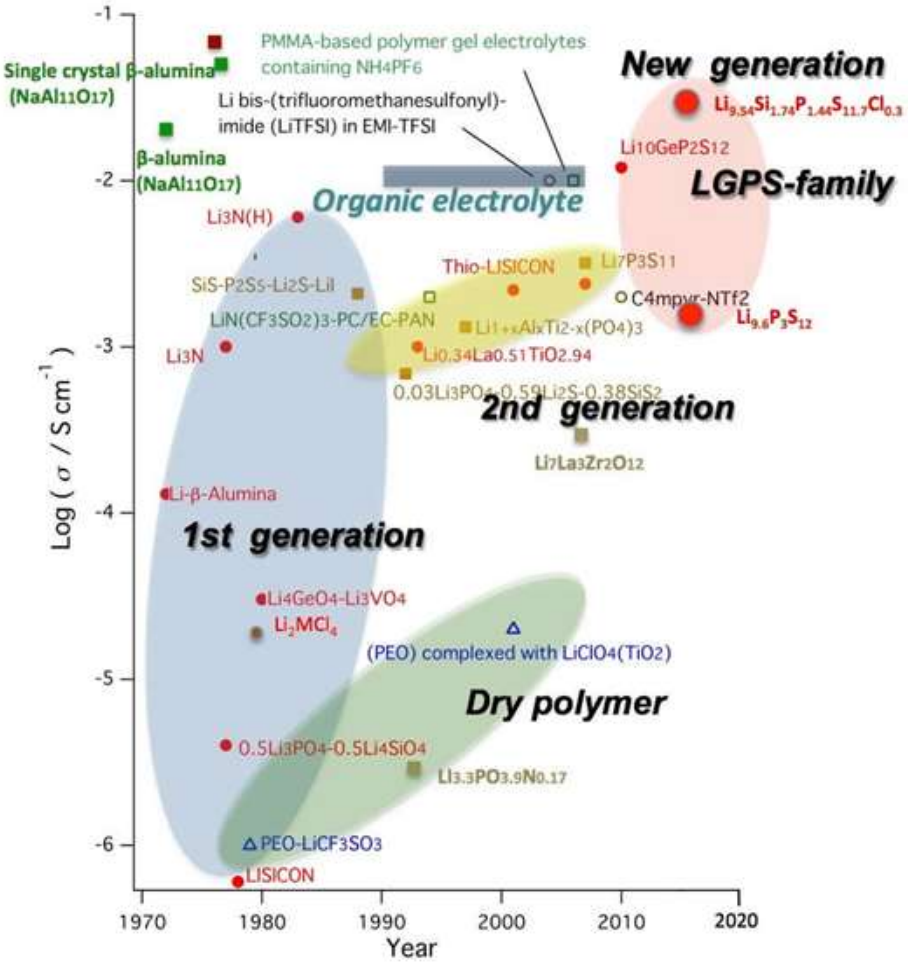

Fig. 1.4 History of lithium superionic conductors (Source: Tokyo Institute of Technology)

strength, which prevents the growth of lithium dendrites.[20,21] High-performance SEs with fast lithium-ion conduction, good interfacial contact with the electrodes, high thermal stability, wide electrochemical window, and sufficient mechanical strength, made using non-toxic and environmentally friendly materials, have not yet been developed.

1.4 Ionogels

To fulfill these requirements, composites of a mesoporous oxide matrix filled with ionic liquid electrolyte (ILE) fillers have been proposed as SEs. These are referred to as inorganic-based "ionogels," which comprise a non-volatile ionic liquid (IL) as the solvent, Li salt as the electrolyte, and inorganic oxide matrix.[22,23] The highest ion conductivity was obtained for an ionogel when the nanoporous oxide matrix was prepared by a chemical method, namely the one-pot sol-gel method.[24] An illustration of a silica-based ionogel is shown in Fig. 1.5.[25] The preparation of oxide-based chemical ionogels starts with a homogeneous liquid mixture, wherein an ILE composed of an IL and Li salt is added to a sol-gel precursor solution to synthesize the oxide matrix. In this method, the ILE and matrix form a composite in an "in situ" manner, wherein the precursors in the solution react to form an oxide matrix around the ionic liquid template, encapsulating it in the process. Under certain synthesis conditions, the solid composite electrolyte (i.e., a solid Li-ion conductor) can be in the form of a monolith with the ILE embedded in a continuous mesoporous oxide network. Such electrolytes ensure battery safety because of the non-volatility and thermal and electrochemical stability of the ILs and inorganic ingredients.[25] Furthermore, the extremely high porosity of the inorganic matrix confers a gel-like consistency to these nanocomposite electrolyte materials, making them

mechanically compliant with polymer electrolytes. The large porosity yet rigid porous matrix provides reasonable Li-ion conductivity combined with good mechanical properties. More importantly, a low-viscosity liquid sol-gel precursor can be impregnated into the dense porous powder electrodes, similar to a liquid electrolyte, where it further gels in the electrodes, which has the potential to achieve good all-around interfacial

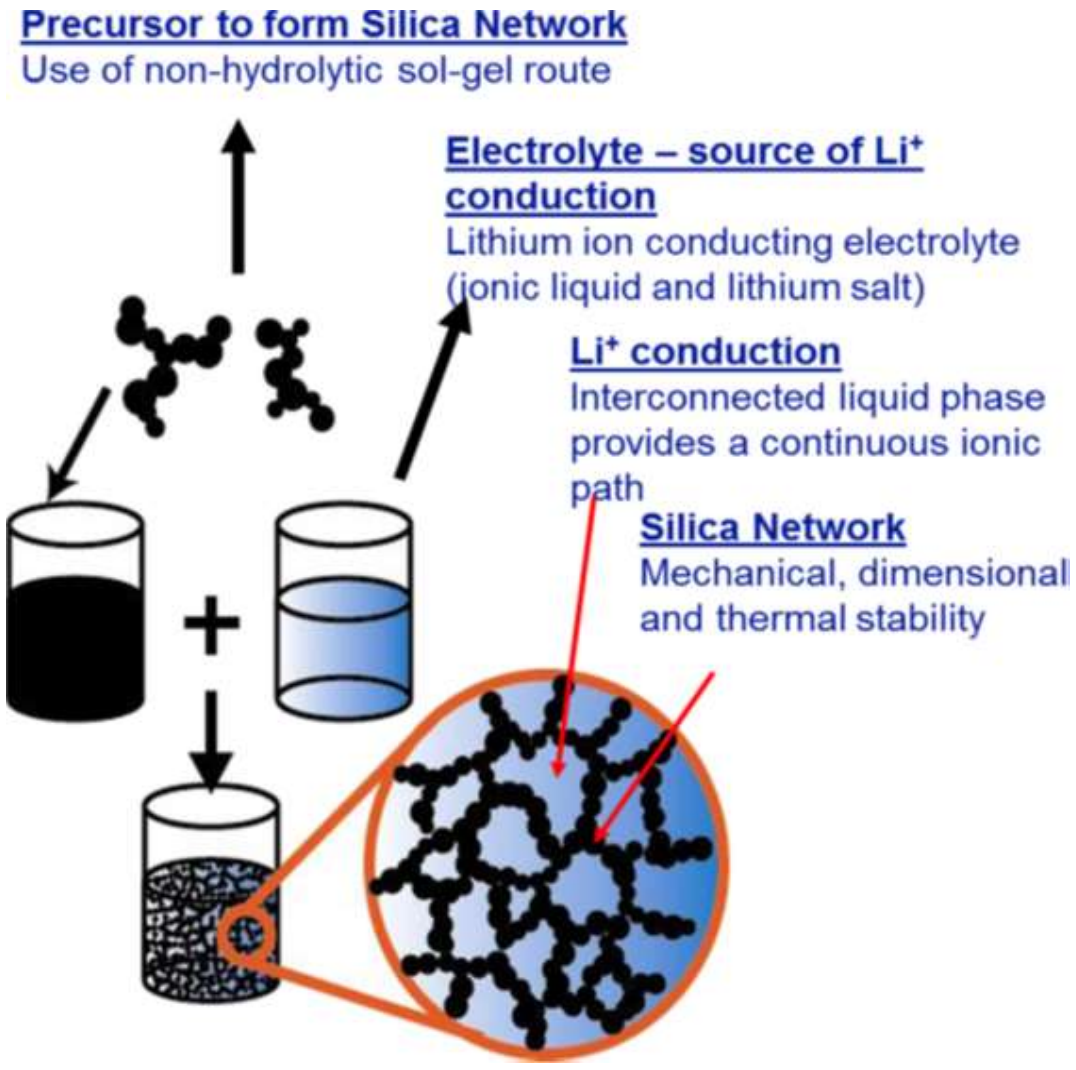

Fig. 1.5 Inorganic-based ionogel.[25] Reproduced with permission of ref. [25] Copyright 2017, Elsevier Inc.

contact between the active electrode particles and the electrolyte. As such, after further drying and curing of the ionogel, dense nanocomposite electrodes with high energy and power densities can be realized.

However, the acidic nature of most of the reported sol-gel precursor chemistries has limited their compatibility with electrode materials to only $LiFePO_4$ (LFP), which typically has a protective carbon coating. Since the first demonstration of Li/Ionogel/LFP in 2011,[26,27] different ILEs, oxide materials, and electrode materials have been investigated.[24,28,29] Although stable battery performance has been achieved, the C-rate performance of these solid batteries is not satisfactory because of the low ionic conductivity of ionogels (<1 mS cm^{-1}) or the chemical incompatibility of the precursor with the electrodes. In the former case, the ionic conduction of the ionogel is typically lower than that of the confined ILE owing to the increase in the viscosity of the mesopores.[30] In the latter case, dry electrodes are typically pressed against a thick ionogel pellet. Hence, a highly conductive ionogel from a chemically mild precursor is required to achieve ionogel-based solid-state batteries with excellent C-rate performance.

1.5 Solid nanocomposite electrolytes (nano-SCEs)

From this background, Chen et al. developed a new concept that consisted of a composite electrolyte formed from a water-based sol-gel process; which is called a “solid nanocomposite electrolyte” (nano-SCE).[31] A photograph of transparent silica gel nano-SCE pellets is shown in Fig. 1.6. These silica gels are sometimes considered as hybrid SEs because they contain a liquid. However, for the silica nanocomposites, as described in this paper, the ionic “liquid” electrolyte acts like a solid when confined in the tens of nanometer-sized channels owing to an increase in viscosity and adsorption onto the silica

wall constraining the channel. If the silica matrix acted merely as a porous separator, then the increase in viscosity for the confined liquid electrolyte would lead to a decrease in ionic conductivity, similar to that seen in ionogels.

Instead, the interaction between the ILE molecules and the silica pore render the properties of the nanocomposite different from the sum of its individual components. The adsorption of ILs on oxides resulting in the formation of solid mesophase layers up to a few nanometers in thickness has been shown on planar surfaces using atomic force microscopy (AFM), [32] X-ray reflectivity (XRR),[33] and molecular dynamics (MD) simulations.[34] XRR analysis revealed the IL molecule ordering in Fig. 1.7. The formation of an interfacial water phase between the hydrophobic IL solvation layer and

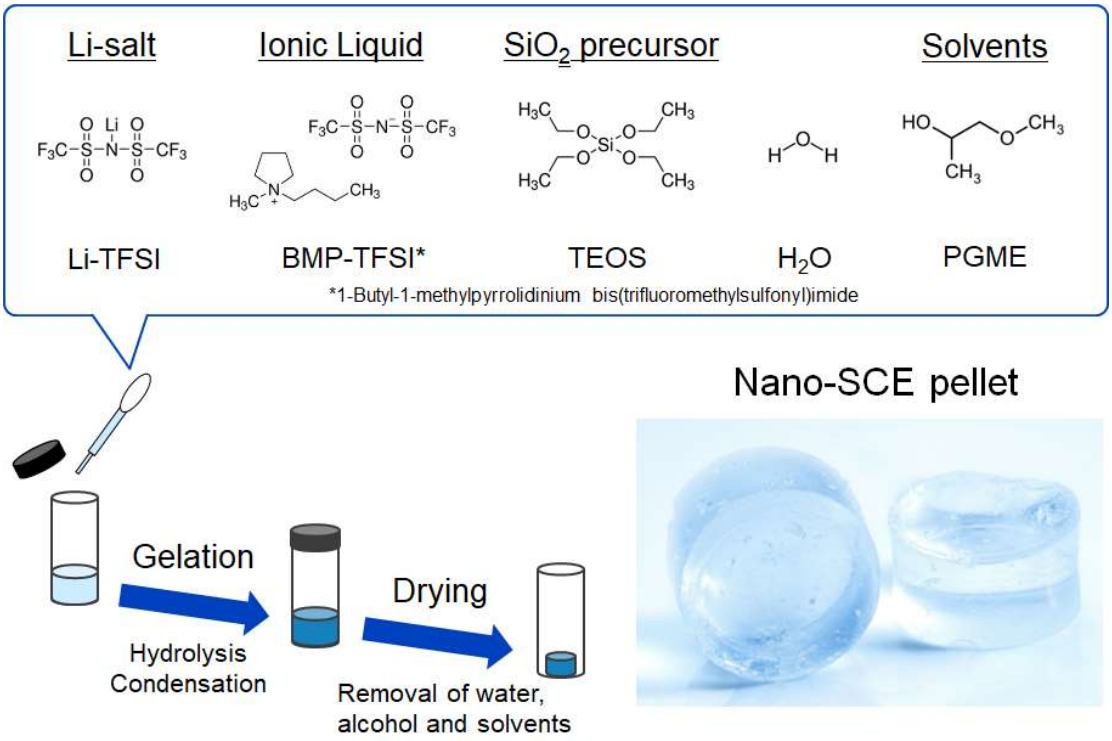

Fig. 1.6 Fabrication method of nano-SCE pellets.[31] Reproduced with permission of ref.[31] Copyright 2020, American Association for the Advancement of Science.

silica surface was observed using AFM.[35] The significantly strong adhesion forces observed in the force curve measurement indicated that the strong hydrogen bonding on the silica surface adsorbed water molecules onto the silica surface, and that the IL molecules were stacked in an orderly manner on the water layer. A firm adsorbed mesophase layer with an IL/water/silica stack was formed with the combination of appropriate IL, water, and oxide materials. Hence, this selective adsorption of IL anions and cations on the oxide surface leads to enhanced Li^+ conductivity at the interfaces, demonstrating the novel concept of surface conduction promotion in nano-SCEs.

Based on this new concept, Chen et al. demonstrated the systematic promotion of Li-ion conductivity in a sol-gel derived nano-SCE by introducing an interfacial ice-water layer. This interfacial layer comprised a solid-adsorbed water layer, which was a few monolayers thick, between the IL molecules and the OH-terminated silica surface, as

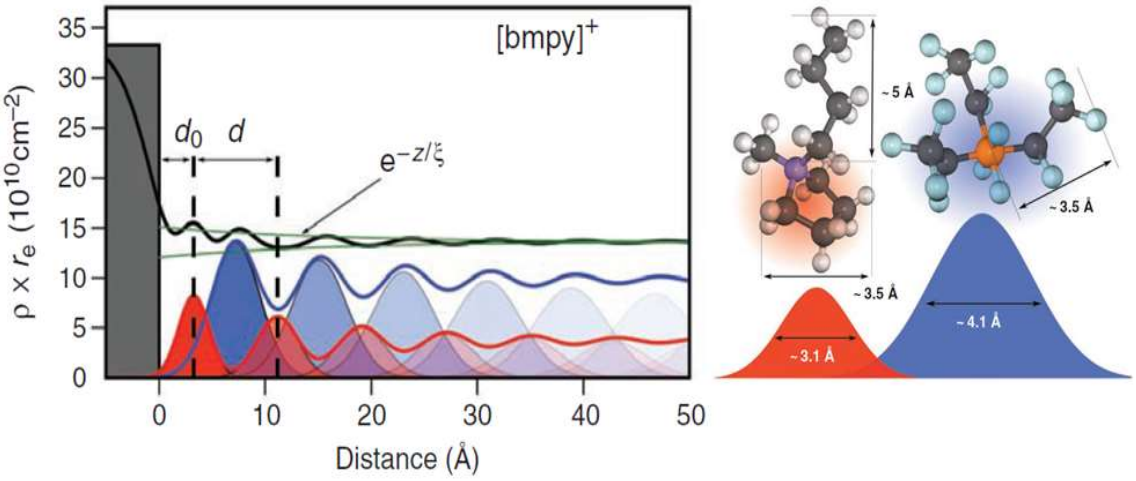

Fig. 1.7 Reported X-ray reflectivity characterization of the 1-butyl-1-methylpyrrolidinium tris(pentafluoroethyl)-trifluorophosphate ionic liquid on sapphire surface.[33] Reproduced with permission of ref.[33] Copyright 2016, American Association for the Advancement of Science.

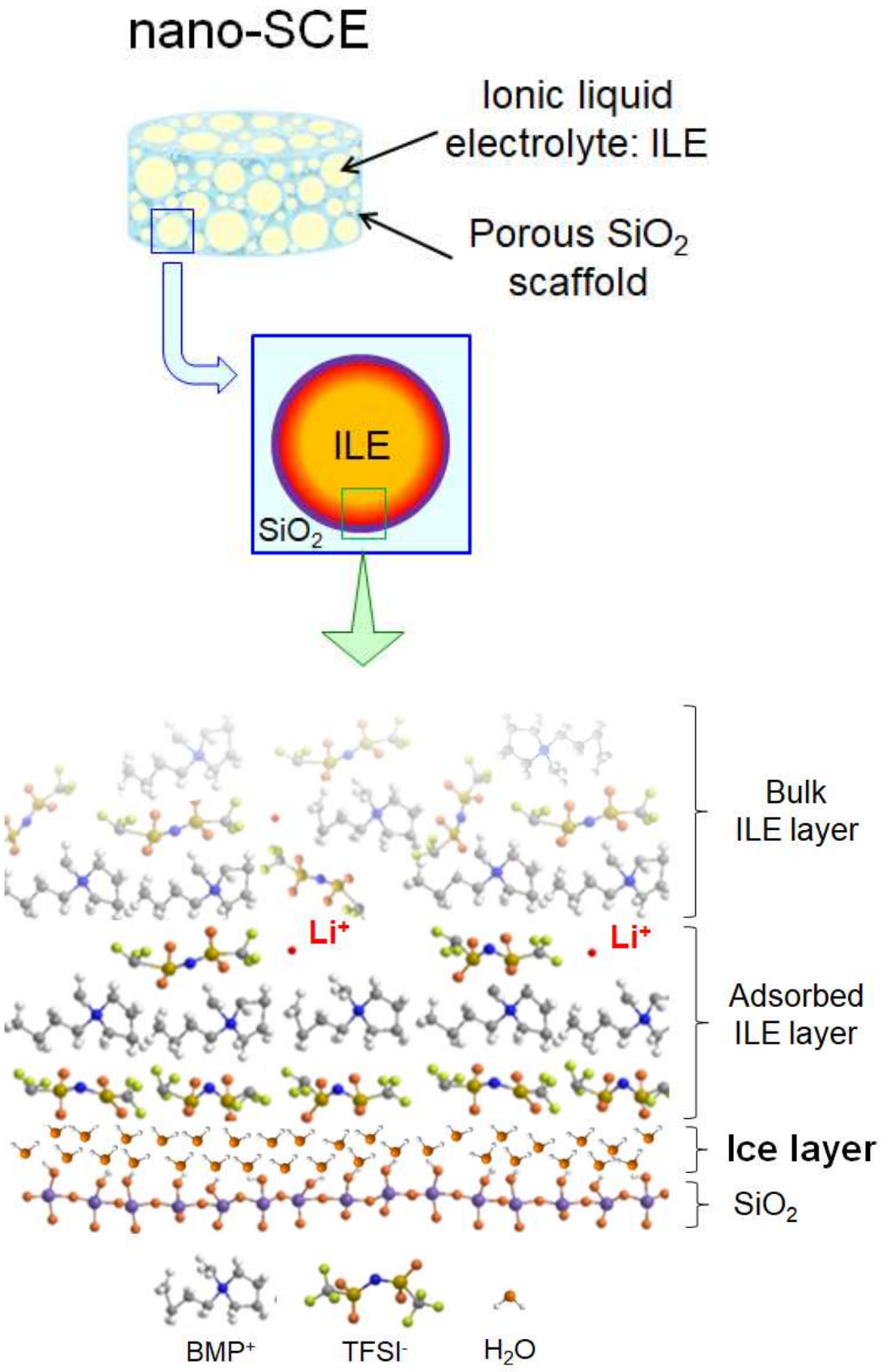

Fig. 1.8 The adsorbed interfacial ILE layer and ice-water layer on the SiO_2 pore wall.

shown in Fig. 1.8.[31,36,37] The ionic conductivity of the nano-SCE and the mechanism of surface conduction promotion are shown in Fig. 1.9. It was found that strong hydrogen bonding between the ice-water and the IL molecules induced molecular ordering of the ionic liquid anions and cations on the silica surface. This interfacial interaction weakened the association between the Li-ion and its anion, thus enhancing the ion conductivity well beyond (i.e., 200% at maximum) that of pure ILEs.[31] Here, the activation energy for diffusion was confirmed to be lower along the composite interface with the adsorbed ILE layer and ice-water layer, indicating that the free Li^+ concentration increased near the surface.

As such, high conductivity with surface conduction promotion is an exceptional feature of nano-SCEs that does not occur in ionogels. In addition, as the ice-water layer was confirmed to be electrochemically inactive, it did not degrade during the cycling of the batteries. Furthermore, damage to the active electrode materials was avoided as the water-based sol-gel precursors do not contain corrosive acidic compounds, such as formic acid (FA), which are typical catalysts proposed in the literature. Nano-SCEs have the potential to solve the issues of not only ionogels but also of conventional SEs, and therefore, they can meet all the requirements for SEs mentioned previously (Section 1.3).

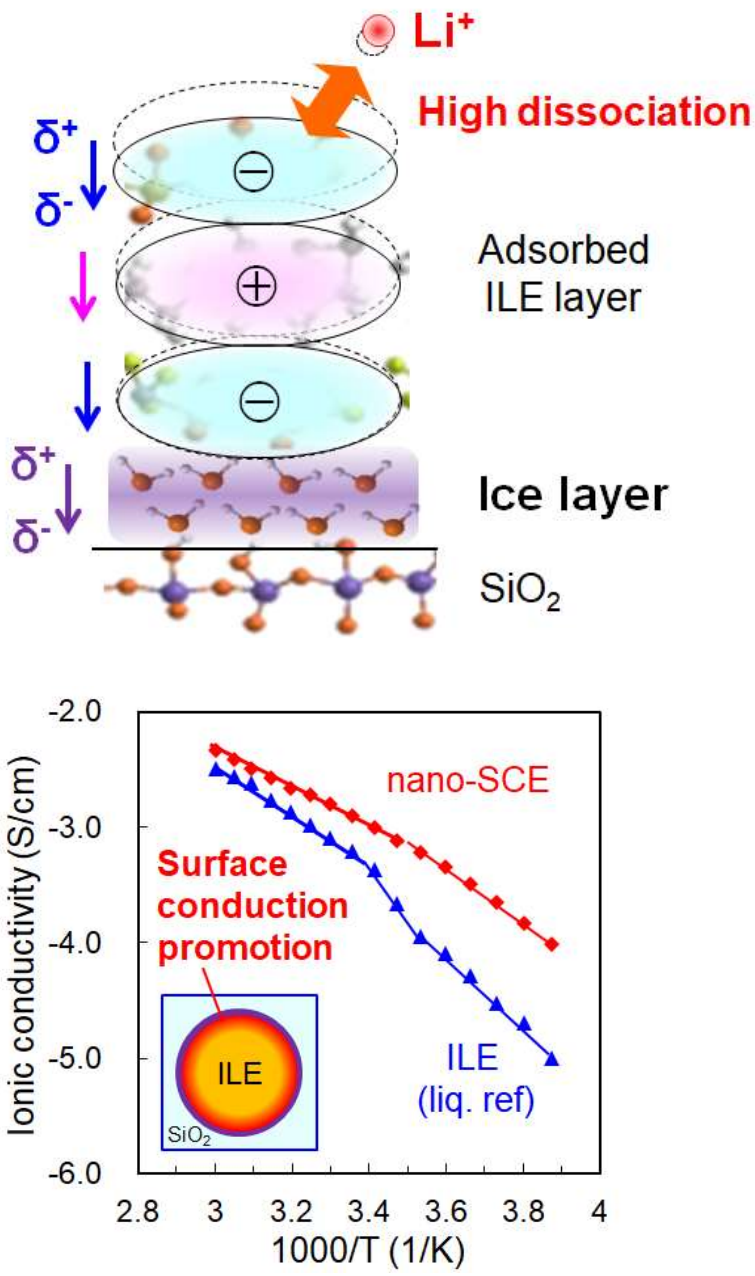

Fig. 1.9 Ionic conductivity of a nano-SCE and the mechanism of surface conduction promotion.

1.6 Aims and outline of the thesis

For these reasons, newly developed nano-SCEs may be a breakthrough material to allow production of ASSBs and to meet future energy storage requirements. To improve the conductivity and realize high-power performance using nano-SCEs, the surface enhancement effect will have to be maximized by tailoring the surface chemistry and nanostructure of the matrix. To achieve this, a comprehensive and quantitative understanding of the Li-ion conduction behavior in the pores and the design of an ideal porous structure is necessary. In other words, the effect of the silica nanostructure (pore size, surface area, and porosity) on the surface conduction promotion and confinement effects must be understood.

This research aims to clarify the ion conduction behavior in nanopores of nano-SCEs and to demonstrate the high-power performance of the cell based on the new findings. An overview of the research is shown in Fig. 1.10.

First, the characterization procedure of the nanostructures of IL-templated porous silica was established, as described in Section 2. Positron annihilation lifetime spectroscopy (PALS) was first selected to distinguish the nanometer-sized and closed pores from the mesopores and macropores. A comprehensive understanding of the pore structure of the porous silica matrix of nano-SCEs combined with SEM, TEM, and N_2 adsorption/desorption measurements is discussed.

As described in the beginning of Chapter 3, the pore structures of the silica matrix in nano-SCEs, such as pore size, surface area, and porosity, were analyzed by the characterization method established in Section 2. Subsequently, the relationship between

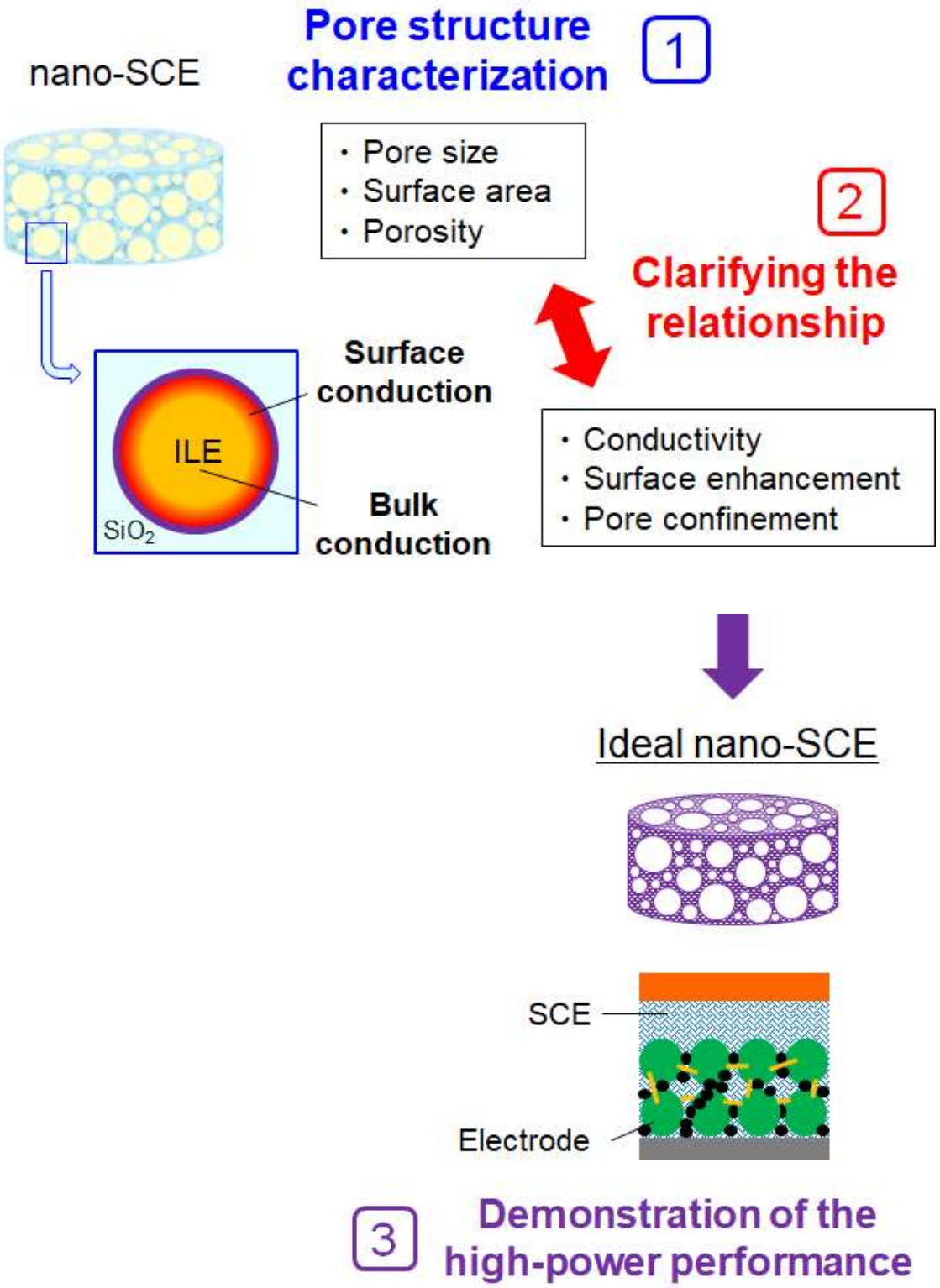

Fig. 1.10 Overview of this research: Mechanistic analysis and ion conduction behavior in nano-SCEs and demonstration of high-power performance.

the pore structure and ion conduction behavior was clarified and described. The degree of the surface conduction promotion effect and pore confinement effect was verified in relation to the ILE and ice-water layer thickness estimated from the analysis of pore size, surface area, and porosity.

Based on the findings in Chapter 3, a bis(fluorosulfonyl)imide (FSI)-based IL was selected to reduce the pore confinement effect in a new nano-SCE. A Li-$LiFePO_4$ cell was fabricated using the new nano-SCE with EMI-FSI, and its electrochemical performance was compared with that of a cell using a conventional liquid electrolyte. The rate performance of each cell is described and discussed in Section 4.

Finally, the overall conclusions of this dissertation and further suggestions for achieving higher conductivity and expanding the new applications using nano-SCEs are summarized and described in Chapter 5.

Chapter 2

Pore structure analysis of ionic liquid-templated porous silica using positron annihilation lifetime spectroscopy

2.1 Introduction

Porous materials have attracted considerable attention over the years owing to their potential for use in a wide range of applications, including catalysis, chemical separation, sensors, nanoelectronics, and drug delivery [38–41]. To fabricate porous structures, sol-gel processes have been developed and extensively used [5, 6]. In a typical sol-gel process, hydrolysis and condensation of a metal oxide precursor are performed to form a sol in an alcoholic aqueous solution. This is followed by gelation and drying of the sol to remove the existing water, alcohol, and solvents. Herein, by introducing a templating agent in the initial solution, such as a surfactant, nanostructures in the resultant gel can be tailored. These soft-templated sol-gel processes enable the realization of a variety of nano-ordered structures in accordance with the demands of the applications listed above [44–47].

Room-temperature ionic liquids (RT-ILs) are organic salts with melting points below 100 °C. They are one of the favorable templates in the sol-gel process owing to their unique properties, such as high-thermal stability, nonflammability, and environmental friendliness [11, 12]. Given that ILs have an undetectable vapor pressure in a broad temperature range of −96 to +400 °C, they do not evaporate during long aging periods, thus enabling the production of a stable gel network. Moreover, tunable physical

characteristics (i.e., size and shape of molecules) and chemical characteristics (i.e., hydrophilicity and end-group of molecules) allow the control of the pore size, structure, and distribution in the gel. Since the first report on monolithic porous silica by Dai *et al*. [50], which was fabricated by a sol-gel process using 1-ethyl-3-methylimidazolium bis(trifluoromethylsulfonyl) imide (EMI-TFSI), many studies have been conducted for the creation of various types of structures, such as wormlike [51], lamellar [15, 16], and random structures with very high porosity [54–56]. Various types of ILs have been tested to fine-tune the nanostructure [57–59]. Subsequently, the research has been extended to the use of different oxide materials, such as titanium oxide (TiO_2) [60] and alumina (Al_2O_3) [61].

Based on the definition of the International Union of Pure and Applied Chemistry (IUPAC), porous structures can be classified into three categories according to their pore diameter: micropores (<2 nm), mesopores (2–50 nm), and macropores (>50 nm) [41,62]. These three types of pores created in IL-templated porous silica have been characterized by various techniques. Scanning electron microscopy (SEM) and transmission electron microscopy (TEM) have been the most popular methods for the observation of the pores in these materials. However, although they have been successfully used to visualize the fine structures of IL-templated porous silica [51–54,59–61], it has been difficult to quantitatively evaluate the pore size because of the overlap of the randomly located pores within the samples. By contrast, nitrogen adsorption/desorption measurements have been conducted for the quantitative analysis of the surface area and pore size distribution of IL-templated porous silica [50–54,57–61]. This method is known as the standard method for the characterization of porous materials; however, it can only evaluate open spaces, because the N_2 gas cannot access closed spaces such as vacancy and voids. Additionally, it is generally difficult to analyze structures with sizes of a few nanometers (micropores)

with this technique. Small-angle X-ray scattering (SAXS) and small-angle neutron scattering (SANS) techniques have been used to obtain the pore structure information of IL-templated porous silica, including that of the closed pores [50–54,59]; however, the detection size is typically limited to ~2 nm, owing to the diffraction limit of X-rays. Therefore, pores with sizes on the order of a few nanometers (micropores) in IL-templated porous silica, including closed pores, have not been fully characterized. Micropores are important because they can act as bridges between the microporous zeolite and mesoporous materials, and they can thus potentially show size and shape selectivity for organic molecules [39,63]. Additionally, it is important to know the free volume of the open spaces to control the mechanical properties, such as the elastic modulus and fatigue resistance [41,43]. Nevertheless, to date, scientific interest in understanding the micropore structures in IL-templated porous silica has been limited.

In this section, it is reported the use of positron annihilation lifetime spectroscopy (PALS) to analyze nanometer-sized and closed pores in IL-templated porous silica. The unique interaction of the antimatter probe (i.e., the positron with the electron) provides information on the open space with sizes spanning the sizes of atomic vacancies to a few tens of nanometers for the cases of open and closed pores with high sensitivities [25, 26]. PALS has contributed significantly to the evaluation of vacancy-type defects and open volumes in semiconductor materials [27, 28], and it has been successfully extended to the characterization of porous materials [68]. It has potential to be used for comprehensive understanding of the pore structures of IL-templated porous silica. I prepared IL-templated porous silica with different compositions, ratios of IL and silica precursor, and characterized it by PALS. Based on the combination of results obtained with SEM, TEM, and N_2 adsorption/desorption measurements, the relationship between the IL and silica precursor ratio used in the synthesis and the porous structure is analyzed and discussed.

2.2 Experimental

2.2.1 Sample preparation

The samples were prepared with a single-step sol-gel method using IL. The porous silica matrix was formed with a slow hydrolysis-condensation reaction of the SiO_2 precursor with the use of the IL as a soft template for the condensation of the interconnected hydrated silica network. Tetraethyl orthosilicate (TEOS, 98%, Sigma–Aldrich) was selected as a SiO_2 precursor, and 1-butyl-1-methylpyrrolidinium bis(trifluoromethylsulfonyl)imide (BMP-TFSI, 98.5%, Sigma–Aldrich) was selected for ionic liquids, respectively. Lithium bis(trifluoromethylsulfonyl)imide (Li-TFSI, 99%, Solvey) was used as the catalyst to trigger the hydrolysis reaction. It has the same anionic molecular structure as that of BMP-TFSI, and was added in the initial solution together with deionized water (DIW) and 1-methoxy-2-propanol (PGME, 99.5%, Merck). The molar ratio between BMP-TFSI and TEOS (hereinafter "x") in the mixture was varied between 0.5 and 2.0. Accordingly, the amounts of Li-TFSI and BMP-TFSI were determined with the use of these ratios. For example, when x = 1, the added BMP-TFSI and Li-TFSI in the solution were 0.97 g and 0.22 g, respectively. The volume of TEOS, DIW, and PGME, were fixed at 0.5 mL, 0.5 mL, and 1 mL, respectively. The pH value in the mixture with large excess of water and PGME was approximately equal to five. This mild pH condition ensured that the hydrolysis and condensation reactions are favorable [69]. The mixtures were shaken for 1 min to form monophasic solutions. These solutions were then stored without stirring to form gels at 25 °C and at 50% relative humidity (RH) in a climate chamber (SH-641, Espec Corporation). After the gelation process was completed (within a period that spanned a few days), the samples were soaked in acetone

for 36 h (12 h × 3) to extract the IL and Li salt, and was then dried in vacuum for 12 h at 25 °C (<5 Pa) to remove the solvent.

2.2.2 Imaging of the silica matrix

The morphologies of the samples were investigated with SEM and TEM. SEM was conducted using a Thermo–Fisher Apreo tool with an acceleration energy setting in the range of 1.5–2.0 kV; it was operated in a dual-detector imaging mode with T1 and T2 detectors in a parallel configuration for live image adjustments. Additionally, the T2 detector was used to record the acquired SEM images. For the measurements, a piece of the sample was fixed with carbon conductive tape. TEM was conducted with the use of JEM-ARM200F at 300 keV. To minimize the overlap of silica with the voids, the samples were ground as follows. A piece of the sample was placed in the solution and vibrated for 7 min in an ultrasonic bath. Subsequently, three droplets of silica dispersed solution were picked up and deposited onto the copper lacey carbon grid.

2.2.3 Nitrogen adsorption and desorption

The obtained samples were de-gassed for 4 h at 40 °C using 0.1 mbar vacuum. Subsequently, nitrogen physisorption isotherms were acquired at T = −196 °C with an Autosorb 3 analyzer. The surface area was extracted from the adsorption isotherm based on the Brunauer–Emmett–Teller (BET) theory. The BET theory is based on a model that describes the amount of gas adsorbed on a silica surface at different pressures [62,70,71]. The pore size distribution was analyzed with the Barrett–Joyner–Halenda (BJH) method, assuming a cylindrical pore [72].

2.2.4 Positron annihilation spectroscopy

PALS was carried out using a conventional lifetime system, as described elsewhere [36]. The positron source was prepared by depositing and drying aqueous ^{22}NaCl (radioactivity of ~500 kBq) on Kapton polyimide foil, and by covering it with another Kapton foil. Subsequently, the positron source was sandwiched between two identical samples, which were prepared by packing the samples in the central groove of acrylic holders (4.5 mm in diameter, 3 mm in thickness), and then placing them in a vacuum chamber (10^{-3} Pa). The positron beam was irradiated through the whole sample (in 3 mm thick). To prevent backscattering of γ-rays by the scintillators, the two detectors were positioned perpendicular to each other. All the measurements were conducted at room temperature. The full width at half maximum (FWHM) of the time resolution of the system was ~230 ps and the time calibration constant was 102.7 ps/ch. The total number of accumulated counts was in the range of 4×10^6 to 8×10^6 for each lifetime spectrum. Here, the lifetime spectrum can be represented in a continuous decay form according to,

$$S_{LT}(t) = \int_0^\infty \lambda\alpha(\lambda)\exp(-\lambda t)d\lambda \tag{2.1}$$

where $\alpha(\lambda)$ is the probability density function (PDF) of the annihilation rate. The free volume hole distribution can be determined by the deconvolution of the lifetime using the numerical Laplace inversion technique [38, 39]. The computer program CONTIN was used for these calculations [40, 41]. The pore sizes of the samples were estimated from the lifetime using the extended Tao–Eldrup (ETE) model, which is a quantum mechanical model established by Gidley *et al*. [42, 43]. The EELViS calculator was used for this estimation [81].

2.3 Results and discussion

Figure 1 (a) shows the SEM image of the IL-templated porous silica with an IL/SiO_2 ratio of 1.5 (x = 1.5). The scaffold of porous silica, which is wrapped around various sizes of open spaces, is shown in Fig. 2.1 (a). The diameters of large open spaces are in the range of 200–400 nm (as indicated by the white closed circles), whereas the diameters of

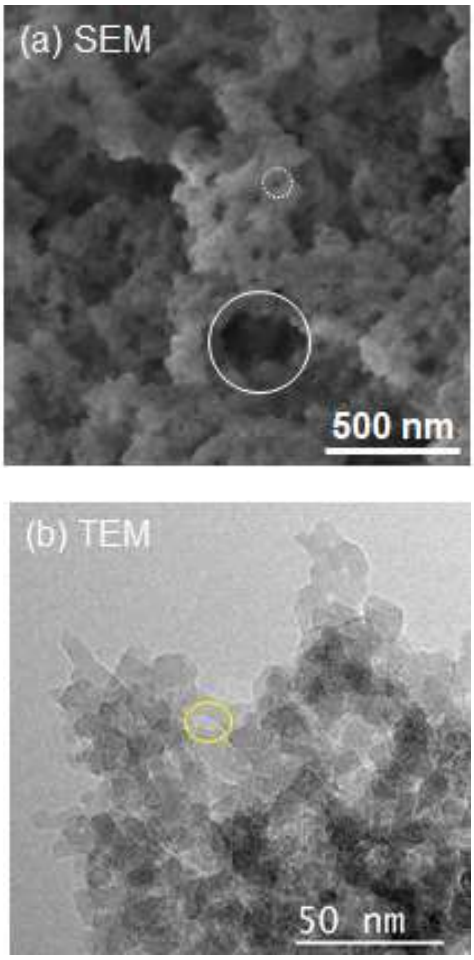

Fig. 2.1 (a) Scanning electron microscopy (SEM) and (b) transmission electron microscopy (TEM) images of ionic liquid (IL)-templated mesoporous silica with an IL/SiO_2 of 1.5. Reproduced with permission of ref.[82] Copyright 2020, Elsevier Inc.

the smaller pores are typically in the range of 30–70 nm. The smallest pore diameter in this figure is approximately 10 nm (indicated by the white dotted circles). Given that it is difficult to obtain clear images with high magnification owing to the charge-up of the insulating samples, the small-sized pores cannot be fully characterized by SEM only. To distinguish the pore sizes of the order of a few nanometers, high-resolution TEM analyses were carried out. The TEM image of the IL-templated porous SiO_2 with x = 1.5 is shown in Fig. 2.1 (b). A microstructure composed of closely packed silica nanoparticles is observed. The average particle diameter is approximately 14 nm for this sample. In addition, an open space is observed between the silica particles in the thinnest area of the sample (indicated by the yellow circle). The diameters of these pores are in the range of 5–10 nm. These values correspond to the smallest sizes of pores that can be observed by SEM, as indicated in Fig. 2.1 (a). As the silica particles and pores overlap, it is difficult to conduct further quantitative analyses of the microstructure by TEM. A complementary analysis should therefore be performed to determine the sizes of the micropores.

N_2 adsorption/desorption measurements were conducted to characterize the pore size and its distribution quantitatively. Figure 2.2 (a) shows the isotherms of the IL-templated porous silica at different IL/SiO_2 ratios (x = 0.5, 1.0, 1.5, 1.75 and 2.0). All the data show hysteresis with a N_2 adsorption branch (bottom line) and N_2 desorption branch (top line). This behavior can be classified as a typical type IV category, as defined by IUPAC, thus indicating that a mesoporous structure (2–50 nm) exists and is dominant in the sample [31, 33]. When the IL/SiO_2 ratio is increased from 0.5 to 2.0, the hysteresis of the isotherm plot becomes clear. This indicates that the pore size distribution is larger in the sample with a higher IL/SiO_2 ratio. By contrast, the total pore volume increased as a function of the IL/SiO_2 ratio. This can be explained by the expansion of the open space according to the volume fraction of IL, i.e., the space occupied by IL increased as a function of the

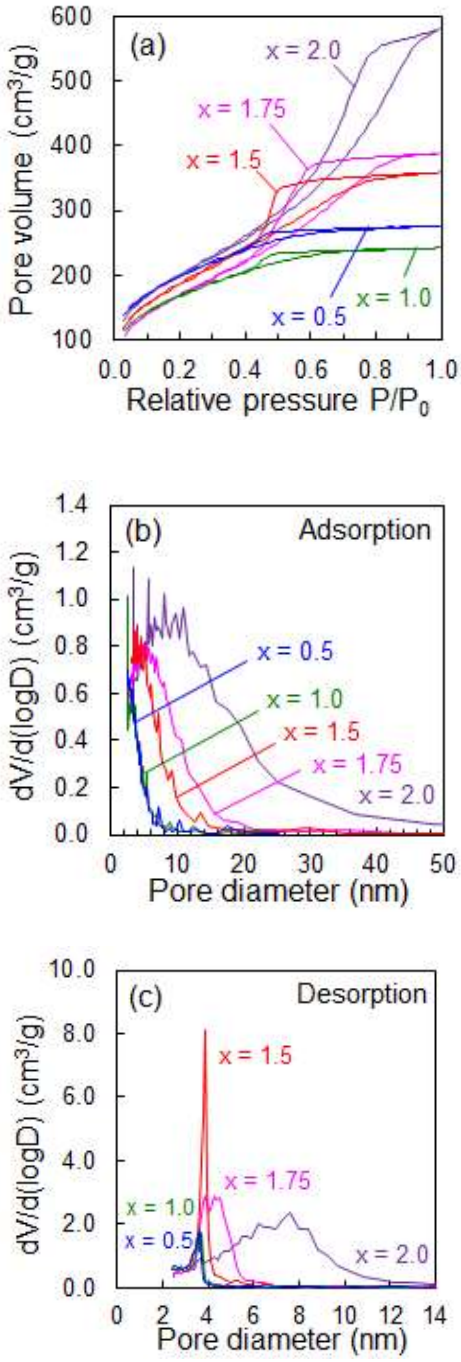

Fig. 2.2 N_2 adsorption/desorption measurements of IL-templated mesoporous silica. (a) Isotherm and (b) log differential pore size distribution analyzed using the adsorption part of the isotherm and the BJH method. (c) Log differential pore size distributions analyzed based on the desorption part. "x" denotes the IL/SiO_2 molar ratio of the samples. Reproduced with permission of ref.[82] Copyright 2020, Elsevier Inc.

IL/SiO_2 ratio. Figures 2.2 (b) and (c) show the log differential pore size distributions, which were analyzed by the BJH method assuming a cylindrical pore [72]. The numbers of pores are shown on the vertical axes of these graphs. Therefore, these plots provide information about the pore sizes and their distributions. In general, the pore size distribution obtained from adsorption branches reflect the length of the larger part in the cylindrical pore, and the distribution of the desorption branch reflects the smaller part.

All the plots contain one main peak in the 2–50 nm region (Figs. 2.2 (b) and (c)), i.e., one type of mesopore can be distinguished using these measurement conditions. The profiles of the IL-templated porous silica with x = 0.5 and 1.0 are almost identical, although the templated IL volume of the sample with x = 0.5 was twice as large as the volume of the sample with x = 1.0. This implies that the pore structure in the samples with x = 1.0 collapsed and shrunk after acetone rinsing and vacuum drying owing to the surface tension of porous silica. This might be the case for the samples with higher IL/SiO_2 ratios (x > 1.0) because the mechanical strength of porous silica scaffold was weaker owing to the decreased SiO_2 volumetric ratio. The pore sizes and their distributions with x = 0.5 and 1.0 are smaller than those of the others, thus indicating that homogeneous pores exist in these samples. The main pore sizes of these samples are in the range of 3.5–3.6 nm (Figs. 2.2 (b) and (c)). In the sample with x = 1.5, the pore sizes are slightly increased and are in the range of 3.8–3.9 nm. Additionally, the number of pores increased (by more than four times) compared to the sample with x = 0.5 and 1.0. In addition, the pore size distribution is slightly broader. The created structure had clearly changed at this composition. For the sample with x = 1.75 and 2.0, both the pore size and its distribution increased considerably, although there were minor differences of IL volumes in these samples compared to those with x = 1.5. The pore sizes are in the range of 4.2–5.0 nm for the sample with an x = 1.75, and 7.6–8.7 nm for the sample with x =

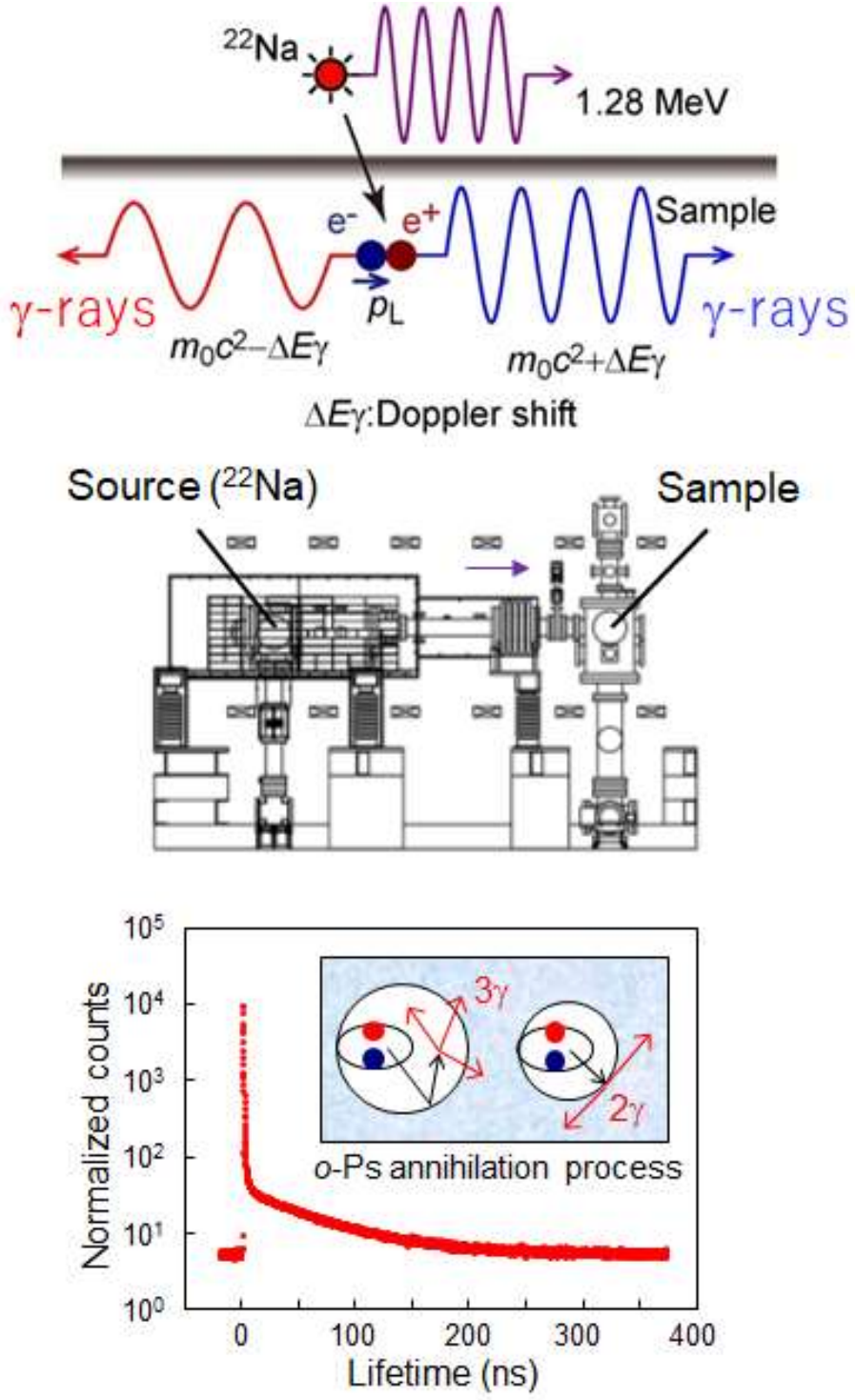

Fig. 2.3 Positron annihilation lifetime spectra of IL-templated porous silica with an IL/SiO_2 ratio of 1.5. Two types of otrho-positronium (*o*-Ps) annihilation processes are shown in the figure. Reproduced with permission of ref.[82] Copyright 2020, Elsevier Inc.

2.0. This increase of pore diameter can be explained by the expansion of the open spaces according to the increase in the IL volume. Thus, the variation in the open mesoporous structure (>3 nm) corresponding to the IL/SiO_2 molar ratio was characterized based on the analysis of the N_2 adsorption/desorption measurements. Figure 2.3 shows the positron

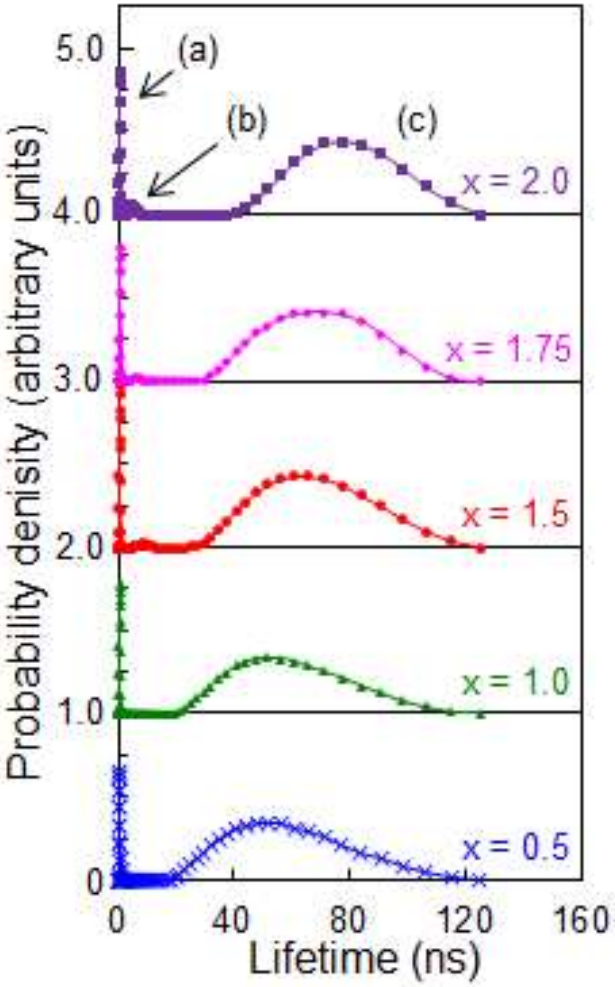

Fig. 2.4 Probability density function (PDF) of the annihilation rate obtained by the numerical Laplace inversion technique for IL-templated porous silica with an IL/SiO_2 ratio in the range of 0.5–2.0. "x" denotes the IL/SiO_2 molar ratio of the samples. The three observed peaks are denoted as (a), (b), and (c). Reproduced with permission of ref.[82] Copyright 2020, Elsevier Inc.

annihilation lifetime spectra of the IL-templated porous silica with an IL/SiO_2 molar ratio of 1.5. In porous materials, a portion of the injected positrons forms a positron–electron bound state, which is called Positronium (Ps) [44, 45]. The Ps with the singlet spin state (antiparallel) is called para-Ps (*p*-Ps), and it annihilates with the emission of two quanta with a short lifetime of 0.125 ns (in vacuum) [85]. Given that this component does not reflect the information of open spaces, it will not be discussed further in this paper. In contrast, the Ps with the triplet spin state (parallel) is called ortho-Ps (*o*-Ps), and it emits the three quanta during annihilation in the vacuum. As the intrinsic lifetime of *o*-Ps is 142 ns (a thousand times longer than that of *p*-Ps) [85], it diffuses into the open spaces and survives for a longer period compared to *p*-Ps. However, in a condensed matter with small pore structures, a portion of the positrons in *o*-Ps annihilates with the electrons at the pore surface according to the two-quanta emission process with a lifetime of a few tens of ns ("pick-off" process) [86]. As this annihilation process is sensitive to small variations in the electron density, the small-sized pores in the samples can be characterized by analyzing the behavior of *o*-Ps annihilation. To analyze the details of the *o*-Ps annihilation behavior, a numerical Laplace inversion analysis was conducted for the measured spectra using the CONTIN program [75–78]. Figure 2.4 shows the PDF of the annihilation rate for the IL-templated porous silica with different IL/SiO_2 compositions. The three distinguishable peaks are observed in the lifetime region of (a) 0.2–1.4 ns, (b) 2–14 ns, and (c) 15–120 ns. The peak with the shortest lifetime of 0.4–1.0 nm is attributed to the mixture of the annihilation of free positron, *p*-Ps, as well as *o*-Ps. Annihilation with 0.4-0.5 ns has been observed in SiO_2 synthesized via the sol-gel process [87,88]. It is known to be due to positron annihilation without the formation of positronium in the vacancy clusters in amorphous SiO_2 [89,90].

In contrast, annihilation with a relatively larger lifetime of 0.5–0.8 nm has been

reported in sol-gel prepared SiO_2 [91]. This value corresponds to the annihilation lifetime of free positron and *o*-Ps in the microvoids, which are created by the electron and/or neutron irradiation to amorphous SiO_2 [92,93]. Although it is difficult to resolve each component, owing to the limitation of spectrometer resolution and the deconvolution technique, the (a) peaks in Fig. 4 are a result of the positron annihilation in the open-volume structure of the amorphous network of SiO_2. Components (b) and (c) are explained by the annihilation of *o*-Ps because their lifetimes are much longer than the intrinsic lifetime of *p*-Ps (0.125 ns). The lifetime of component (b) is approximately 2–14 ns, and has a similar value as that observed for highly porous silica gel powders [94]. It originates from the pick-off annihilation of *o*-Ps trapped in the small pores between the primary silica particles. The longest lifetime component (c) with a lifetime of 15–120 ns is considered to be due to the annihilation of *o*-Ps in pores with larger sizes [94–96]. The other components with higher lifetimes (> 130 ns) could not be obtained from the spectra. This result is the same as the fitted results in Fig. 2. This means that most of the injected positrons are annihilated in the relatively smaller sized pores before they are trapped by the large open spaces (200–400 nm), which can be detected by SEM. The PALS characterization technique is sensitive to the small open spaces, which are less than a few tens of nanometers in size.

Figure 2.5 compares the PDF spectra at different IL/SiO_2 compositions in the three lifetime regions. The peaks with the shortest lifetimes are shown in Fig. 2.5 (a). In this region, the lifetime did not change in materials with different IL/SiO_2 ratios; i.e., the size of the vacancy clusters and/or microvoids were not influenced by the IL/SiO_2 ratio. Therefore, I mainly focused on the long lifetime components, (b) and (c), for characterizing the variation of pore structure with different IL/SiO_2 ratios. If the pore shape is assumed to be spherical, the pore diameter can be estimated from the *o*-Ps

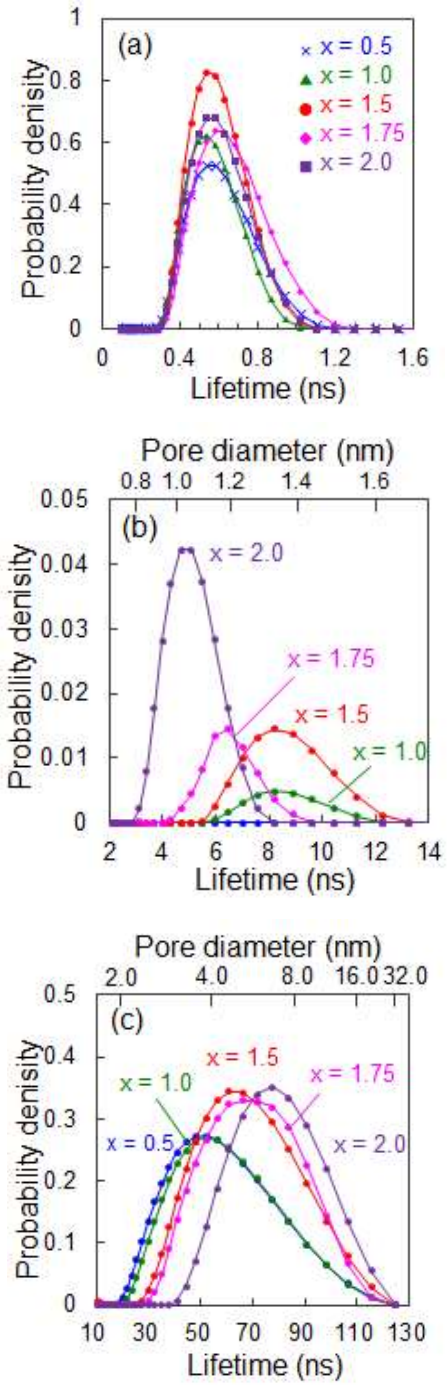

Fig. 2.5 Probability density function (PDF) of annihilation rate obtained by the numerical Laplace inversion technique for IL-templated porous silica with IL/SiO_2 ratios in the range of 0.5–2.0 in the three lifetime regions. "x" denotes the IL/SiO_2 molar ratio of the samples. The pore diameter was calculated and is shown in the upper horizontal axis of (b) and (c). Reproduced with permission of ref.[82] Copyright 2020, Elsevier Inc.

lifetimes using the ETE model [42, 43]. The calculated pore diameter is shown in the upper horizontal axis in Figs. 2.5 (b) and (c). Figure 2.5 (b) shows the positron lifetime distribution of the PDF in the 2–14 ns region. As observed in Fig. 2.5 (b), the pore diameter varied between 1.0 and 1.4 nm. This is the typical size of pores between primary silica particles in porous SiO_2 prepared by the sol-gel process [94]. Note that the pores in this size range cannot be detected by standard N_2 adsorption/desorption techniques. For samples with x = 0.5, no signal was detected in this lifetime region, indicating that the open space between primary silica particles was closed, i.e., a dense network of SiO_2 was formed in the silica matrix. For the sample with x = 1.0, the peaks appeared at 8 ns (pore diameter = 1.4 nm). Upon increasing the IL/SiO_2 molar ratio from 1.0 to 1.5, the probability density of the annihilation rate increased owing to the maintenance of the pore diameter at approximately 1.4 nm. This indicates that the number of pores increased owing to the expansion of the open spaces occupied by IL with an increase in the IL/SiO_2 ratio. Meanwhile, the pore diameter decreased as the IL/SiO_2 molar ratio increased from 1.5 to 2.0; i.e., the length of the pores between the primary silica particles decreased from 1.4 to 1.0 nm. This might be related to the sizes of the primary silica particles.

The sizes of the silica particles decreased in samples with higher IL/SiO_2 ratios, owing to the small volume of TEOS compared to IL. As a result, the space between the silica particles decreased. The threshold IL/SiO_2 ratio appears to be 1.5. In contrast, the probability density increased with increasing IL/SiO_2 ratios. This indicates that the number of pores increased according to the reduction in the pore size and the expansion of the open spaces occupied by IL. The probability density was found to be 10 times smaller than that of the other peaks. Thus, these pore types are not dominant in the samples. However, the pores in this size range (1–2 nm) are important for the selection of organic molecules and for controlling the mechanical properties of the material.

The peaks with the longest lifetimes are shown in Fig. 2.5 (c). The pore diameter is distributed from 2.0 to 40 nm in this lifetime region. The lifetime increased as a function of the IL/SiO_2 ratio. Additionally, the pore diameter at the peak increased from 4 to 7 nm. This variation is consistent with the results of the N_2 adsorption/desorption measurements, especially with the results of the desorption branch analysis presented in Fig. 2.2 (c) (3.8–7.6 nm). This clearly indicates that the pores detected in Fig. 2.5 (c) are the same as the mesopores that were characterized by SEM, TEM, and N_2 adsorption/desorption. As shown in Fig. 2, this pore size variation can be explained by the expansion of the open space according to the increase in the IL volume. Therefore, the PALS technique can characterize various types of open spaces, not only mesopores (>2 nm) but also micropores (<2 nm), and can reveal the variation in the structure of these pores according to the variation in the IL/SiO_2 ratio.

A schematic of the pore structure variation of the IL-templated porous silica corresponding to the IL/SiO_2 ratio is presented in Fig. 2.6. In the IL-templated porous SiO_2 with x = 0.5, vacancy clusters, microvoids, and mesopores (4 nm) exist. Upon increasing the IL/SiO_2 ratio to x = 1.0, micropores (1.4 nm) are created in addition to vacancy clusters, microvoids, and mesopores. This is because the space occupied by IL of increased IL content, as mentioned above. However, the size and number of mesopores increased with increasing IL content. In contrast, the size and number of mesopores did not change, indicating that IL molecules tend to gather into small clusters during the sol-gel process in the range of this IL/SiO_2 ratio. The templated IL has a small influence on the creation of mesopores at this IL content. For the sample with x = 1.5, the size was comparable to that of the sample with x = 1.0. This can also be explained by the effects increased as compared to those of the sample with x = 1.0 (5 nm). This implies that IL molecules started to form larger clusters during the sol-gel process, leading to the

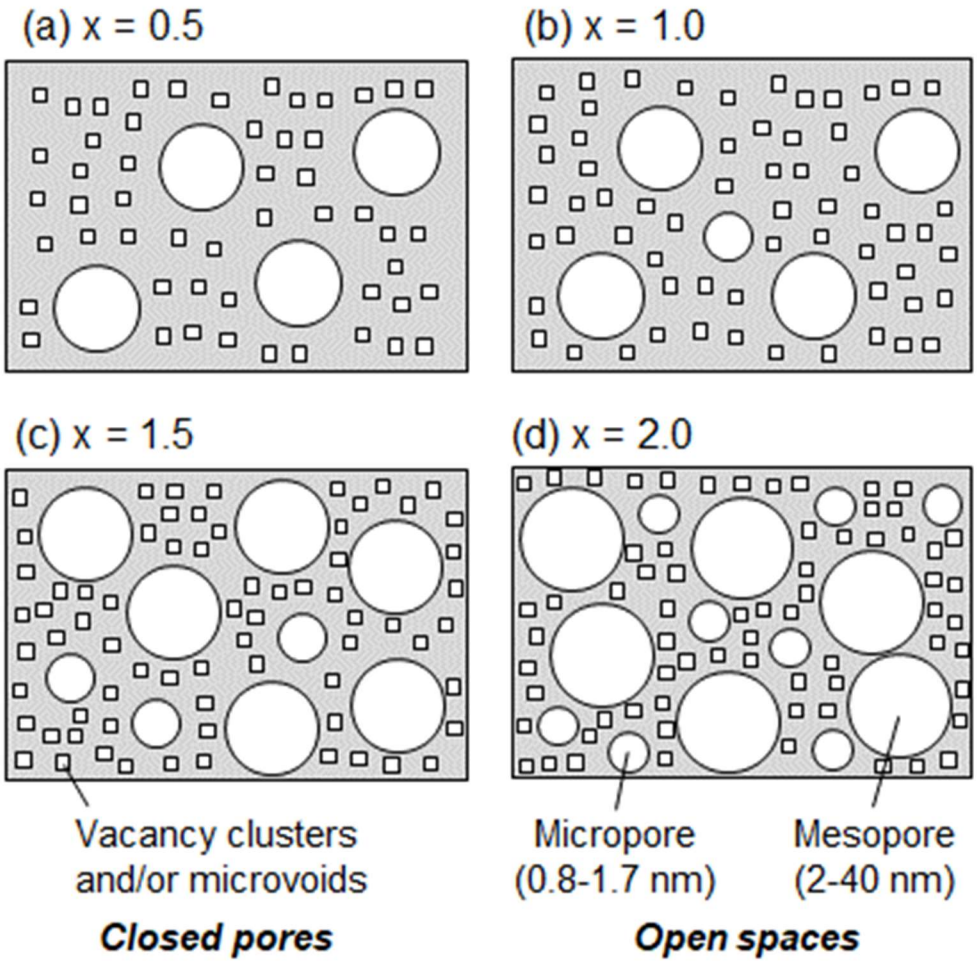

Fig. 2.6 Schematic of the pore structure of IL-templated porous silica with an IL/SiO_2 ratio in the range of 0.5–2.0. (a) x = 0.5, (b) x = 1.0, (c) x = 1.5, (d) x = 2.0. "x" denotes the IL/SiO_2 molar ratio of the samples. Reproduced with permission of ref.[82] Copyright 2020, Elsevier Inc.

formation of larger mesopores. Upon increasing the IL/SiO_2 ratio from 1.5 to a higher value, the number of micropores increased, although the size of the micropores decreased (1.0 nm with x = 2.0). These results are due to the suppression of the creation of the silica network and a reduction in the size of the primary silica particle due to decreased TEOS content. In contrast, the size and number of mesopores increased with higher IL/SiO_2 ratios (7 nm at x = 2.0). In the sample with x = 2.0, a highly sparse structure was created

with a large number of micropores and larger mesopores.

2.4 Conclusion

In this study, I clarified the pore structures of IL-templated porous silica using the PALS technique. PALS can be used to characterize open spaces with diameters below 2 nm, which is otherwise difficult to analyze using standard methods for pore structure determination, such as SEM, TEM, SAXS, SANS, and N_2 adsorption/desorption experiments. PALS analyses revealed that IL-templated porous silica samples have three types of pores: (1) vacancy clusters and/or microvoids (closed pores), (2) micropores between primary silica particles in the porous SiO_2 (1.0–1.4 nm), and (3) mesopores with side lengths in the range of 4–7 nm. Upon increasing the IL/SiO_2 ratio, the sizes of the spaces between the primary particles decreased from 1.4 nm to 1.0 nm. This is related to the size of the silica particle, which decreased owing to the small volume of TEOS (SiO_2) compared to that of IL. As for the larger mesopores, their size increased at higher IL/SiO_2 ratios, indicating that the open space expanded according to the increase in the IL volume. Thus, the PALS method allowed us to comprehensively understand the pore structure of IL-templated porous SiO_2. In the future, these findings on the relationship between pore structure and IL content will be used for optimizing the mechanical properties and chemical selectivity.

Chapter 3

Ion Conduction behaviour in the Nanopores in Silica-gel Solid Nanocomposite Electrolytes

3.1 Introduction

All-solid-state batteries (ASSBs) with solid electrolytes (SEs) are epoch-making energy storage devices beyond conventional lithium-ion batteries because SEs can remove the risks of electrolyte leakage, volatilization, flammability and explosion. To realize high-energy and high-power performance as well as high-safety, SEs with fast lithium-ion conduction and good interfacial contact with the electrodes are expected to be developed. Recently, Xubin et al. developed a novel solid nanocomposite electrolyte (nano-SCE) composed of ionic liquid (IL), Li-salt and porous silica using sol-gel method[31]. This electrolyte ensures battery safety because of the non-volatility, thermal and electrochemical stability. Furthermore, a liquid precursor can be impregnated into the powder electrodes, which potentially forms a good interfacial contact between the electrode and the electrolyte. More interestingly, nano-SCE shows the promotion of the Li-ion conductivity on the silica pore wall. The strong hydrogen bonding between the surface ice-water and the IL molecules induces molecular ordering of IL anions and cations. This interfacial interaction weakens the association between the Li-ion and its anion, thereby enhancing the ionic conductivity well beyond that of pure IL electrolyte. In order to achieve higher conductivity and realize the high-power performance, the fundamental understanding of the Li ion conduction behavior in the pores is necessary. It

is important to evaluate the behavior of Li ion conduction in the pores, in order to design the ideal porous structure of nano-SCEs, towards improving the ionic conductivity. In other words, the effect of the silica nanostructure (pore size, surface area, porosity) on the surface conduction promotion phenomena and confinement effect must be understood. However, it is difficult to characterize the silica matrix structure itself in nano-SCEs because the silica structure collapses by the surface tension when the ILE is removed by rinsing with solvents such as ethanol and acetone and after drying, both in ambient and vacuum.[82] To maintain the nanostructural integrity of the silica matrix and characterize its properties, ILE should be removed without any damage to the original silica structures.

In this section, I have extracted and characterized the pore structure of nanoporous silica matrix using CO_2 supercritical drying (SCD) method. This method is generally used for the fabrication of aerogels[97,98] to extract ILE from SCEs. The porous structures were analyzed by scanning electron microscopy (SEM), transmission electron microscopy (TEM), and N_2 adsorption/desorption measurements. In addition, the positron annihilation lifetime spectroscopy (PALS) was performed to study the small size and closed pore structures, which is typically difficult to characterize with N_2 adsorption/desorption analysis.[64,65] The PALS analysis is widely used for evaluating vacancy-type defects and open volume in semiconductor materials.[66,67] Additionally, it has been successfully applied in silica aerogels.[95] The variation of the porous structure with different IL/SiO_2 material ratio was studied with the aid of several analytical techniques. Moreover, the degree of surface conduction promotion and pore confinement were estimated from the variation in conductivity of nano-SCEs. The relationship between pore structures and conduction behavior was also investigated.

3.2 Experimental

3.2.1 Synthesis of nano-SCE pellets

The nano-SCE monolith was prepared using a templated sol-gel process; the mesoporous silica matrix was formed by slow hydrolysis-condensation reaction of TEOS as SiO_2 precursor with ILE as a template, for the condensation of the interconnected hydrated silica network.[31] Lithium bis(trifluoromethylsulfonyl)imide (Li-TFSI, 99%, Solvay), 1-butyl-1-methylpyrrolidinium bis(trifluoromethylsulfonyl)imide (BMP-TFSI, 98.5%, Sigma Aldrich), tetraethyl orthosilicate (TEOS, 98%, Sigma Aldrich), deionized water (DIW) and 1-methoxy-2-propanol (PGME, 99.5 %, Merck) were mixed in a glass vial. Here, the molar ratio between BMP-TFSI and TEOS (hereafter referred as "x") in the mixture was varied between 1.0 and 2.0, while the molar ratio of Li-TFSI and BMP-TFSI was fixed at 1:3 (equivalent to a 1M Li-TFSI ILE solution). The amounts of Li-TFSI and BMP-TFSI were determined from these ratios. For example, when x = 1, the added BMP-TFSI and Li-TFSI in the solution were 0.97 g and 0.22 g, respectively. The volume of TEOS, DIW, and PGME were fixed at 0.5 mL, 0.5 mL, and 1 mL, respectively. Unlike the typical formic acid catalyzed ionogel recipes,[24,26,27,29] a mixture with a mild pH of 5 with excess of water and PGME added to TEOS with ILE were used. This is because the hydrolysis reaction is slow, whereas the condensation reaction is favorable at this pH.[69] The Li-ions are believed to act as catalysts for the hydrolysis reaction, as no gelation occurred in the absence of the lithium salt while both had the same pH of 5. The mixtures were shaken for 1 min to form monophasic solutions. These solutions

were then stored without stirring to form gels at 25 °C and 50 %RH in a climate chamber (SH-641, Espec corp.). After allowing gelation for 2 to 4 days, the open vials were first dried at 40 °C for 4 days at a slightly reduced pressure (80 kPa) and then moved into a vacuum oven for 72 h at 25 °C (< $5x10^{-2}$ mbar). The weight of the resulting gels was measured with a semimicro balance (SM 1245Di-C, VWR). As a liquid reference, a pure ILE, a simple mixture of BMP-TFSI and Li-TFSI was prepared in the Ar-filled glovebox (O_2, H_2O <0.1 ppm), i.e., without air exposure.

3.2.2 Removing ILE from nano-SCE pellets

The open porous-silica matrix (aerogel) was prepared by removing the ILE fraction from the nano-SCE pellet using SCD.[97,98] First, nano-SCE pellet were immersed in ethanol at 40 °C for 12 h to exchange ILE by ethanol. This procedure was repeated three times, that is, the samples were soaked for 36 days in total. Subsequently, they were transferred into a CO_2 critical point drying chamber (SCF-201, JASCO) that was filled with ethanol and sealed tightly. The drying sequence started with a decrease in temperature to -5 °C. Subsequently, CO_2 gas was purged through the chamber at a flow rate of 2 mL/min until the pressure was 12 MPa and then heated to 70 °C, which is higher than the supercritical point of CO_2 (7.38 MPa and 31.1 °C).[97,98] At this stage, supercritical CO_2 flow was continued at 2 mL/ min for 5–6 h to replace all the ethanol with CO_2. Finally, the pressure was decreased slowly in intervals from 12 to 7 MPa, 7 to 3 MPa, and 3 to 0 MPa over time spans of 10, 60, and 10 minutes, respectively. After cooling down to room temperature, the samples were transferred to an Ar-filled glove box (oxygen <0.1 ppm, water <0.1 ppm) and stored in a closed vial. For comparison, a sample with

the standard drying technique was prepared. The nano-SCE was soaked in acetone for 36 h (12 h x 3) to extract the ILE, and then dried in ambient for 4 h at 60 °C to dry the excess solvent.

3.2.3 Imaging of the SCE and silica matrix

The morphology of the nano-SCE pellet, with and without ILE, were investigated by SEM and TEM. SEM was done using a Thermo-Fisher Apreo tool with the acceleration energy in the range of 1.5–2.0 keV and dual-detector imaging mode using the T1 and T2 detectors in parallel for live image adjustments and the T2 detector for recording the SEM images. The sample was fixed on a conductive carbon tape. TEM was done using JEM-ARM200F at 200 keV and the sample was fixed on a copper micro grid.

3.2.4 Density measurement

The specific density of the nano-SCE (ρ_{SCE}) and ILE (ρ_{ILE}) were determined by N_2 gas pycnometer (micromeritics, AccuPyc II 1340). The true density of porous silica after extracting ILE and drying (ρ_{silica}) was measured by H_2 gas pycnometer (Quantachrome, UltraPyc 1200e).

3.2.5 Nitrogen Adsorption and Desorption

The obtained porous silica after ILE removal was outgassed for 4 h at 40 °C under a 0.1 mbar vacuum. Nitrogen physisorption isotherms were then measured

at T=77 K using an Autosorb 3 analyzer. The surface area was extracted from the adsorption isotherm with Brunauer-Emmett-Teller (BET) theory, which is based on a model that describes the amount of gas adsorbed on a silica surface as a function of pressure.[62,71,99] The pore size distribution was analyzed with the Barret-Joyner-Halenda (BJH) method.[72] The porosity of the silica matrix (P) was determined by eq. (3.1)

$$P = \frac{V_{pore}}{V_{Pore}+V_{silica}} \times 100 = \frac{V_{pore}}{V_{Pore}+1/\rho_{silica}} \times 100 \quad (3.1)$$

where V_{pore} (cm^3/g) is the specific total pore volume obtained from the isotherms plot, and V_{silica} (cm^3/g) is the specific volume of silica matrix, which is the inverse of the silica matrix density as determined above.

3.2.6 Positron Annihilation Spectroscopy

PALS was carried out using a conventional lifetime system with digital oscilloscope (LeCroyWavepro), as described by A. Uedono et al.[73] The positron source was prepared by the deposition and drying of aqueous $^{22}NaCl$ (radioactivity of ~500 kBq) on the Kapton polyimide foils and then covering it with another Kapton foil. Subsequently, the positron source was sandwiched between two identical samples, which were prepared by packing the samples in the central dip of the acrylic holders (4.5 mm in diameter, 3 mm thick), and then placing them into the vacuum chamber (10^{-3} Pa). The positron beam was irradiated through the whole sample (in 3 mm thick). To prevent backscattering of γ-rays by the scintillators, the two detectors were positioned perpendicular to each other. All the

measurements were conducted at room temperature. The full width at half maximum (FWHM) of the time resolution of the system was ~230 ps and the time calibration constant was 102.7 ps/ch. The total number of accumulated counts was in the range of 4×10^6 to 8×10^6 for each lifetime spectrum. Herein, the lifetime spectrum $S_{LT}(t)$ is given by eq. (3.2).

$$S_{LT}(t) = \sum \lambda_i I_i \exp(-\lambda_i t) \quad (3.2)$$

where λ_i and I_i are the annihilation rate and intensity of positrons of i^{th} component, respectively.[73] The lifetime of positrons τ_i is given by $1/\lambda_i$. The number of lifetime components is determined by deconvoluting the spectra with a time resolution of approximately 190 ps using a computer program called RESOLUTION.[100] The pore size of the samples was estimated from the lifetime of each component using the extended Tao–Eldrup (ETE) model, which is a quantum mechanical model established by Gidley et al.[80,101] The EELViS calculator was used for this estimation.[81]

3.2.7 Conductivity measurement of nano-SCE

The ionic conductivity of the nano-SCE pellets was determined by electrochemical impedance spectroscopy (EIS) measurements on a small volume (23 μl) of the synthesized pellets that was placed in a polytetrafluoroethylene (PTFE) ring. The filled ring was sandwiched between two stainless steel (SS) disks WITHOUT sealing in a coin cell (CR2032, MTI) to dry further in the glovebox

(O_2, H_2O <0.1 ppm). The effect of "drying" on the conductivity was determined using these samples. For impedance measurement, the AC amplitude was set at 5 mV and the frequency range was from 1 MHz to 1 Hz. The ionic resistance of the nano-SCE was determined from the intercept of the high frequency with the real axis in the Nyquist plots and the dimension of the inner ring filled with nano-SCE. The conductivity measurements were done with a potentiostat (PGSTAT302N, Autolab) combined with a frequency response analyzer (FRA32M, Metrohm) controlled through Nova software. The details of the measurements was described by Chen et al.[31]

3.3 Results and discussion

In order to characterize the pore structures, the ILE was extracted from nano-SCE, with x = 1.0, 1.5, and 2.0 by CO_2 SCD methods. For comparison, ILE extracted nano-SCE samples (x = 1.5) that were simply dried in ambient air were also prepared. The optical images of nano-SCE (x = 1.5) at each step of the ILE removal process are shown in Fig. 3.1. First, a transparent nano-SCE pellet was prepared by following the procedure described in the experimental section (Fig. 3.1(a)). The pellet diameter was approximately 1.8 cm. Next, the ILE in the nano-SCE was exchanged by ethanol. The pellet appearance changed from clear to opaque after replacing the solidified ILE by liquid ethanol in the pores. However, the pellet size and volume remained unchanged, even after the exchange (Fig. 3.1(b)) due to the solid monolithic nature of the silica matrix.[31] After careful drying beyond the critical point of CO2, intact aerogel monoliths, i.e., porous silica

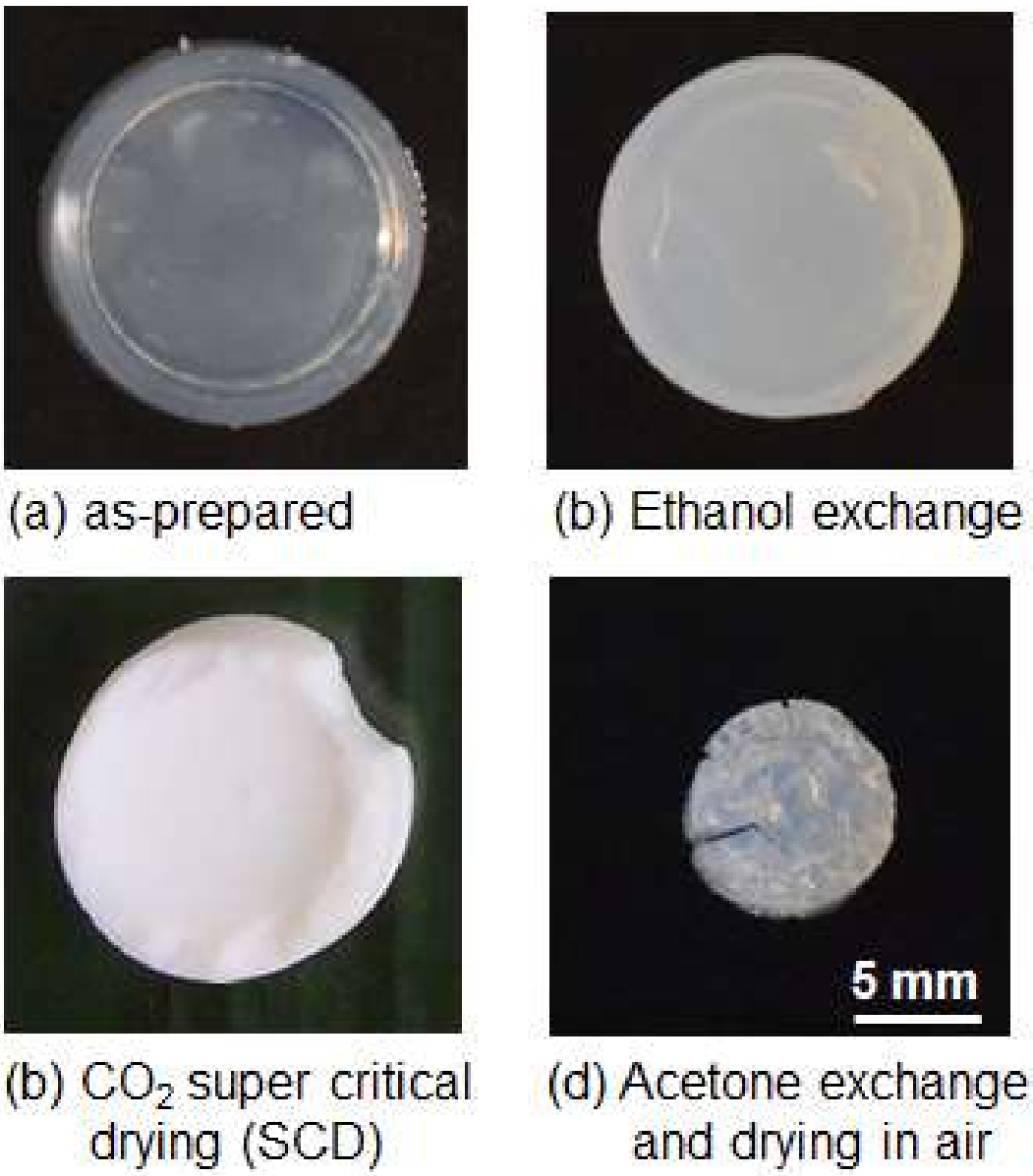

Fig. 3.1 Pictures of nano-SCE pellets at each step of the ILE removal process (ILE/SiO_2 = 1.5) (a) as-prepared pellet (without additional process). (b) The pellet after soaking in ethanol for 36 h at 40 ºC. (c) The pellet after soaking in ethanol for 36 h at 40 ºC and then drying by CO_2 super critical drying method. (d) The pellet after soaking in acetone for 36 h at RT and then drying in ambient at 60 ºC. Reprinted with permission from ref.[102] Copyright 2021, American Chemical Society.

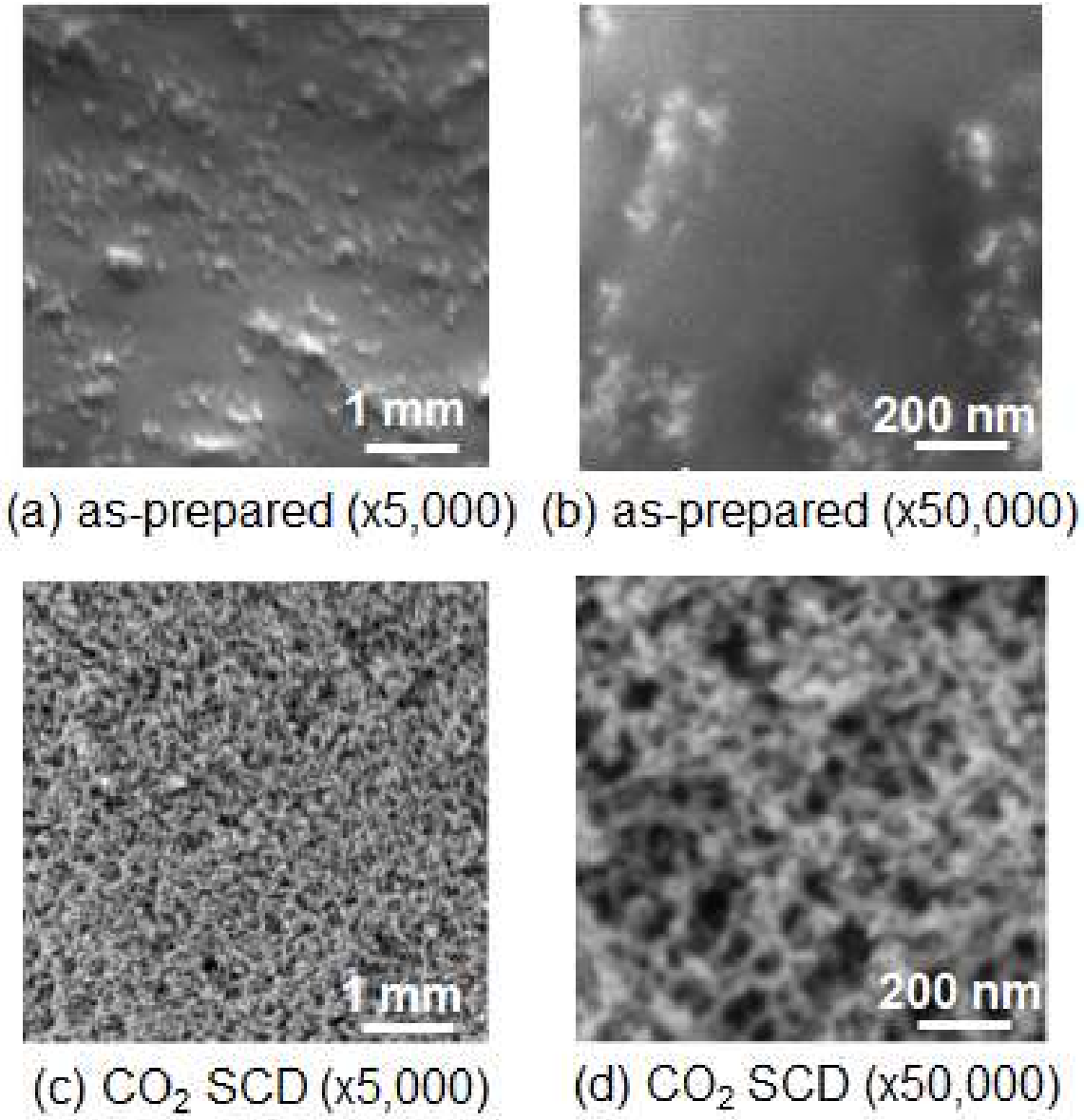

Fig. 3.2 SEM images of the nano-SCE with ILE/SiO_2 molar ratio of 1.5 and porous silica matrix which was obtained by removal of ILE. (a), (b) as-prepared pellet (nano-SCE). (c), (d) The porous silica which remains after soaking in ethanol for 36 h at 40 ºC and subsequent drying by CO_2 super critical drying method. Reprinted with permission from ref.[102] Copyright 2021, American Chemical Society.

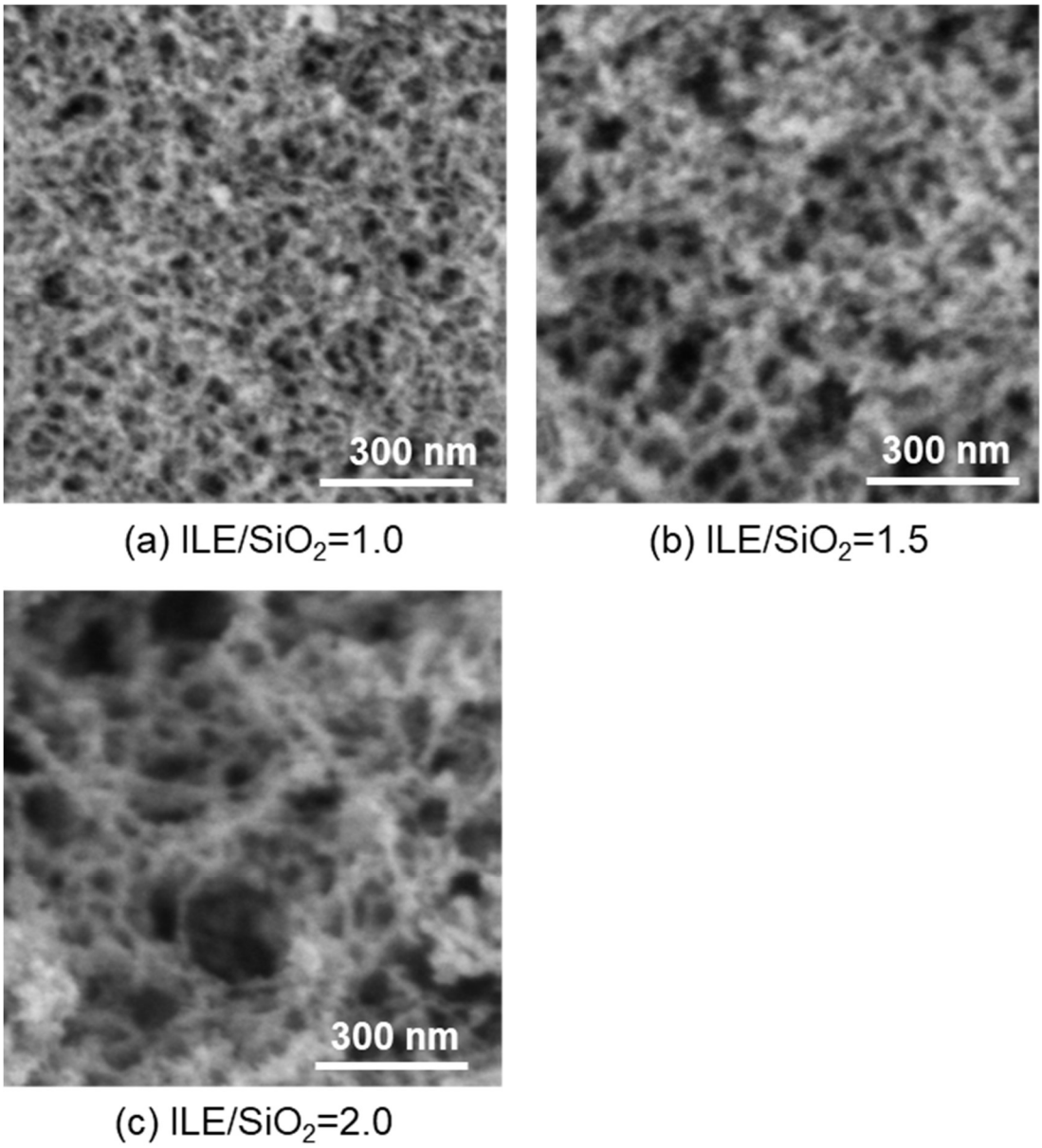

Fig. 3.3 SEM images of the porous silica matrix which was obtained by removal of ILE from the nano-SCEs. (a) ILE/SiO_2 = 1.0. (b) ILE/SiO_2 = 1.5. (c) ILE/SiO_2 = 2.0. ILE was collapsed almost completely during (ambient) drying due to the surface tension between the shrinking acetone fraction and the large internal silica surface. Reprinted with permission from ref.[102] Copyright 2021, American Chemical Society.

matrix, was obtained (Fig. 3.1(c)). The color became white due to the scattering of light by the random pore structures. However, no significant change in the size and volume of the pellets was observed after CO_2 SCD. Even though some change in pore structure cannot be excluded, I expect that most of the original silica matrix structure remained intact. In contrast, after soaking in acetone and drying in ambient conditions, the pellet size had reduced more than half in size with a diameter of approximately 8 mm (Fig. 3.1 (d)). In this case, the pore structure

Figure 3.2 shows the SEM images of the nano-SCE with x = 1.5 before and after ILE removal. The nano-SCE indicated no clear microstructure, except for some patched of smooth amorphous-like morphology randomly distributed (Fig. 3.2 (a) and (b)). I believe these patches are silica matrix. The full silica matrix was revealed after the extraction of ILE by CO_2 SCD. A dense scaffold of mesoporous silica with 10–30 nm diameter pores is observed, intersected by occasional larger macropores of 100–150 nm (Fig. 3.2 (c) and (d)).

removed by soaking in ethanol for 36 h at 40 °C and subsequent drying by CO_2 super critical drying method.

Figure 3.3 shows the comparison of the silica matrix structure with increasing ILE/SiO_2 content: x = 1.0, 1.5, and 2.0. In the porous silica with x = 1.0, the size of the pores was small (<70 nm) and relatively uniform. With increasing ILE/SiO_2 ratios of x = 1.0 to 2.0, more macropores appeared in the silica scaffold and their pore size became larger. This can be explained by the increase of the ILE volume fraction, which occupies a larger fraction in the nano-SCE. The larger volume fraction can be accommodated by either more pores and/or larger pore size.

A high-resolution TEM image of the sample with x =1.5 is shown in Fig. 3.4. The silica scaffold microstructure is made up of silica nanoplatelets of

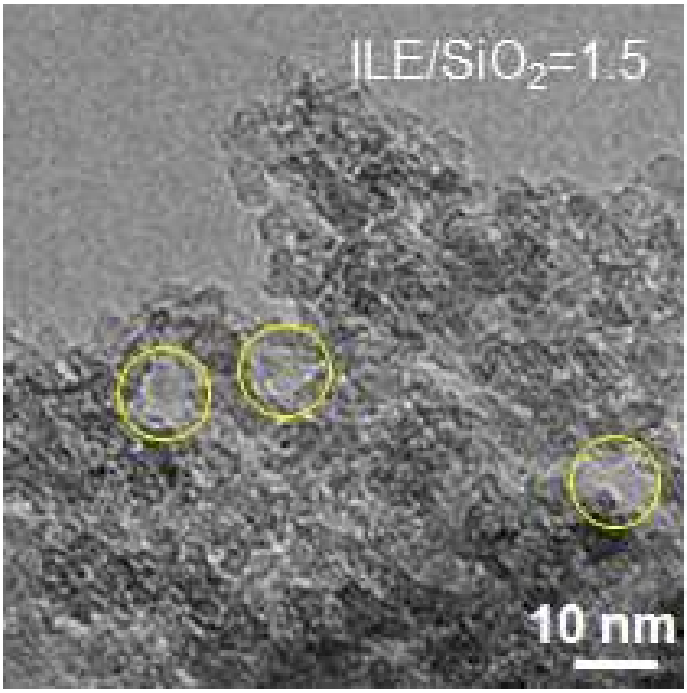

Fig. 3.4 TEM image of the porous silica matrix which was obtained by removal of ILE from the nano-SCE with ILE/SiO_2 molar ratio of 1.5. ILE removal was done by soaking in ethanol for 36 h at 40 ^oC and subsequent drying by CO_2 super critical drying method. Reprinted with permission from ref.[102] Copyright 2021, American Chemical Society.

approximately 7–10 nm. Unfortunately, the mesoporous character observed in the SEM images is not preserved in the TEM images owing to the sample preparation by drop casting and drying on the TEM carbon lace grid. Hence, it is seen that an image of a densified structure where the silica nanoplatelet building blocks are bound together. Nevertheless, upon carefully inspection, (more) open spaces can be observed in a few positions (indicated by yellow circles), which are the remnants of pores. The diameter of the pores is estimated to be approximately 8–9 nm. This corresponds to the smallest sized pores, which can be seen by SEM in Fig. 3.3 (b).

However, it is difficult to determine the pore size and their distribution by TEM as the pore was overwrapped with the electron transmission axis.

N_2 adsorption/desorption measurements were done to characterize the pore size and its distribution, and calculate the specific surface area (BET surface area) and porosity of the open porous silica aerogel matrix. Figure 3.5 (a) shows the isotherms of the nano-SCEs after ILE removal and drying. All data indicate the hysteresis with N_2 adsorption branch (bottom line) and N_2 desorption branch (top line), but the plot shape was different depending on the sample preparation conditions. The plots of the air-dried sample with x = 1.5 and SCD sample with x = 1.0 show a relatively clear hysteresis. This behavior can be classified into the typical type-IV category indicating that a mesoporous structure (2–50 nm) is dominant in the sample as defined by the International Union of Pure and Applied Chemistry (IUPAC).[62,71] In contrast, the hysteresis was flat in the SCD samples at higher ILE/SiO_2 (x = 1.5 and 2.0). This behavior can be explained by an overlap of a type-II shape, which is indicative of a macroporous structure (>50 nm), and type-IV of a mesoporous structure. This confirms that a larger pore size co-exists with a mesoporous structure in these samples as observed with SEM.

Figures 3.5 (b) and (c) show the pore size distributions analyzed by BJH method assuming a cylindrical pore.[72] The pore size distribution obtained from the adsorption branch (Fig. 3.5 (b)) reflects the pore size of the wider part of the cylindrical pore, and that of the desorption branch (Fig. 3.5 (b)) reflects the size of the narrow part of the cylindrical pore. Upon comparison the SCD and ambient drying samples at a fixed ILE/SiO_2 ratio (x = 1.5), it was observed that the pore size and number density for the sample dried in air was much smaller than that of the SCD fabricated aerogels. This confirms that the pore structure collapsed during

ambient drying as expected. Whereas all SCD samples have comparable pore sizes in Fig. 3.5 (b) and (c). The pore size distribution for the x = 1.0 aerogel is distinctively narrower than that for the higher x-values, confirming the presence of relatively small and uniform pores in this sample as observed by SEM (Fig. 3.3 (b)). Note that the lower cut-off value for the pore size was set at 3 nm; thus, the actual average pore size might even be somewhat lower. The pore size of the SCD samples with x = 1.0 was smaller than 30–90 nm with a peak density of 15–25 nm pores (Fig. 5 (b) and (c)). The maximum pore size and pore size distribution becomes larger with increasing ILE/SiO_2 molar ratio due to the increase of ILE volume, i.e., the space occupied by ILE in the nano-SCE. Pore sizes as large as a few hundred nanometers with a peak density around 40–80 nm were measured for SCE samples with x = 1.5 and 2.0. This is also in accordance with the SEM results (Figs. 3 (b) and (c)). However, the total number of pores in the SCE sample with x = 2.0 seems lower compared to that of x = 1.5. This could be due to the partial collapse of the pores after CO_2 drying, as the silica network might not be strong enough to withstand forces of water adsorption from air.

The BET surface area and porosity is summarized in Table 3.1. The porosities of the samples were calculated from the total pore volume and true density of porous silica using eq. (1).[99] For comparison, the volumetric ratio of ILE (V_{ILE}) to nano-SCE (V_{SCE}) was determined by eq. (3) and summarized in Table 3.1.

$$\frac{V_{ILE}}{V_{SCE}} = \frac{w_{ILE}/\rho_{ILE}}{w_{SCE}/\rho_{SCE}} \tag{3.3}$$

where w_{ILE} and w_{SCE} are the weight (g) of the combined materials in the reacted

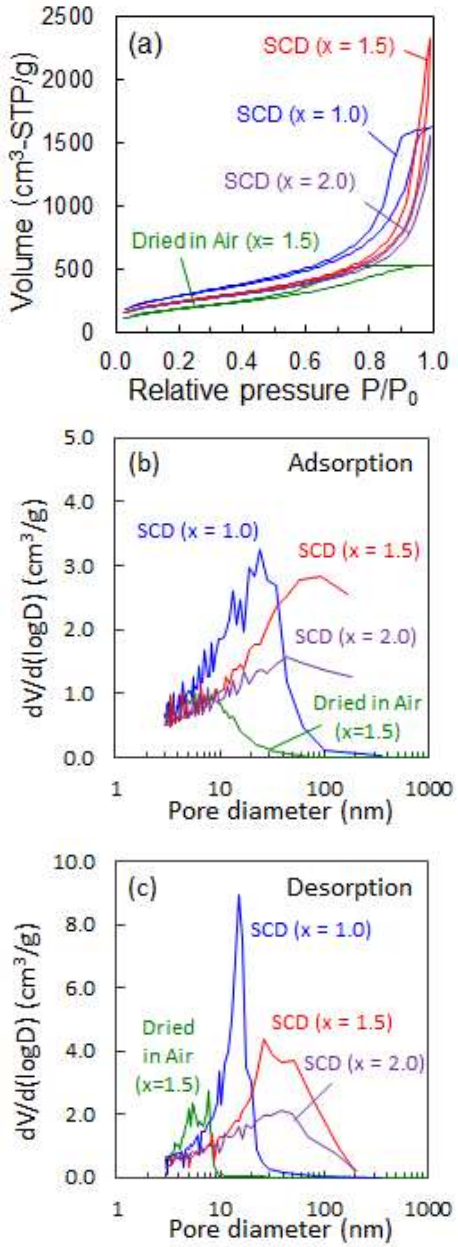

Fig. 3.5 N_2 adsorption/desorption measurement results of the porous silica matrix which was obtained by removal of ILE from the nano-SCEs. (a) Isotherm. (b) log differential pore size distribution which is analyzed by adsorption part of the isotherm using BJH method with an assumption that the pores in the silica are cylindrical in shape. (c) log differential pore size distribution which is analyzed by desorption part. "x" denotes the ILE/SIO_2 molar ratio of the samples. Reprinted with permission from ref.[102] Copyright 2021, American Chemical Society.

sol-gel precursor solution, and ρ_{ILE} and ρ_{SCE} are the measured density of ILE and nano-SCE (g/cm^3). The volumetric ratio in (3) expresses the space occupied by ILE in the nano-SCE and thus, in principle, is equal to the porosity of the silica matrix. Note that the calculation is done under the assumption that the density of pure ILE is the same as that of the ILE confined in the pores of the nano-SCE. As he ILE molecules form a solid, adsorbed and molecular ordered nanocomposite with the silica, the density of the ILE fraction is likely to be slightly higher; thus, the actual volumetric ratio is slightly smaller, as indeed discovered (Table 3.1). On the contrary, the density of the confined ILE in the sample x =1.5 can be extracted: 1.56 g/cm^3 or 5.4 % larger than bulk ILE density (1.48 g/cm^3). The surface area and porosity of sample under ambient drying (x = 1.5) was lower than that of the SCD sample; however, not as much as one would expect from the near 100% volume reduction. Hence, the pore structure is indeed partially collapsed. However, the large shrinkage is also the result of a strong reduction in pore size, which was also inferred from the pore size distribution in Fig. 3.5 (b) and (c). For the SCD sample, the surface area decreased with increasing ILE/SiO_2 ratio from 1050 m^2/g for x = 1.0 to 850 m^2/g for x = 2.0. Conversely, the pore volume reaches a maximum for x = 1.5. Hence, an optimum ILE/SiO_2 ratio seems to be reached at this point. For higher x, there is insufficient silica to form more walls. Indeed, larger pores containing liquid ILE are likely to be formed for higher x-values as discussed in Fig. 3.5. From the ratio of pore volume to surface area, an average pore size of 9.6 nm, 15.8 nm and 11.4 nm is expected for x = 1, 1.5 and 2, respectively. However, the average silica wall thickness reduces to less than 2 nm from x = 1.5; thus, confirming that there is insufficient silica to form the matrix. Therefore, larger pores are formed to store the excess ILE.

Table 3.1 Summary of the structural properties of porous silica matrix which were obtained by removal of ILE from the nano-SCEs. BET surface area and porosity were determined from N_2 adsorption/desorption measurements. ILE/nano-SCE volumetric ratio was calculated from the density of ILE and nano-SCEs measured with pycnometer.

ILE/SiO_2 molar ratio	1.0	1.5		2.0
Drying method	SCD	Dried in ambient	SCD	SCD
BET Surface area (m^2/g silica)	1048	665	908	849
Pore volume (cm^3/g silica)	2.53	0.83	3.6	2.41
Silica density (g/cm^3)	2.1	2.3	2.3	2.3
Porosity (%)	84	67	89	85
ILE/nano-SCE volumetric ratio (%)	91.5	94.1		93.9

The PALS was obtained for the nano-SCEs with ILE/SiO_2 molar ratio of 1.0, 1.5, and 2.0 after ILE removal and CO_2 SCD. All the spectra resolved into four components by fitting using RESOLUTION.[100] The lifetime and intensity of each component is shown in Supplementary Information (Table 3.2). In porous materials, a part of the injected positrons form a positron-electron bound state, which is called positronium (Ps).[83,84] The Ps with the singlet spin state (anti-parallel) is called para-Ps (*p*-Ps), which annihilates with the emission of two quanta in a short lifetime of 0.125 ns (in vacuum). The Ps with triplet spin state (parallel) is called ortho-Ps (*o*-Ps), which emits three quanta during annihilation in vacuum.[85] As the intrinsic lifetime of *o*-Ps is 142 ns (thousand times longer than that of *p*-Ps), it diffuses nto the pores and survives for significantly longer. In condensed matter with small pore structures; however, a part of positron in *o*-Ps annihilates with the electrons with opposite spin at the pore surface and annihilates through the two quanta emission process with the lifetime of few tens of ns ("pick-

Table 3.2 Positron lifetime and intensity of the four components fitted in the positron lifetime spectrum of the porous silica matrix which was obtained by removal of ILE. ILE was extracted from the nano-SCE by soaking in ethanol for 36 h at 40 °C and subsequent drying by CO_2 super critical drying method.

	ILE/SiO_2						
	1.0		1.5		2.0		Annihilation type
	Lifetime (ns)	Intensity (%)	Lifetime (ns)	Intensity (%)	Lifetime (ns)	Intensity (%)	
1st	0.22	27.41	0.17	24.28	0.25	41.25	free positron, *p*-Ps
2nd	0.47	46.60	0.46	49.94	0.55	34.04	*o*-Ps (pick-off)
3rd	2.03	13.75	2.06	17.09	2.13	18.67	*o*-Ps (pick-off)
4th	61.78	12.24	65.75	8.69	66.00	6.04	*o*-Ps (pick-off)

off' process).[86] As this annihilation process is sensitive to small variations in the electron density, the small-sized pores in the samples can be characterized by analyzing the behavior of *o*-Ps annihilation.

Taking into account, that the porous silica (aerogel) samples are composed of silica and open spaces (pores), the first (shortest-lived) lifetime component, τ_1, with around 0.2 ns is attributed mainly to the annihilation of free-positron and the positron of *p*-Ps in the silica region. It is difficult to distinguish between the lifetime arising from the free positron and *p*-Ps due to limitation of the time resolution of the spectrometer. Since this component does not reflect the information of open spaces, it will not be discussed further in this paper. The second component, τ_2, with about 0.5 ns is due to the annihilation of *o*-Ps as it is longer than the intrinsic lifetime of *p*-Ps (0.125 ns). Annihilation with 0.4–0.5 ns has been observed in SiO_2 synthesized via the sol-gel process.[87,88] It is reported to be due to positron

annihilation without the formation of positronium in the vacancy clusters in amorphous SiO_2.[89,90] Thus, the second component is a result of the positron annihilation in the open-volume structure of the amorphous network of SiO_2. The third component, τ_3, with a mean lifetime of about 2.0 ns is a typical value observed in the porous silica made by sol-gel process.[91,94] It is originated from the pick-off annihilation of *o*-Ps trapped in the small pores between primary silica particles. The *o*-Ps lifetimes in the pick-off process can be used to evaluate the pore size using ETE model.[80,101] If the pore shape is assumed to be spherical, the pore diameter is calculated to be 0.63–0.65 nm for 2.0–2.1 ns (τ_3). The pore diameter of τ_2 and τ_3 is smaller than the molecular size of ILs;[103] thus, the pore corresponding to the second and third components don't contain ILE inside. However, they could contain adsorbed or ice-water and affect the determination of the exact number of ice-water monolayers at the ILE/ice-water/silica interface.[31] Additionally, these pores might be closed spaces, which do not connect with each other; thus, Li ion conduction would not occur through these spaces. Hence, τ_2 and τ_3 have negligible contribution towards the ionic conductivity. In contrast, the longest lifetime component, τ_4, with lifetime in the range of 60–65 ns is considered to be due to the annihilation of *o*-Ps in the larger size pores. The pore diameter is estimated to be about 4.6–5.1 nm, which can hold IL molecules. These small sized pores were not distinguished by SEM, TEM and N_2 adsorption/desorption analysis above. However, no components with lifetimes higher than 70 ns were observed from the PALS spectra. This implied that most of the injected positrons annihilated in the small sized pores (less than few tens nm) before getting trapped in the larger pores (> 10 nm). From these results, it is concluded that PALS technique is sensitive to a relatively small pore size in the

sample (less than few tens nm) and is in agreement with the other analytical techniques such as SEM, TEM, and N_2 adsorption/desorption methods.

The lifetime and intensity of the fourth component as a function of ILE/SiO_2 molar ratio is shown in Fig. 3.6. The lifetime increased with increasing molar ratio of ILE/SiO_2 even though the intensity decreased. This indicates that the pores of approximately 5 nm slightly grow in size with increasing ILE, while decreasing in number density. This trend corroborates with the reduction in BET surface area, even though it does not capture the larger pores. Thus, the nanoporous structure

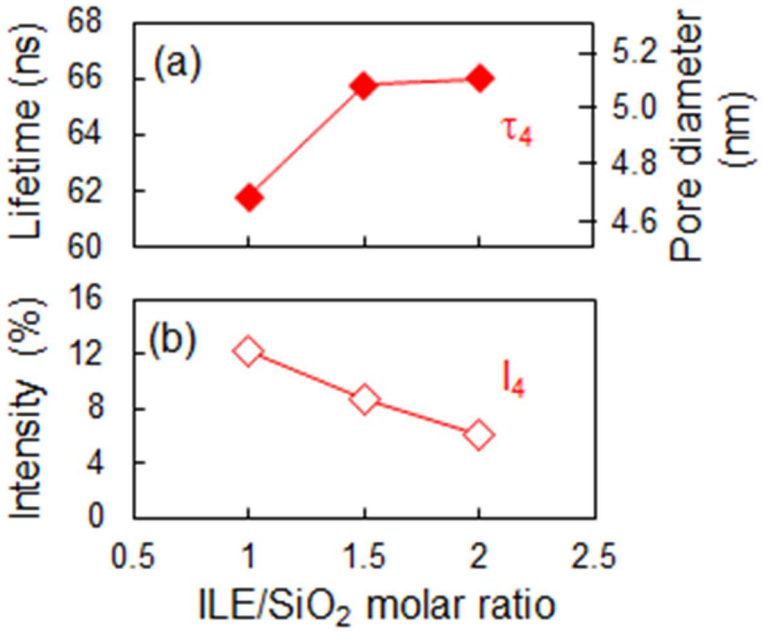

Fig. 3.6 Positron annihilation parameters for the fourth component of porous silica matrix which was obtained by soaking in ethanol for 36 h at 40 ºC and subsequent drying by CO_2 super critical drying method. (a) Lifetime and (b) Intensity as a function of ILE/SiO_2 molar ratio of the original nano-SCEs. The pore diameter was calculated and is shown in the right axis of (b). Reprinted with permission from ref.[102] Copyright 2021, American Chemical Society.

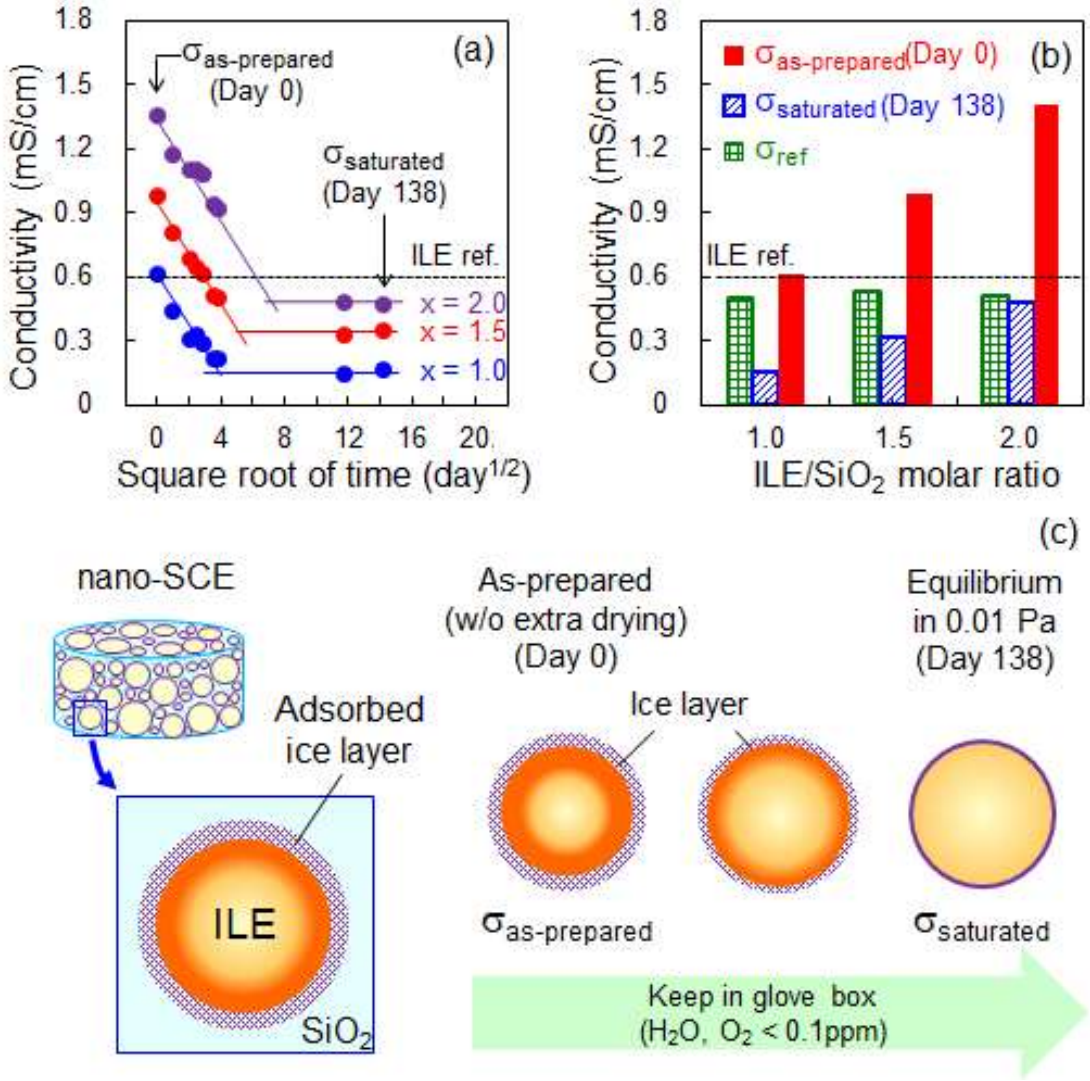

Fig. 3.7 Ionic conductivity of nano-SCEs with different ILE/SiO_2 molar ratio (x = 1.0, 1.5 and 2.0). (a) Conductivity vs. square root of drying time in Ar-filled glovebox. (O_2, H_2O <0.1 ppm). [31] (b) Ionic conductivity with drying in glovebox for 0 day ($s_{as\text{-}prepared}$) and 138 days ($s_{saturated}$). The reference conductivity which is estimated from porosity is shown for comparison. (c) Schematic of the pore structure change in nano-SCE. Reprinted with permission from ref.[102] Copyright 2021, American Chemical Society.

was completely characterized by the combined results from SEM, TEM, N_2 adsorption/desorption, and PALS.

In order to investigate the behavior of Li ion conduction in the nanoporous structure, the effect of drying on conductivity was studied. The nano-SCEs with x = 1.0, 1.5, and 2.0 were selected and are shown in Figure 3.7 (a). [31] The conductivity increased with increasing molar ratio of ILE/SiO_2, i.e., the volume of ILE. The plot of pure ILE reference is also shown for comparison (0.6 mS/cm, horizontal dotted line). Fig. 3.7 (a) shows the change in conductivity for 23 μl of nano-SCE as a function of residence time (square root of time) in the Ar-filled glovebox. For the samples immediately after vacuum drying (without additional drying in the glovebox, Day 0), the conductivity exceeded that of the ILE reference. This is due to the promotion of the Li-ion conductivity by the ordered IL molecules on the porous silica surface with a functional adsorbed ice-water layer. The strong hydrogen bonding between the ice-water and the IL molecules induces molecular ordering of the ionic liquid anions and cations on the silica surface. This interfacial interaction weakens the association between the Li- ion and its TFSI anion, thereby enhancing the ionic conductivity well beyond that of pure ILE.[31] Herein, the Ar atmosphere in the glove box contains less than 0.1 ppm of water, which corresponds to a relative humidity of 0.0005 %RH, a partial water pressure of 0.01 Pa or a dew point of -88 °C. The amount of ice-water on silica is in equilibrium with the partial pressure of water in the environment[36,37]. Thus, the nano-SCEs are slowly dried when they are kept in the glovebox until they reach an equilibrium with the dry glove box conditions. Fig. 3.7(a) indeed shows a decrease in the ionic conductivity of nano-SCEs until it saturates at a value well below that of the pure

ILE. The linear relationship of conductivity with the square root of drying time is due to the diffusion limited removal of the adsorbed water from the silica surface.

Both the conductivity with largest enhancement ($\sigma_{as\text{-}prepared}$: conductivity at Day 0 with functional ice water layer) and least enhancement ($\sigma_{saturated}$: conductivity at Day 138 with only a partial coverage with ice water) were extracted from Fig. 3.7 (a) and are summarized in Fig. 3.7 (b). It is noteworthy that the numbers for the $\sigma_{as\text{-}prepared}$ and $\sigma_{saturated}$ are derived from the same sample; i.e. with the same nanoporous structure. Thus, these value can be compared directly for estimating the surface enhancement and pore confinement degree. For comparison, a reference conductivity (σ_{ref}) was added, where the bulk ILE conductivity is corrected for the porosity, P, obtained by CO_2 SCD (Table 1) using eq. (3.4)

$$\sigma_{ref} = \sigma_{ILE} \times P \tag{3.4}$$

This reference is the value for a hypothetical case where the conductivity is simply proportional to the ILE/SiO_2 volumetric ratio without any surface enhancement and effects of a viscosity increase.

The ratio of $\sigma_{as\text{-}prepared}$ to σ_{ref} provides the enhancement in the ion conductivity with respect to the same volume of bulk ILE and increases with ILE/SiO_2 ratio. However, the $\sigma_{as\text{-}prepared}/\sigma_{ref}$ ratio includes all the conduction phenomena in the nanostructure, that is, the surface enhancement effect (surface functionalization) and pore confinement degree (increase in viscosity). To distinguish the effect of these phenomena, the equivalent ice-water and ILE layer thickness was determined by the water and ILE content with the surface area of silica matrix in Table 3.3. The vacuum-dried nano-SCE pellets were directly brought into the Ar-filled

Table 3.3 Equivalent thickness of ILE and adsorbed ice water layer derived by surface area assuming the flat silica surface. The water content was determined from the excess mass weight difference from non-volatile compounds.

ILE/SiO_2 molar ratio	1.0	1.5	2.0
Li-TFSI weight (g)	0.22	0.33	0.44
BMP-TFSI weight (g)	0.95	1.43	1.90
ILE volume (cm^3)	0.79	1.19	1.58
Theoretical weight of SiO_2 (g)	0.14	0.14	0.14
Theoretical weight of nano-SCE (g)	1.31	1.89	2.48
Water content (g)	0.10	0.14	0.24
Surface area of mesopores (m^2/g)	1048	908	849
Surface area of micropores (m^2/g)	400	360	350
Equivalent thickness of ILE layer (nm)	5.6	9.7	13.8
Equivalent number of adsorbed ice water layers (ML)	1.9	3.0	5.3

glovebox (O_2, H_2O <0.1 ppm) and stored in closed vials. Thus, the water content retained in the nano-SCE was determined from the difference between the measured weight of the pellets and the weight of the non-volatile compounds (ILE and SiO_2). As the BET surface area shown in Table 3.1 is for the mesopores and macropores only, surface area of micropores was also estimated from the silica volume and average particle diameter determined by TEM images in Fig. 3.4. A maximum additional surface area of micropores was determined to be between 350 and 400 m^2/g. The number of corresponding monolayers of surface-bound ice layers was estimated from the water content and total surface area of all kinds of pores. Meanwhile, the equivalent thickness of ILE was obtained by ILE volume fraction and BET surface area assuming a flat silica surface. The calculation detail

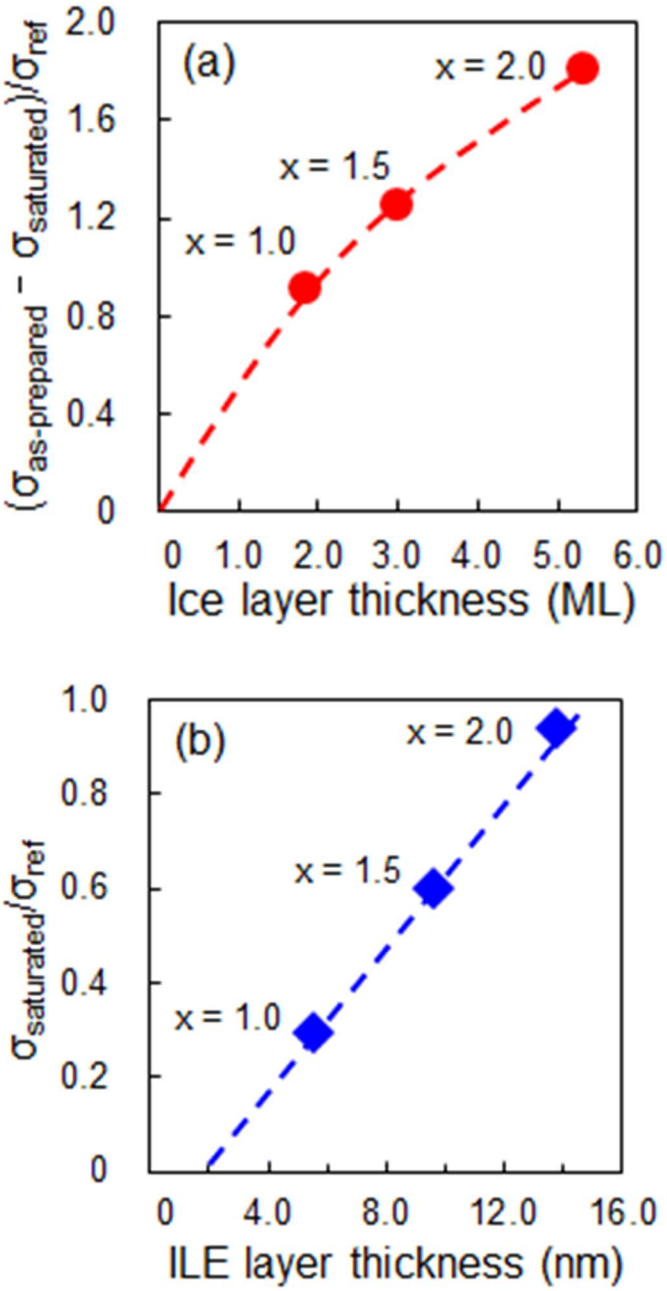

Fig. 3.8 Ion conduction behavior in the nano-SCEs. "x" denotes the ILE/SiO_2 molar ratio of the samples. (a) Surface enhancement factor ($(s_{as\text{-}prepared}\text{-}s_{saturated})/s_{ref}$) of nano-SCEs as a function of Ice water layer thickness on the silica surface. (b) Pore confinement degree ($s_{saturated}/s_{ref}$) of nano-SCEs as a function of equivalent ILE layer thickness assuming a flat silica surface. Reprinted with permission from ref.[102] Copyright 2021, American Chemical Society.

has been described previously[31]. All the data is summarized in Table 3.3.

Fig. 3.8(a) shows the enhancement factor, which is defined by ($\sigma_{as\text{-}prepared}$-$\sigma_{saturated}$)/ σ_{ref}, as a function of the number of ice-water layers. It is apparent that the enhancement effect is related to the number of ice water layers. The nano-SCE composition (water content) at t = 0 depends on the vacuum drying process, which indicates that the removal of water from the nano-SCE takes longer for a higher ILE/SiO_2 content. It is known that a silanol surface can have 3 to 4 solid ice water layers.[36] Thus, ideally, 3 to 4 monolayers of ice water are obtained to impart the largest surface enhancement effect without liquid water.[31] The enhancement factor is likely to be saturated from the range of 4–5 monolayers of the ice water layer (Fig. 3.8 (a)). For the nano-SCE with x = 2, the surface water layer right after vacuum drying may already have some liquid-like surface water as up to 5 layers partial pressure of water in the glove box (0.01 Pa), the amount of surface water is reduced from 2-5 monolayers at the start to only a partial monolayer of adsorbed water.[31] Without this surface ice-water, the surface conduction promotion effect is small and the decrease in Li-ion were estimated. Thus, the thickness of the ice water layer should be controlled within 3 to 4 monolayers. However, it is difficult to make a thin and uniform adsorbed water layer on the silica pore walls as it is relatively sensitive to the environment (humidity). The other functional layers that yield similar or even larger surface promotion are expected to be developed.

As the samples continue to dry in the glovebox, the surface water layer further shrinks. At the equilibrium condition (saturation), a conductivity is dropped due to the increasing viscosity of the ILE encapsulated in the nanopores.[30,104] Thus, the conductivity saturates well below the value of the pure ILE. Fig. 3.8 (b) shows the pore confinement degree, which was defined by $\sigma_{saturated}/\sigma_{ref}$, as a function of equivalent ILE layer thickness. As seen in the figure, the $\sigma_{saturated}/\sigma_{ref}$ ratio is

proportional to the ILE thickness, that is, pore size of the silica matrix. The $\sigma_{saturated}/\sigma_{ref}$ ratio dropped with decreasing pore size indicating that a strong confinement occurred in the samples with the smaller pores in nano-SCE. Furthermore, the ILE layer thickness where conductivity becomes zero is estimated to be approximately about 1.9 nm or 1-2 ILE monolayers from extrapolating the plots. This might correspond to the thickness of the adsorbed ILE layer on the silica pore wall. In contrast, the $\sigma_{saturated}/\sigma_{ref}$ ratio increases with the ILE layer thickness, implying that the confinement effect was relieved in the large-sized pores. Furthermore, the $\sigma_{saturated}/\sigma_{ref}$ ratio reaches 1 at the ILE thickness of 15 nm indicating that the pore confinement effect reached zero at some point. Assuming the pore size as approximately double that of the ILE thickness, the optimal pore size where the confinement effect was sufficiently suppressed can be estimated to be approximately 30 nm. This agrees well with the pore size of the samples with a higher conductivity (x = 2.0) in Fig. 3.5 The overall (measured) conductivity of nano-SCE was determined by the balance of surface enhancement and pore confinement effects. Thus, the low conductivity of the sample with x=1.0 is explained by the stronger confinement in the pores compared to the surface enhancement effect. The total conductivity was limited to 0.6 mS/cm even in Day 0, which is almost the same as pure ILE value (0.6 mS/cm) and 0.15 mS/cm at the equilibrium condition on Day 138. This is due to the suppression of the ionic conduction by the severe confinement in the pores. In contrast, the higher conductivity was obtained in the sample with x = 2.0 (1.4 mS/cm in Day 0 and 0.5 mS/cm in Day 138). This is due to the large surface enhancement effect with approximately five monolayers of ice water layer before drying, and the limited pore confinement effect in the large pores of 30–40 nm even at equilibrium

conditions. As such, the Li ion conduction behavior in nano-SCE with different ILE/SiO_2 ratio was interpreted with two phenomena that originated from the nanostructure; surface enhancement effect and pore confinement effect.

Finally, the effect of the pore structure on the Li ion conduction behavior was investigated by comparing the pore structures obtained from the various characterization techniques and surface enhancement/pore confinement effect. The variation in the surface area corresponds to the size of pores in the sample. Both, the size of the macropores (> 50 nm), which is characterized by SEM measurement (Fig. 3.3), and that of the mesopores (2–50 nm), which is determined by N_2 adsorption/desorption (Fig. 3.5) and PALS analysis (Fig. 3.6), were increased with increasing ILE/SiO_2 molar ratio. The reason for the larger surface area in the sample with lower ILE/SiO_2 ratio was the reduction of the pore size in the samples. Furthermore, the number of mesopores was larger in the samples with lower ILE/SiO_2 ratio. This also leads to a larger surface area of the sample. However, the structure which has many small pores (less than few tens of nm) lead to suppression of the conductivity due to the pore confinement effect as discussed in Fig. 3.8 (b). Thus, to attain a higher conductivity by maximizing surface conduction promotion effect and minimizing the confinement effect, a pore structure with optimized pore size (approximately 30 nm) should be realized in the nano-SCE.

3.4 Conclusion

I have investigated the effect of the pore structures on the Li ion conduction behavior in nano-SCE, which is composed of ionic liquid and Li-salt (ILE) supported by porous silica matrix. The porous silica matrix was successfully

obtained by extracting the ILE from the nano-SCE. A careful drying above CO_2 super critical point aids in sustaining the original structure, thereby avoiding the collapse due to surface tension. Pore size and its distribution, BET surface area, and porosity were characterized by several analytical techniques such as SEM, TEM, N_2 adsorption/desorption, and PALS methods. It was revealed that there are various size of macropores and mesopores in the silica matrix, and their size increased with increasing ILE/SiO_2 molar ratio of original nano-SCEs. It was also revealed that the surface area was larger corresponding to the reduction in the pore size. The surface enhancement degree was verified to increase with the thickness of the adsorbed ice-water layer on the silica surface, indicating that the conduction promotion effect originated from the strong hydrogen bonding in the ice layer. In addition, a large number of small pores lead to a severe pore confinement effect that results in a drop in the conductivity due to the increasing viscosity of ILE filled in the pores. The conductivity can be higher by realizing a nano-SCE with an optimized pore size of approximately 30 nm to minimize the pore confinement effect.

Chapter 4

High-rate Performance Solid-State Lithium Batteries with Silica-gel Solid Nanocomposite Electrolytes using Bis(fluorosulfonyl)imide-based Ionic Liquid

4.1 Introduction

All-solid-state batteries (ASSBs) with solid electrolytes (SEs) are epoch-making energy storage devices beyond conventional lithium-ion batteries because SEs can remove the risks of electrolyte leakage, volatilization, flammability and explosion. To realize high-energy and high-power performance as well as high-safety, SEs with fast lithium-ion conduction and good interfacial contact with the electrodes are expected to be developed. Recently, Xubin et al. developed a novel solid nanocomposite electrolyte (nano-SCE) composed of ionic liquid (IL), Li-salt and porous silica using sol-gel method[31]. This electrolyte ensures battery safety because of the non-volatility, thermal and electrochemical stability. Furthermore, a liquid precursor can be impregnated into the powder electrodes, which potentially forms a good interfacial contact between the electrode and the electrolyte. More interestingly, nano-SCE shows the promotion of the Li-ion conductivity on the silica pore wall. The strong hydrogen bonding between the surface ice-water and the IL molecules induces molecular ordering of IL anions and cations. This interfacial interaction weakens the association between the Li-ion and its anion, thereby enhancing the ionic conductivity well beyond that of pure IL electrolyte.

As the ice-water layer was confirmed to be electrochemically inactive, it does not cause degradation during cycling of the batteries. Furthermore, damage to the active electrode materials is avoided as this water-based sol-gel precursor does not contain corrosive acidic compounds, such as formic acid (FA), which have been typically proposed as catalysts in the literature.

Previously, Xubin et al. reported on the battery performance of Li-LFP ($LiFePO_4$) and Li-$Li_4Ti_5O_{12}$ (Li-LTO) cells using nano-SCE containing 1-butyl-1-methylpyrrolidinium bis(trifluoromethylsulfonyl)imide (BMP-TFSI) as IL, which demonstrated stable charging and discharging behaviour.[31] However, the C-rate performance of these cells was limited as a result of the formation of a highly resistive solid electrolyte interphase (SEI) against metallic lithium and the limited ion conductivity of the BMP-TFSI based nano-SCE.[31,105,106] In this paper, I demonstrate the drastic improvement of the C-rate performance of a solid-state Li-ion battery using a nano-SCE with 1-ethyl-3-methylimidazolium bis(fluorosulfonyl)imide (EMI-FSI). The bis(fluorosulfonyl)imide (FSI^-) anion is a smaller analogue of $TFSI^-$, where both CF_3 end groups of $TFSI^-$ are substituted by F^- atoms. FSI^--based ILs are known to reduce the resistance of SEI.[107–110] Additionally, the conductivity of FSI^--based ILEs is higher than those of $TFSI^-$ based ones as FSI^- has a lower viscosity.[111] The reaction kinetics at the Li/SCE are compared between the EMI-FSI^- and BMP-$TFSI^-$ based nano-SCEs using three-electrode measurements. The C-rate performance of the solid Li-LFP cell with nano-SCE is compared with that of a standard cell with a conventional lithium hexafluorophosphate ($LiPF_6$) liquid electrolyte.

4.2 Experimental

4.2.1 Synthesis of nano-SCE pellets

The nano-SCE monolith was prepared using a templated sol-gel process: the mesoporous silica matrix was formed by the slow hydrolysis-condensation reaction of tetraethyl orthosilicate (TEOS) with an ILE as template for the condensation of the interconnected hydrated silica network. Two different ILEs, which were composed of a Li-salt and an ionic liquid with a molar ratio of 1 : 3, were selected. One was a mixture of lithium bis(trifluoromethylsulfonyl)imide (Li-TFSI, 0.33 g, 99%, Solvay) and BMP-TFSI (1.02 mL, 99.9%, Solvionic), and the other was a mixture of Li-FSI (0.21 g, 99%, Fluorochem) and EMI-FSI (0.70 mL, 99.9%, Solvionic). The ILE, tetraethyl orthosilicate (TEOS, 0.5 mL, 98%, Sigma Aldrich), deionized water (DIW, 0.5 mL) and 1-methoxy-2-propanol (PGME, 1.0 mL, 99.5%, Merck) were mixed in a glass vial. The molar ratio of the ILE to TEOS was fixed at 1.5. The mixtures were stored in closed vials to form gels at 25 °C and 50% relative humidity in a climate chamber. After gelation for a few days, the open vials were first dried at 40 °C for 4 days at slightly reduced pressure (80 kPa) and then moved into a vacuum oven for 72 hours at 25 °C ($<5 \times 10^{-2}$ mbar). The result was a monolithic pellet with a diameter of approximately 1.5 cm and a thickness of 5 mm. The pellets were stored in a closed vial inside an Ar-filled glove box (oxygen <0.1 ppm, water <0.1 ppm).

4.2.2 Fabrication of the electrode foil

A LFP powder electrode was prepared by blade-coating on aluminum foil (20 μm) from an aqueous slurry containing a dry mass of 91 wt.% LFP, 3 wt.% carbon black (CB), 2 wt.% carboxymethylcellulose (CMC) and 4 wt.% fluorinated acrylic latex. First, the

LFP powder and carbon black (Imerys, SUPER C65) were mixed with the aqueous CMC solution (Nippon Paper, MAC350HC) using a planetary mixer. Then this homogenized product was mixed with DIW and a fluorinated acrylic latex (JSR, TRD202A) in a vacuum mixer to make a slurry for the coating. The prepared slurry was cast on aluminum foils to deposit the electrode films using a blade coater (Elcometer, 4340) with a blade height of 150 μm and coating speed of 15 mm sec^{-1}. These as-coated electrodes were immediately brought into an atmospheric oven with stagnant air at 70 °C for 10 min, and were further dried at 140 °C for 4 hours in a vacuum oven. The dry coating thickness was around 30 μm, as determined from scanning electron microscopy (SEM, Philips XL30) measurements. LTO powder electrode films were blade-coated on copper foils (25 μm) in a similar way as the LFP electrode. The composition of dry mass was 85 wt.% LTO powder, 5 wt.% CB, 5 wt.% CMC and 5 wt.% fluorinated acrylic latex. The LTO film thickness was approximately 40 μm.

4.2.3 Fabrication of the battery cells

Nano-SCE-impregnated electrodes were fabricated by drop-casting of the sol-gel precursor solution in the LFP and LTO electrode coatings and left to gel and cured in a similar way as for the fabrication of the nano-SCE pellets. First, 100 μL of precursor solution that had been aged for 2 days was drop-casted on the LFP and LTO electrode punched with a diameter of 15 mm. The electrodes were left for 4 or 5 extra days at 25 °C to form a gel. Then, the composite electrodes were dried at 40 °C for 4 days at 80 kPa, and kept in a vacuum oven for 72 hours at 25 °C ($<5 \times 10^{-2}$ mbar). The overburden thickness of the fully cured and dried nano-SCE on top of the impregnated composite powder electrode was 300–400 μm, as determined by SEM.

A Li-LFP cell with nano-SCE was assembled in a coin cell (MTI, CR2032) in an Ar-filled glove box. A lithium foil (0.75 mm, 99.9%, Sigma Aldrich) was pressed on the nano-SCE impregnated solid composite electrode, and the coin-cell was sealed. Similarly, a LFP-LTO cell was assembled by placing the nano-SCE impregnated solid composite LFP and solid composite LTO electrode foils facing each other. No separator was used in the solid-state cells. For comparison, a reference cell with LFP and LTO was made with a conventional organic liquid electrolyte solution, that is, 1 M $LiPF_6$ in ethylene carbonate (EC) : dimethyl carbonate (DMC) (1:1 vol.%) (99.9%, Solvionic). The powder electrodes, separator (Celgard, 3501) and Li foil were stacked and sealed in the coin cell.

4.2.4 Conductivity measurement of nano-SCE

The ion conductivity of the nano-SCE pellets was determined by electrochemical impedance spectroscopy (EIS) measurements on a small volume (23 μL) taken from the synthesized pellets and placed in a polytetrafluoroethylene (PTFE) ring. The filled ring was sandwiched between two stainless steel (SS) disks and sealed in a coin cell. All these preparations were done in an Ar-filled glovebox (O_2, H_2O < 0.1 ppm). The temperature of the coin cell was controlled by placing it on a metal chuck flushed with ethylene glycol from a circulating thermostatic bath (F12-ED, Julabo). The cells were first cooled to −10 °C, and then step-wisely heated to 50 °C. For impedance measurement, the AC amplitude was set at 10 mV and the frequency range was from 1 MHz to 1 Hz. The ionic resistance of the nano-SCE was determined from the high frequency intercept with the real axis in the Nyquist plots and the dimension of the inner ring filled with nano-SCE. The conductivity measurements were conducted with a Autolab PGSTAT302N potentiostat combined with a FRA32M frequency response analyzer (Metrohm)

controlled through Nova software.

4.2.5 Pulsed field gradient nuclear magnetic resonance spectroscopy (PFG-NMR)

PFG-NMR measurements were performed using a JEOL JNM-ECX400. The stimulated echo pulse sequence was used for the diffusion measurements. The normalized echo signal attenuation, *E*, was described by Eq. (4.1).[112]

$$E = \exp\left(-\gamma^2 g^2 \delta^2 D(\Delta - \delta/3)\right) \quad (4.1)$$

where g is the strength of the gradient pulse, δ is the duration of the gradient pulse, Δ is the interval between the leading edges of the gradient pulses, γ is the magnetogyric ratio and D is the self-diffusion coefficient of the molecules. The self-diffusion coefficients were estimated by fitting the echo signals which were obtained by changing Δ in Eq. (1). ^{7}Li was selected to determine the diffusion coefficient of the lithium ion. All the measurements were performed at 30 °C.

4.2.6 Three-electrode measurements of nano-SCE and ILE

For current-potential characterization of the individual lithium/nano-SCE interface, a solid-state three-electrode electrochemical measurement setup was constructed in an Ar-filled glove box. A nano SCE pellet (thickness of 5 mm and diameter of 1.5 cm) was placed on a large Li-ribbon supported on a copper plate as the counter electrode (largest area of 1.8 cm^2) and two Li-disks (diameters of 5 mm) were pressed on top of the SCE

pellet as working and reference electrodes (0.2 cm^2). The area of the counter electrode was approximately 9 times larger than that of the working electrode (WE) so that the measured current was determined by the electrode kinetics of the WE only. Cyclic voltammetry (CV) measurements were performed with a scan rate of 20 mV sec^{-1}. Additionally, pure ILE references were measured under similar conditions using a three-electrode electrochemical cell with a large Li counter electrode. The CV measurements were conducted with a Autolab PGSTAT302N potentiostat controlled through Nova software.

4.2.7 Electrochemical stability of nano-SCE

The electrochemical window of the nano-SCE was measured on a Li/nano-SCE/SS stack. A small volume (23 μL) of nano-SCE was placed in a PTFE ring, and sandwiched between Li foil and SS disks in an Ar-filled glovebox (O_2, H_2O < 0.1 ppm). The cyclic voltammograms were recorded at a scan rate of 10 mV sec^{-1} from the open circuit potential (OCP) to −0.5 V and +4.5 V. The CV measurements were performed using a potentiostat (Solartron Celltest 1470E).

4.2.8 Li stripping and plating test in a Li/nano-SCE/Li symmetric cell

Li stripping and the plating test were performed with a Li/nano-SCE/Li stack. A small volume (23 μL) of nano-SCE was placed in a PTFE ring, and sandwiched between two Li foils and sealed in a coin cell. A constant current of +/− 0.1 mA cm^{-2} was applied for one hour alternately. The measurements were conducted using a potentiostat

(Solartron Celltest 1470E) at room temperature in an Ar-filled glovebox.

4.2.9 Electrochemical measurement of the battery cells

In a typical experiment, three cyclic voltammograms were recorded at a scan rate of 1 mV sec^{-1} before and after the charge-discharge cycles. The potential ranges were between 2.7 V and 4.2 V for the Li-LFP cell, and 1.2 V to 2.4 V for the LTO-LFP cell. The galvanostatic charge-discharge measurements were performed at a C-rate of 0.1C, 0.2C, 0.5C and 1.0C. The charge and discharge cycles were performed at the same C-rate. Note that no constant voltage step was used in these experiments. The current density of 1C was 0.15 mA cm^{-2}. All the electrochemical measurements of the two-terminal battery cells were conducted using a potentiostat (Solartron Celltest 1470E) at 30 °C.

4.3 Results and discussion

Figure 4.1 shows the temperature dependence of the ionic conductivity of the nano-SCE with BMP-TFSI + Li-TFSI (hereinafter referred to as BMP-TFSI nano-SCE) and EMI-FSI + Li-FSI (hereinafter referred to as EMI-FSI nano-SCE). The ion conductivity of the EMI-FSI nano-SCE was higher than that of BMP-TFSI nano-SCE as expected from the difference in viscosity and ion conductivity of the pure ionic liquids.[111] The conductivity at 25 °C was 0.8 mS cm^{-1} for BMP-TFSI nano-SCE and 6.2 mS cm^{-1} for EMI-FSI nano-SCE. For comparison, the conductivity at 25 °C was 0.6 mS cm^{-1} and 8.8 mS cm^{-1} for their respective ILEs. Note that the BMP-TFSI nano-SCE showed a slight enhancement compared with ILE owing to the large interfacial conduction enhancement,

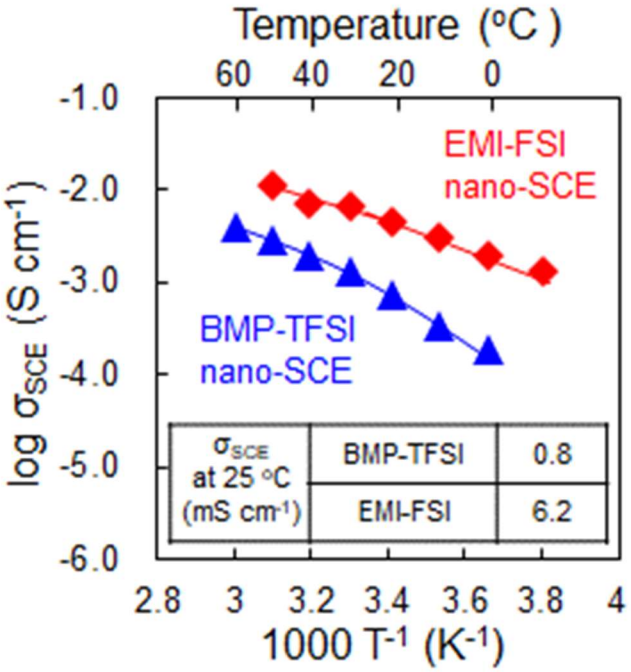

Fig. 4.1 Temperature dependence of the ion conductivity of nano-SCEs with BMP-TFSI + Li-TFSI (blue) and EMI-FSI + Li-FSI (red). Reprinted with permission from ref [113] Copyright 2020, IOP Science.

which overcompensated the decrease in conductivity arising from the strongly increased viscosity of the ILE encapsulated in the pores. However, the conductivity of EMI-FSI nano-SCE was slightly lower than that of ILE itself, which indicated a relatively smaller interface enhancement and/or larger increase in viscosity inside the pores. In Fig.4.1, a continuous and nearly linear variation in ion conductivity, σ, with inverse temperature was observed, which is typical for a nano-SCE.[31] The slope of the $\sigma - T^{-1}$ profile was smaller in the EMI-FSI nano-SCE than in the BMP-TFSI nano-SCE, which indicated a lower activation energy of Li-ion diffusion owing to the lower viscosity of EMI-FSI and the higher dissociation degree of the Li cation from the FSI anion.[114–117] Indeed, it

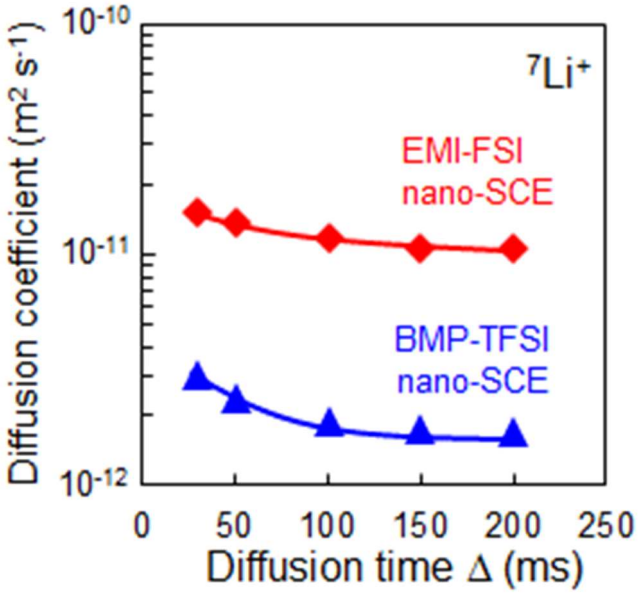

Fig. 4.2 Pulsed field gradient NMR derived Li^+ diffusion coefficient of nano-SCEs with BMP-TFSI + Li-TFSI (blue) and EMI-FSI + Li-FSI (red) as a function of the interval between the gradient magnetic field pulses. Reprinted with permission from ref [113] Copyright 2020, IOP Science.

has been shown that the Li cation is solvated by three FSI^- anions and the bond length of Li^+-O^- (of the FSI anions) is relatively longer than that of other Li-salts (e.g., Li-TFSI).[117]

From the PFG-NMR measurement, the self-diffusion coefficients of the different mobile Li-ion species in the nano-SCEs were determined as a function of the interval time between the gradient magnetic field pulses Δ. The $^7Li^+$ self-diffusion coefficients of BMP-TFSI nano-SCE and EMI-FSI nano-SCE are shown in Fig. 4.2. The diffusion coefficient of EMI-FSI nano-SCE was approximately 6 times higher than that of BMP-TFSI. This value matched well with the ratio of conductivity shown in Fig. 4.1. The Li^+ self-diffusion coefficient decreased with Δ and became saturated at higher Δ for both BMP-TFSI and

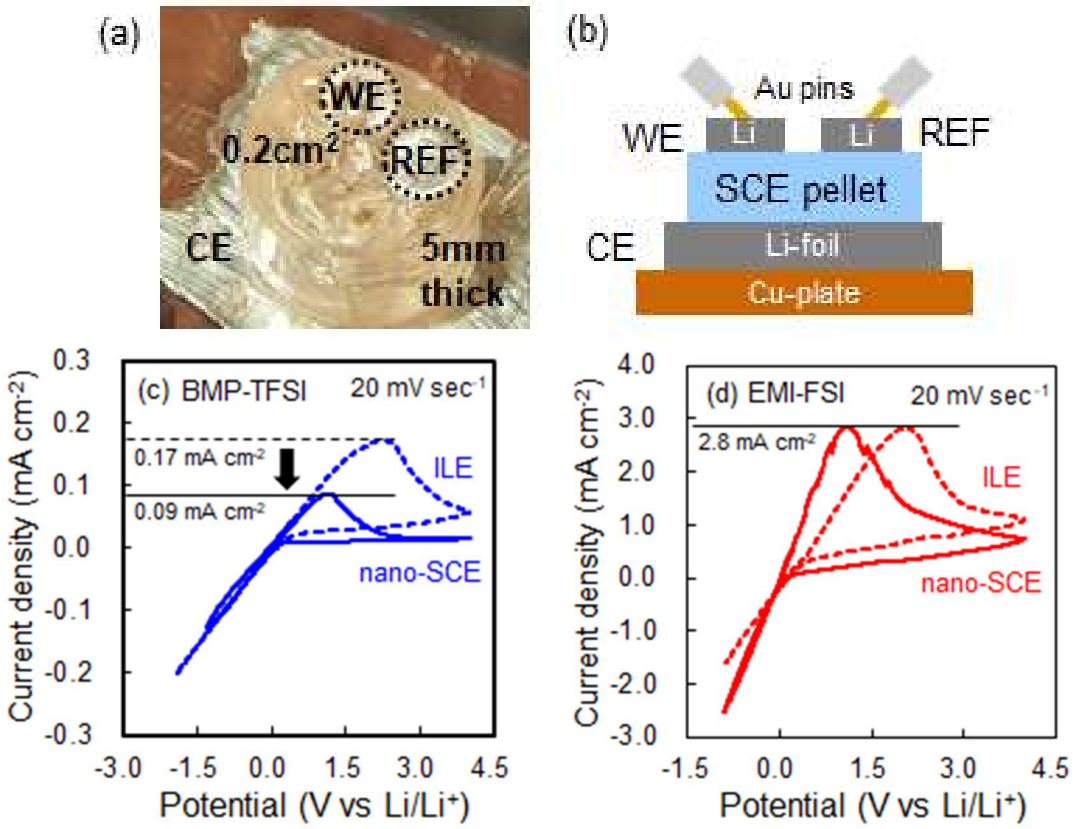

Fig. 4.3 Three-electrode electrochemical measurements of nano-SCEs and ILEs. (a) Picture of the three-electrode measurement set up with SCE pellet. (b) Schematic showing the cross sectional view of the electrical contact of the set up. (c) Cyclic voltammograms of nano-SCE with BMP-Li-TFSI (solid line) and ILE reference (dotted line) measured by three-electrode measurement set up. (d) Cyclic voltammograms of nano-SCE with EMI-Li-FSI (solid line) and ILE reference (dotted line) measured by three-electrode measurement set up. Reprinted with permission from ref [113] Copyright 2020, IOP Science.

EMI-FSI nano-SCEs, which indicated that slow moving species became dominant in the long pulse intervals. As the saturation value was less than that of pure ILE, these slow Li-species corresponded to the decrease in conductivity arising from the confinement of the ILE in the mesopores of nano-SCE, which has a higher viscosity owing to the restriction

of molecular movement.[30,31] In contrast, the self-diffusion coefficient was higher at small Δ, which indicated the presence of a fast moving Li-species that responded only at short intervals between magnetic field pulses. The gradient of the self-diffusion coefficient suggested that the activation energy of diffusion was lowered at the silica pore surface. This implied that the Li^+ diffusion was enhanced at the silica surface according to the conductivity enhancement mechanism described in our previous study.[31] The increase in the self-diffusion coefficient or, thus, the enhancement at the silica surface was indeed larger for the BMP-TFSI nano-SCE than for the EMI-FSI nano-SCE. However, the presence of a gradient in the EMI-FSI nano-SCE implied that an interface enhancement was still present even though the total conductivity was slightly lower owing to the increased viscosity in the core of the mesopore, as stated above.

The electrochemical stability of the nano-SCE against lithium metal was tested using a three-electrode setup. A schematic of the setup is shown in Fig. 4.3 (a) and (b). The current-potential characteristics of Li/ILE/Li and Li/nano-SCE/Li are shown in Fig. 4.3 (c) and (d), respectively. Reversible lithium plating and stripping was observed in all the measurements. For the BMP-TFSI ILE, a stable SEI layer was formed at the metallic lithium which caused the large IR drop in the *i-V* curve on both the cathodic and anodic sides. The cathodic current in the pure ILE solutions did not show any hysteresis down to -0.2 mA cm^{-2}. However, the anodic dissolution showed a passivation peak with a maximum peak current of 0.17 mA cm^{-2} and a steady-state current of only 0.06 mA cm^{-2} (measured at 4.0 V in Fig. 4.3 (c)) in the fully inhibited current regime. Whereas the physical SEI layer limits both the currents in the cathodic and anodic regimes, an additional passivation layer is formed only for lithium dissolution.[105,106] As the *i-V* curves were reproducible over many cycles in the ILE solutions, we believed the inhibition layer was a soluble near-surface layer that disappeared upon switching polarity.

Indeed, whereas the extraction of Li^+ from the Li-TFSI solution merely builds up a depletion layer in the cathodic regime, the introduction of additional Li^+ in the ILE solution needs a solvation action by the IL molecules, which quickly reaches saturation. Additionally, an increased salt concentration in ionic liquids leads to a strong increase in ILE viscosity and even solidification.[118] Note that in a symmetric two-electrode setup with equal size of Li cathode and anode, only the passivation peak is seen as the anode will be always rate limiting. Similar to ILE, the cathodic current branch of SCE, that is, the solid-solid interface, showed no hysteresis for cathodic currents up to −0.15 mA cm^{-2} with the similar SEI resistance of ILE. However, the anodic peak of Li/nano-SCE was lower at 0.09 mA cm^{-2}, which is half of ILE, and the steady state current in the anodic passive region became 0.015 mA cm^{-2} (measured at 4.0 V), that is, only a quarter of that in the pure ILE solution. The ILE in the nano-SCE is already more viscous in the mesopores and inhibition by saturation will hence be reached quicker at the interface of lithium and the pores of the nano-SCE. Both the voltammograms for the Li/ILE/Li and Li/SCE/Li electrodes were reproducible upon multiple cycles, which indicated that the anodic passivation layer and chemical SEI layer were stable. The slow dissolution kinetics at the Li/SCE interface severely limited the performance of the half cells made with Li metal anodes. In contrast, the resistance of the stable SEI layer in the EMI-FSI ILE was much less than that of BMP-TFSI + Li-TFSI. The anodic dissolution peak current increased to 2.8 mA cm^{-2}, and the steady state current for anodic passivation was 1.1 mA cm^{-2} (measured at 4.0 V in Fig. 4.3 (d)). The higher currents for EMI-FSI versus the BMP-TFSI ILE showed that both the cathodic (SEI limited) and anodic (SEI and passivation layer limited) reaction kinetics at the Li/SCE interface were faster, at least in part as a result of the smaller resistance of the SEI and passivation layers.[109,110] For the nano-SCE, the resistance of the stable SEI layer was almost the same as that of ILE

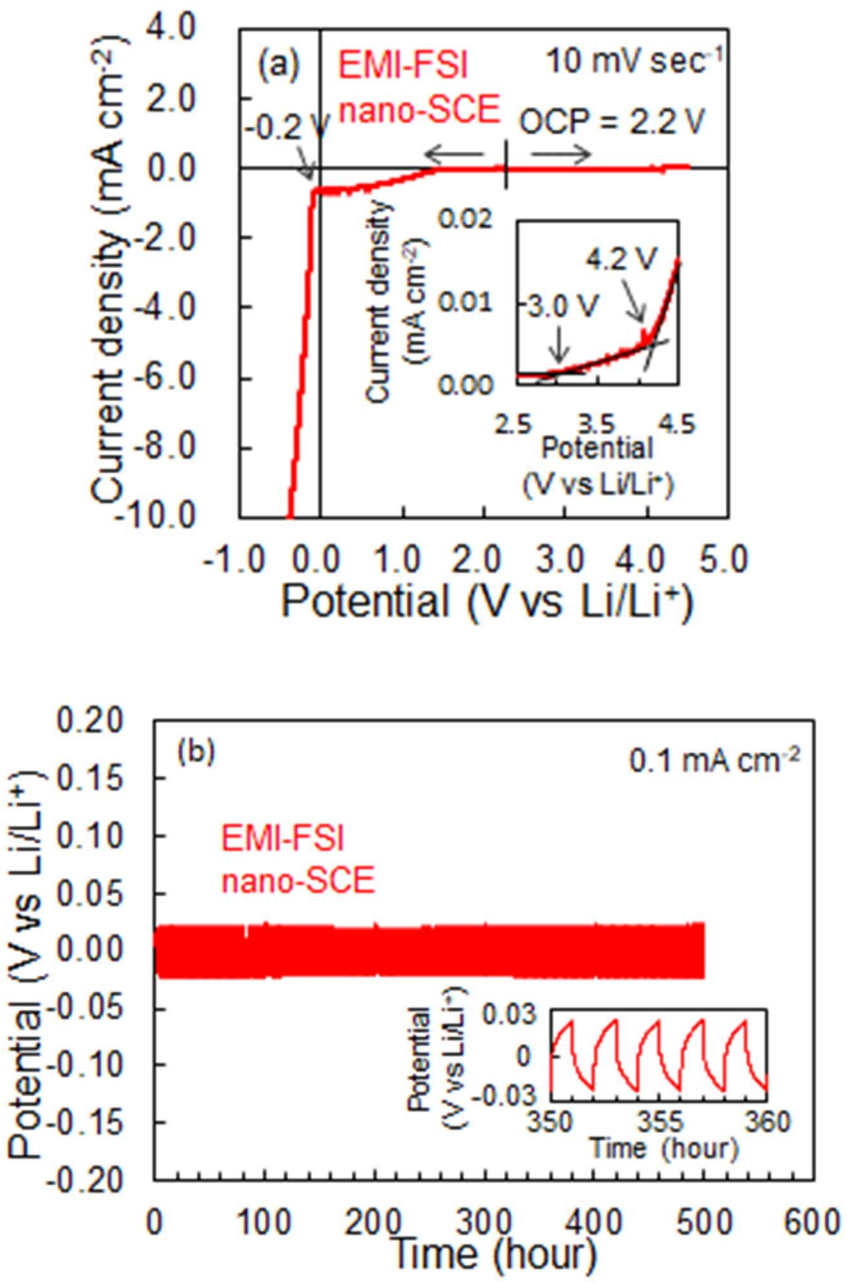

Fig. 4.4 Electrochemical stability of nano-SCEs. (a) Linear sweep voltammograms of EMI-FSI nano-SCE at stainless steel (SS) using a two-electrode SS/nano-SCE/Li stack structure with a scan rate of 10 mV s^{-1}. (b) Cycling stability of the Li/nano-SCE/Li symmetric cell with EMI-FSI nano-SCE at a current density of 0.1 mA cm^{-2}. Reprinted with permission from ref [113] Copyright 2020, IOP Science.

and the anodic peak current reached 2.8 mA cm^{-2}; which was very similar to that of the ILE solution. The steady-state anodic passivation current was somewhat lower for nano-SCE than for the ILE solution but was still high with a value of 0.7 mA cm^{-2}. Indeed, the lower viscosity in the pores lowered the saturation value somewhat but overall, the

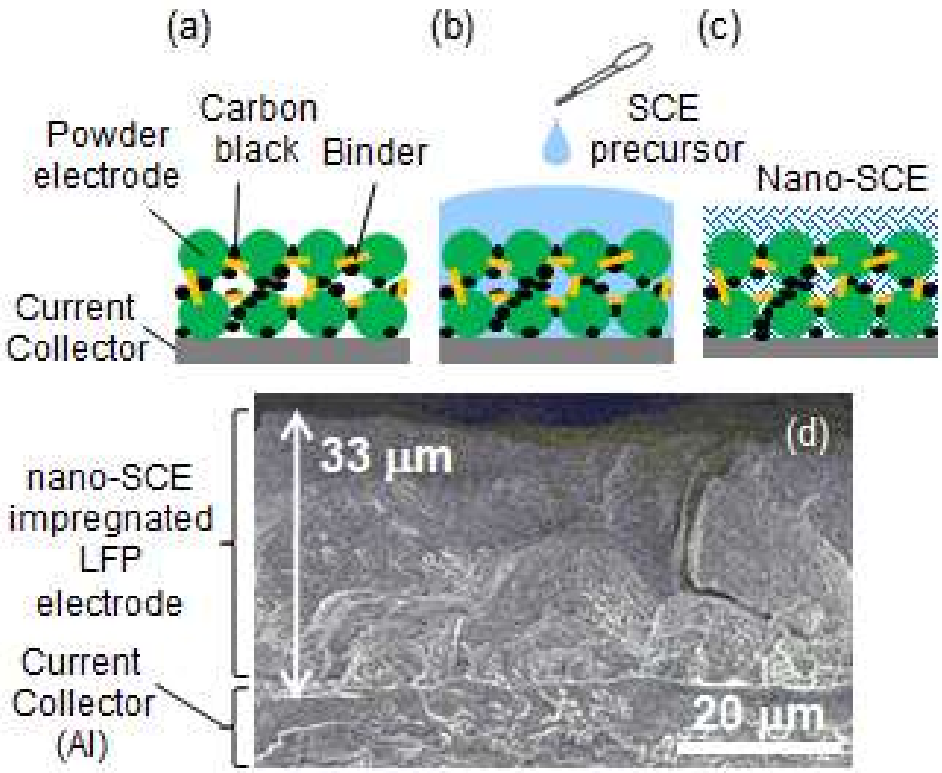

Fig. 4.5 Schematic of the composite electrode fabrication process with sample pictures and images. (a) LFP powder electrode foils. (b) Drop casting of the SCE sol-gel precursor. Liquid sol-gel precursor penetrates into the powder electrode and fills the space between active mass and gels in place. (c) Gelation 6 days after drop casting. The nano-SCE forms around the active mass and the composite electrode densifies during drying curing of the gel into the nano-SCE. (d) Cross-sectional SEM images of composite electrode. Reprinted with permission from ref [113] Copyright 2020, IOP Science.

dissolution kinetics at the Li and EMI-FSI nano-SCE interface were still approximately 50 times higher than those of BMP-TFSI nano-SCE.

To check the electrochemical stability of the EMI-FSI nano-SCE, linear sweep voltammograms were recorded at a scan rate of 10 mV sec^{-1} with a SS/SCE/Li stack, and are shown in Fig. 4.4 (a). The OCP was around 2.2 V versus Li^+/Li. First, the voltage was swept to a negative potential of −0.5 V. The water reduction peak (expected above 1 V) was not observed, which confirmed that the ice-water layer, which was created at the IL/SiO_2 interface, was stable. Before the onset of lithium plating at V < 0 V versus Li^+/Li, a current plateau of approximately 0.5 mA cm^{-2} was measured at V< 1.5 V versus Li^+/Li for the decomposition of the IL. The decomposition of the electrolyte was controlled by the introduction of a stable SEI as it is done also for conventional carbonate electrolytes (e.g., $LiPF_6$ in EC:DEC). Hence, the nano-SCE may be used for an anode such as graphite,[119,120] Si[121] as well as metal Li. The formation of stable SEI at Li metal was already discussed with regards to Fig. 4.3. Below, the cycling stability of the nano-SCE against Li metal in a symmetric cell will be shown (See Fig. 4.4 (b)). When increasing the potential from OCP to more positive potentials, a small current started to flow at 3.0 V (vs Li^+/Li) with an even steeper increase at 4.2 V (vs Li^+/Li) but the current density remained well below 0.02 mA cm^{-2} up to 4.5 V. The electrochemical window of the nano-SCE was determined by that of the ILE.[115] For a voltage window up to 4.5 V, $LiFePO_4$,[108,122] $LiCoO_2$[123] and $LiMn_{1/3}Co_{1/3}Ni_{1/3}O_2$[124] can be used as the cathode.

To assess the cycling stability of EMI-FSI nano-SCE against Li metal, sequential Li stripping/plating experiments were performed using a Li/nano-SCE/Li symmetric cell. As shown in Fig. 4.4 (b), a steady-state voltage hysteresis of approximately 50 mV was observed at a current density of 0.1 mA cm^{-2} without voltage reduction from the first few

cycles. This indicated that a stable SEI was formed at the Li/nano-SCE interface as discussed above. After long-term cycling for over 500 h, no sign of an internal short circuit was observed, which indicated a uniform and reversible Li deposition with a stable Li/nano-SCE interface layer. Hence, the results showed that the nano-SCE shows potential for use in Li-metal batteries with high safety, high interfacial stability and long-term cycling stability.

Next functional cells with LFP powder electrodes were assembled. Figure 4.5 (a)–(c) shows a schematic of the composite electrode fabrication process. The sol-gel solution was prepared and kept for two days to allow for the hydrolysis and polycondensation reactions to proceed. The slightly viscous solution was then drop-casted on the porous

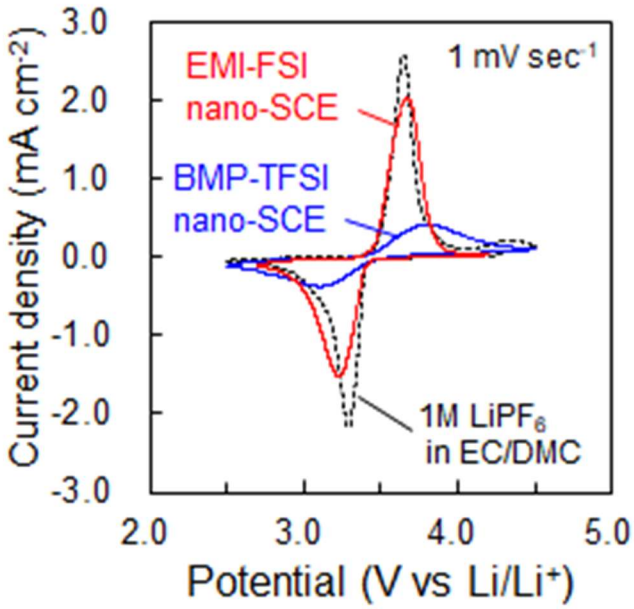

Fig. 4.6 Cyclic voltammograms of Li-LFP cells with BMP-TFSI nano-SCE (blue), EMI-FSI nano-SCE (red) and $LiPF_6$ in EC:DMC reference (black). The scan rate was 1 mV sec^{-1} and the cell temperature was 30 °C. Reprinted with permission from ref [113] Copyright 2020, IOP Science.

electrode punchout, which was placed in a coin cell. The precursor sol-gel solution penetrated into the porous electrode and was left for further gelation before they were dried and vacuum annealed. Figure 4.5 (d) shows the cross sectional SEM images of the LFP powder electrode impregnated with nano-SCE. No particle structure was observed as the nano-SCE had fully filled the openings in-between the particles of the electrode foils. The nano-SCE was found all the way down to the current collector foil, which meant that the nano-SCE had fully impregnated into the electrode. The average thickness of the nano-SCE impregnated electrode film was 33 μm; that is, close the nominal thickness of the LFP electrode (~30 μm), which meant that the binder kept the electrode structure intact during the nano-SCE impregnation process. Thus, the nano-SCE seemed to nicely fill the open space in the powder electrode and it did not break the binding structure between the active mass and the current collector, and so maintained a good electrical contact.

Cyclic voltammograms of the solid-state Li-LFP cells with both types of nano-SCE are presented in Fig. 4.6. For comparison, the wet cell with standard $LiPF_6$ in EC:DMC is also shown. Reversible anodic and cathodic peaks for the Li^+ extraction and insertion reaction were observed around 3.4 V versus Li^+/Li for both nano-SCEs. However, the peak current of the cell with EMI-FSI nano SCE was approximately 4 times higher than that of the BMP-TFSI nano-SCE based cell, and was comparable to that of the reference cell with liquid electrolytes. This was explained by the difference in Li^+ diffusion coefficient of the bulk electrolyte as Li-ion depletion in the porous electrodes was the likely mechanism (even though an effect of a slower diffusion constant through the SEI layer at the Li/SCE interface cannot be completely excluded). The larger peak separation for BMP-TFSI compared with EMI-FSI nano-SCE (0.72 V vs. 0.47 V) was then the result of a larger iR-drop over the SEI layers (and passivation layers for the cathodic currents)

at the Li/SCE interface. Note that the iR-drop also implied a slower effective scan rate (as the potential axis is also a time axis in cyclic voltammetry), which also contributed to the lower peak current. However, the difference in current was too large to be only explained by the difference in effective scan rate (a difference of approximately 0.4mV s^{-1} was estimated from the peak shift). The similar peak currents obtained for the EMI-FSI nano-SCE and reference cell showed that the Li^+ diffusion coefficients for the solid nano-SCE were similar to those of the liquid electrolyte solution. Additionally, the small peak shift of 80 mV indicated a small difference in the Ohmic drop for both electrolyte systems, which was remarkable as the thickness of EMI-FSI nano-SCE was 300–400 μm; that is, 20 times thicker than the separator thickness of 15 μm of the liquid reference cell (55 mV).

The lithiation (discharging) and delithiation (charging) characteristics of the different Li-LFP cells are shown in Fig. 4.7 (a) and (b). The same C-rate was used for the charge and discharge cycles without any additional constant voltage steps. The reference cell displayed the typical voltage-charge characteristics of Li-LFP cells with a flat plateau at 3.45 V versus Li^+/Li for delithiation and 3.38 V versus Li^+/Li for lithiation at 0.1C (Fig. 4.7 (b)).[125] As for the cyclic voltammograms, the cathodic lithiation and anodic delithiation voltage plateaus were symmetric around 3.42 V for all cells. The separation between the voltage plateaus was the largest for BMP-TFSI nano-SCE (0.12 V at 0.1C) and smallest (and equal) for the EMI-FSI nano-SCE and liquid reference (0.07 V at 0.1C), in accordance with the differences in the Ohmic drop shown in Fig. 4.6. As expected, the effect of the Ohmic drop was even more pronounced at a higher C-rate: for the BMP-TFSI nano-SCE with its resistive SEI at the Li/SCE interface, the plateau separation quickly exceeded 0.35 V at a 1C rate, whereas for the lower resistance EMI-FSI nano-SCE, the voltage separation was only 0.12 V for similar capacities measured at 1C, which

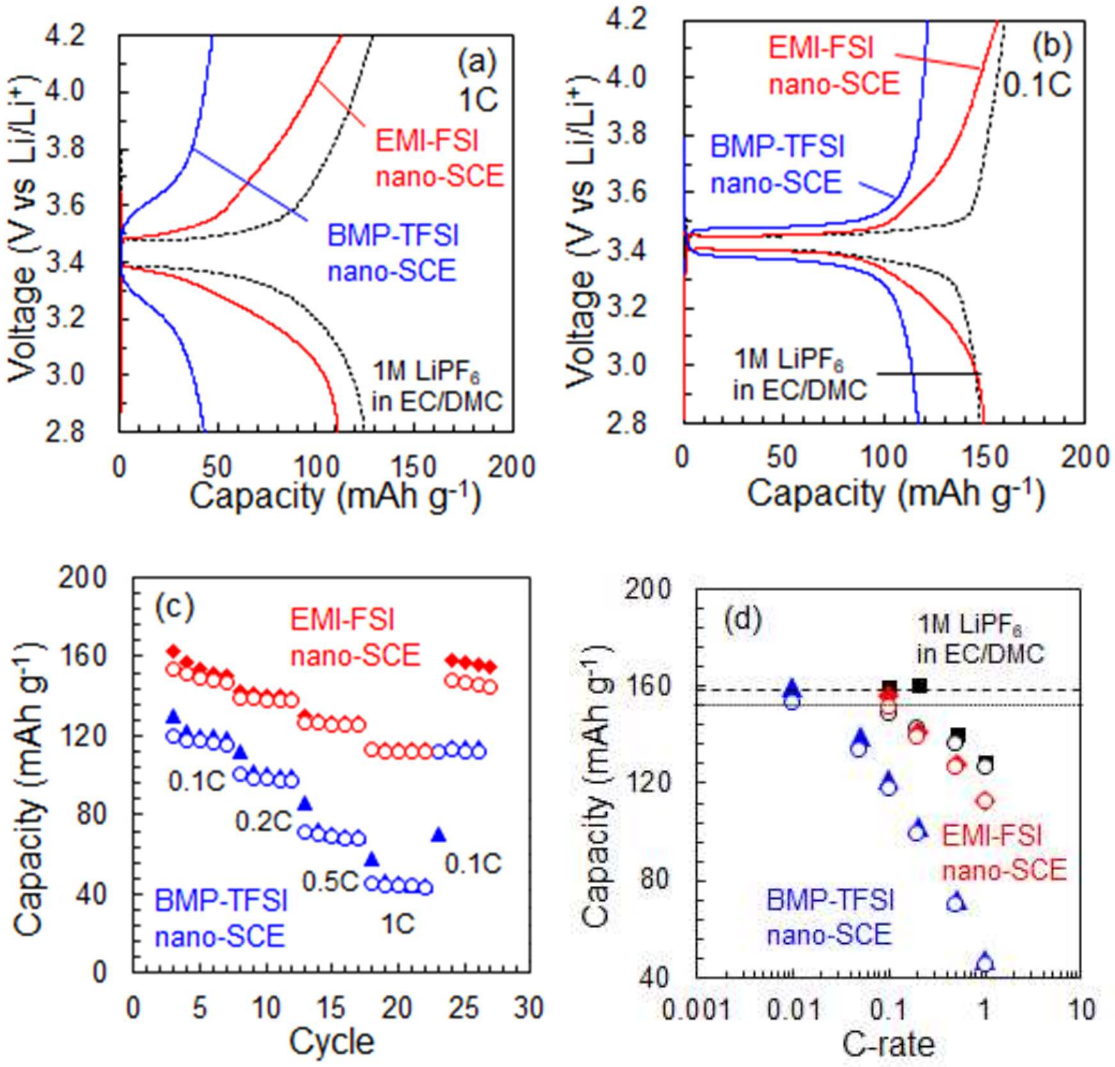

Fig. 4.7 Performance of Li-LFP cells with nano-SCEs cells with different electrolytes of BMP-Li-TFSI (blue), EMI-Li-FSI (red) and $LiPF_6$ in EC/DMC (black). Lithiation and delithiation characteristics at a C-rate of 1C (a) and 0.1C (b). Comparison of the C-rate performance of delithiation (closed symbol) and lithiation (open circle) (c) Cycle test at different C-rates and (d) cell capacity as a function of C-rate. The dashed and dotted lines are the maximum capacity of the lithiation and delithiation, respectively. The measurement temperature is 30 °C. Reprinted with permission from ref [113] Copyright 2020, IOP Science.

was comparable to the liquid reference electrolyte (0.1 V). The effect of the lower Li^+ diffusion coefficient for BMP-TFSI nano-SCE, as compared with EMI-FSI nano-SCE, was reflected in the achieved capacity limit. Indeed, the capacity of the solid-state cell with BMP-TFSI nano-SCE was limited to 120mAh g^{-1} and 45 mAh g^{-1} for 0.1C and 1.0C, respectively (or 80% and 30% of the reference cell). The capacity of the solid-state cell with EMI-FSI nano-SCE, however, had the same capacity (150 mAh g^{-1} or 100%) as the reference cell with a standard liquid electrolyte at 0.1C. Interestingly, the voltage profile for the EMI-FSI cell deviated from its flat plateau for a capacity > 100 mAh g^{-1}. This gradient profile was present for both the lithiation and delithiation cycles and thus could not be attributed only to the inhibition of the Li-dissolution reaction, as discussed for Fig. 3. Instead, I believed that the voltage increase arose from polarization as the result of diffusion limitation and ion depletion processes. The charge at this point was 0.0088 mAh cm^{-2}, which corresponded to a consumed Li^+ concentration of over 3 mol L^{-1} inside the LFP electrode (33 μm and 70% porosity); hence, over three times the Li-ion bulk concentration in the nano-SCE. The capacity of the solid-state cell with EMI-FSI nano-SCE still reached 113 mAh g^{-1} (75%) at 1.0C, which was only slightly below that for the liquid reference (128 mAh g^{-1} or 85% at 1C) and was drastically improved compared with the BMP-TFSI nano-SCE solid cell. In all cases, the coulombic efficiency was close to 100% at 1C, whereas the delithiation charge was somewhat higher than the lithiation charge at lower C-rates, which pointed to parasitic anodic electrolyte decomposition at LFP and Li^+ loss at Li during charging.

Figure 4.7 (c) shows the capacity of cells during cycling of the solid-state cells at varying C-rates. The second lithiation and delithiation cycles are plotted in Fig. 4.7 (d) together with the rate performance of the liquid reference cell. The rate performance of the solid battery with EMI-FSI matched that of the conventional liquid electrolyte cell at

Table 4.1 Comparison of the Li-LFP cell capacities with ternary composite electrolytes, which are composed of ionic liquid, Li-salt and porous-SiO_2 by sol-gel process.

Study	ref.	SiO_2 Precursor	Ionic liquids	Li-salt	Additives	LFP Electrode Thickness (mm)	Delithiation Capacity (mAh g^{-1})	Rate (C)	Temperature (°C)
Current work		TEOS	EMI-FSI	1M Li-FSI		30	150	0.1	30
			BMP-TFSI	1M Li-TFSI		30	120	0.1	30
Le Bideau et al., 2011	[26]	TMOS/MTMS	PYR13-TFSI	0.5M Li-TFSI		40	110	0.05	RT
F. Wu et al., 2011	[27]	TEOS	BMP-TFSI	1M Li-Tf		Not shown	145	0.1	30
Li et al., 2016	[54]	TEOS	PYR1201-TFSI P(DADMA)-TFSI	1M Li-TFSI		Not shown	148	0.2	25
Guyomard-Lack et al., 2014	[55]	TEOS	PYR13-TFSI	0.5 Li-TFSI	PVDF-HEA	Not shown	125	0.1	22

low C-rates and was only slightly lower for C-rates of >0.2C. A comparison of the Li-LFP cells using similar nano-SCE (or ionogels) composed of ionic liquids, Li-salts and porous-SiO_2 reported in the literature is summarized in Table 4.1.[126,127] The Li-LFP cell using EMI-FSI nano-SCE presented in this study showed the highest capacity at both 0.1C (150 mAh g^{-1}) and 1C (113 mAh g^{-1}). For the BMP-TFSI cell, however, the capacity dropped rapidly with increasing C-rate compared with the EMI-FSI cell. However, the delithiation charge of a series of C-rates (with decreasing C-rate), shown in Fig. 4.7 (c), was always higher than the following cycles within the same set of C-rates. This meant that the Li^+ insertion and extraction reaction in the BMP-TFSI system was limited by the lithiation step. This corresponded to the passivation of the anodic dissolution reaction, as inferred from the Li/nano-SCE three-electrode measurements shown in Fig. 4.3. In contrast, the difference of the cycle variation was smaller with the EMI-FSI cell as the anodic passivation at lithium was not limiting in this case. This demonstrated that the reaction kinetics were improved using EMI-FSI.

Both nano-SCE showed good cycle performance as the capacity at the final cycles

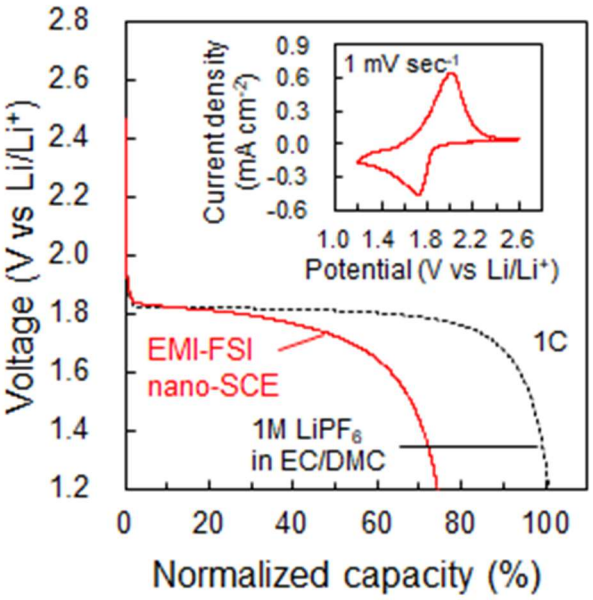

Fig. 4.8 Delithiation performance of LTO-LFP full cell with EMI-FSI nano-SCE (red full line) and 1M $LiPF_6$ in EC:DMC (black dotted line) at a C-rate of 1 C. The capacity was normalized to the capacitance of the cell with $LiPF_6$ in EC/DMC (black). The inset shows cyclic voltammogram at a scan rate of 1 mV s^{-1}. Reprinted with permission from ref [113] Copyright 2020, IOP Science.

(0.1C) returned to its original value at 0.1C. This implied that the volume change of the LFP electrode did not negatively affect the battery performance. The somewhat elastic properties of the nano-SCE were a major advantage compared with the rigid ceramic solid electrolytes. However, the silica matrix of the nano-SCE provides the mechanical support needed and suppresses Li-dendrite formation. The lithiation and delithiation performance was stable and reversible, that is, a stable battery performance was demonstrated with the EMI-FSI cell.

In addition, solid-state LTO-LFP cells with EMI-FSI nano-SCE were assembled. In this case, nano-SCE was impregnated both in the porous LFP cathode and in the porous LTO anode. The inset of Figure 4.8 shows a typical cyclic voltammogram of the cell.

Cathodic and anodic current peaks for Li^+ insertion and extraction were centered around 1.9 V, which corresponded to the difference between the potential of LFP (3.40 V vs. Li^+/Li) and of LTO (1.55 V vs. Li^+/Li). The lithiation curve of the solid-state cell was compared with that of a similar cell made with a conventional liquid electrolyte. The capacity was normalized to that of the liquid electrolyte. The capacity of the solid-state cell reached 70% of the liquid cell capacity even at 1C. These experiments demonstrate the functionality of the nano-SCE as Li-ion electrolyte and the feasibility for integration in Li-ion cells. Considering the electrochemical window of the EMI-FSI nano SCE, it may be used in combination with electrode materials such as graphite,[119,120] Si,[121] $LiFePO_4$,[108,122] $LiCoO_2$,[123] and $LiMn_{1/3}Co_{1/3}Ni_{1/3}O_2$.[124]

4.4 Conclusion

I have demonstrated a high-rate performance in solid-state lithium and Li-ion batteries using a silica-gel solid nanocomposite electrolyte of a FSI-based ionic liquid and Li-salt. The nano-SCE made with EMI-FSI and Li-FSI has a room-temperature ionic conductivity of 6.2 mS cm^{-1}, which is in the same range as standard organic liquid electrolytes conventionally used in LIBs. An advantage of the nano-SCE technology is that it can be impregnated into powder electrodes as a liquid precursor solution, which enables for complete filling of the pores and subsequent solidification. The capacity of the Li-LFP cell with EMI-Li-FSI SCE reached 150 mAh g^{-1} at 0.1C and 113 mAh g^{-1} at 1C. The C-rate performance of solid batteries with EMI-FSI nano-SCE was drastically improved compared with the cell with the BMP-TFSI SCE, and comparable to the cell with the conventional liquid electrolyte. The capacity of the solid-state batteries is the highest among the cells using ternary composite electrolytes reported so far with ionic

liquids, Li-salts and porous-SiO_2 made by sol-gel process. This clearly shows that the reaction kinetics at the interface of the active material and the nano-SCE are fast, which is a strong advantage compared with other types of solid electrolytes.

Chapter 5

General Conclusion and Future Prospects

This dissertation focused on providing new knowledge regarding the ion conduction behavior in nanopores in nano-SCEs and high-power performance of cells using nano-SCEs based on fundamental understanding.

In Chapter 1, background information on SE development and the requirements for high-performance SEs to realize ASSBs were summarized. To meet this demand, nano-SCEs were proposed as a novel concept in SEs. The surface conduction promotion effect was illustrated, as described in our previous study.

In Chapter 2, a method to analyze nanometer-sized and closed pores in porous silica was established using PALS. PALS analysis distinguished between the three types of open spaces in the silica matrix: vacancy (vacancy clusters); micropores between primary silica particles; and mesopores. This technique afforded the comprehensive understanding of the pore structure of the porous silica matrix of nano-SCEs when combined with SEM, TEM, and N_2 adsorption/desorption measurements.

In Chapter 3, the relationship between the pore structure of the silica matrix and its conduction behavior was clarified and the design of an ideal nanoporous structure to achieve a higher conductivity was described. It was revealed that the surface area was larger, corresponding to a reduction in the pore size, which increased the ILE/SiO_2 molar ratio. The surface enhancement degree was verified to increase with the thickness of the adsorbed ice-water layer on the silica surface, indicating that the conduction promotion effect originated from the strong hydrogen bonding in the ice-water layer. In addition, a

large number of small pores led to a severe pore confinement effect, which resulted in a decrease in the conductivity due to the increasing viscosity of ILE in the pores. To realize higher conductivity, nano-SCEs with a high surface area should be created using the optimum IL material to suppress the pore confinement effect.

In Chapter 4, the development of a new nano-SCE using a bis(fluorosulfonyl)imide (FSI)-based IL, which was selected to mitigate the pore confinement effect, was presented. A high C-rate performance in solid-state cells was demonstrated using this new nano-SCE. The capacity of Li-$LiFePO_4$ cell using the EMI-FSI-based nano-SCE was comparable to that of cells with conventional liquid electrolytes. These results also indicated that the nano-SCE fabrication process, especially the impregnation of a liquid precursor, was an efficient approach to producing excellent electrode/electrolyte interfacial contact in the solid composite electrode, as the reaction kinetics at the interface of the active mass and nano-SCE were sufficiently fast.

In conclusion, I succeeded in clarifying the ion conduction mechanism in the pores of nano-SCEs by analyzing the pore structure and internal ion conduction behavior. Stable and high-power cell performance was demonstrated by tuning the IL chemistry based on the ion conduction mechanism. The advantages of nano-SCEs over other types of SEs are described in this thesis.

To improve the conductivity of nano-SCEs and achieve extremely high-power performance in ASSBs, the surface enhancement effect must be maximized and the pore confinement effect must be minimized by tailoring the surface chemistry and nanostructure of the matrix. To suppress the pore confinement effect, the pore size is required to be controlled at approximately 30 nm; this was achieved using surfactants. In contrast, to improve the surface enhancement effect, surface chemistry can be tuned using

a functional ice-water layer. Ice-water is native to silica and therefore ideally suited for the systematic study the effect of surface functionalization on ion conduction promotion, as reported previously.[31] However, it is difficult to control the out-diffusion of water; thus, functional ice-water is not the best option for practical applications. Instead, the author proposes to find the best combination of the oxide, the adsorbed organic molecules on the oxide, and IL molecules, as the functional surface mesophase layer and its dipole depend on them. In this regard, the potential of 3-glycidyloxypropyl and 3-methacryloxypropyl molecules to act as functional groups that result in conductivity enhancement on the silica surface has been reported.[128,129] Other functional surface layers that provide similar or even greater surface promotion can now be developed.

In conclusion, by optimizing the functionalization of the oxide surface combined with maximizing the surface-to-volume ratio with optimal pore size, nano-SCEs with ion conductivities exceeding 10 mS cm^{-1} were engineered. These prepared materials are attractive for high-capacity batteries for automotive applications. Furthermore, the demonstrated principle of ion conduction enhancement can be applied to different ion systems, such as those suitable for sodium, magnesium, calcium, or aluminum ion batteries. In addition, the nano-SCE with interface conduction shown here is a concept rather than a single material; as such, it can be further engineered to achieve the desired properties of ion conduction, transport number, electrochemical window, safety, and cost, to generate various types of battery cells in the future.

References

[1] A. Yoshino, The Birth of the Lithium-ion Battery., Angew. Chemie Int. Ed. 51 (2012) 5798–800.

[2] B. Scrosati, History of lithium batteries, J. Solid State Electrochem. 15 (2011) 1623–1630.

[3] D.A. Notter, M. Gauch, R. Widmer, P. Wager, A. Stamp, R. Zah, H.-J. Althaus, Contribution of Li-Ion Batteries to the Environmental Impact of Electric Vehicles, Environ. Sci. Technol. 44 (2010) 6550–6556.

[4] M. Armand, J.-M. Tarascon, Building better batteries, Nature. 451 (2008) 652–657.

[5] B. Scrosati, J. Hassoun, Y.-K. Sun, Lithium-ion batteries. A look into the future, Energy Environ. Sci. 4 (2011) 3287–3295.

[6] J.B. Goodenough, Y. Kim, Challenges for Rechargeable Li Batteries, Chem. Mater. 22 (2010) 587–603.

[7] Q. Wang, P. Ping, X. Zhao, G. Chu, J. Sun, C. Chen, Thermal runaway caused fire and explosion of lithium ion battery, J. Power Sources. 208 (2012) 210–224.

[8] J.-M. Tarascon, M. Armand, Issues and challenges facing rechargeable lithium batteries, Nature. 414 (2001) 359–367.

[9] A. Manthiram, X. Yu, S. Wang, Lithium battery chemistries enabled by solid-state electrolytes, Nat. Rev. Mater. 2 (2017) 16103.

[10] X. Chen, P.M. Vereecken, Solid and Solid-Like Composite Electrolyte for Lithium Ion Batteries: Engineering the Ion Conductivity at Interfaces, Adv. Mater. Interfaces. 6 (2018) 1800899.

[11] X.-B. Cheng, R. Zhang, C.-Z. Zhao, Q. Zhang, Toward Safe Lithium Metal Anode in Rechargeable Batteries: A Review, Chem. Rev. 117 (2017) 10403–10473.

[12] C. Yang, K. Fu, Y. Zhang, E. Hitz, L. Hu, Protected Lithium-Metal Anodes in Batteries: From Liquid to Solid, Adv. Mater. 29 (2017) 1701169.

[13] M. Baba, N. Kumagai, H. Fujita, K. Ohta, K. Nishidate, S. Komaba, B. Kaplan, H. Groult, D. Devilliers, Multi-layered Li-ion rechargeable batteries for a high-voltage and high-current solid-state power source, J. Power Sources. 119–121 (2003) 914–917.

[14] Y. Gambe, Y. Sun, I. Honma, Development of Bipolar All-solid-state Lithium Battery Based on Quasi-solid-state Electrolyte Containing Tetraglyme-LiTFSA Equimolar Complex, Sci. Rep. 5 (2015) 8869.

[15] P. Knauth, Inorganic solid Li ion conductors: An overview, Solid State Ionics. 180 (2009) 911–916.

[16] J.C. Bachman, S. Muy, A. Grimaud, H.H. Chang, N. Pour, S.F. Lux, O. Paschos, F. Maglia, S. Lupart, P. Lamp, L. Giordano, Y. Shao-Horn, Inorganic Solid-State Electrolytes for Lithium Batteries: Mechanisms and Properties Governing Ion Conduction, Chem. Rev. 116 (2016) 140–162.

[17] Y. Kato, S. Hori, T. Saito, K. Suzuki, M. Hirayama, A. Mitsui, M. Yonemura, H. Iba, R. Kanno, High-power all-solid-state batteries using sulfide superionic conductors, Nat. Energy. 1 (2016) 16030.

[18] N. Kamaya, K. Homma, Y. Yamakawa, M. Hirayama, R. Kanno, M. Yonemura, T. Kamiyama, Y. Kato, S. Hama, K. Kawamoto, A. Mitsui, A lithium superionic conductor, Nat. Mater. 10 (2011) 682–686.

[19] Y. Wang, W.D. Richards, S.P. Ong, L.J. Miara, J.C. Kim, Y. Mo, G. Ceder,

Design principles for solid-state lithium superionic conductors, Nat. Mater. 14 (2015) 1026–1031.

[20] R.C. Agrawal, G.P. Pandey, Solid polymer electrolytes: materials designing and all-solid-state battery applications: an overview, J. Phys. D. Appl. Phys. 41 (2008) 223001.

[21] F.B. Dias, L. Plomp, J.B.J. Veldhuis, Trends in polymer electrolytes for secondary lithium batteries, J. Power Sources. 88 (2000) 169–191.

[22] T. Echelmeyer, H.W. Meyer, L. van Wiillen, Novel Ternary Composite Electrolytes: Li Ion Conducting Ionic Liquids in Silica Glass, Chem. Mater. 21 (2009) 2280–2285.

[23] T. Mizuno, W. Takeshi, M. Noriyoshi, O. Hiroyuki, Preparation of ion conductive inorganic–organic composite systems by in situ sol–gel reaction of polymerizable ionic liquids, Polym. Adv. Technol. 19 (2008) 1445–1450.

[24] J. Le Bideau, L. Viau, A. Vioux, Ionogels, ionic liquid based hybrid materials, Chem. Soc. Rev. 40 (2011) 907–925.

[25] D.S. Ashby, R.H. DeBlock, C.H. Lai, C.S. Choi, B.S. Dunn, Patternable, Solution-Processed Ionogels for Thin-Film Lithium-Ion Electrolytes, Joule. 1 (2017) 344–358.

[26] J. Le Bideau, J.-B. Ducros, P. Soudan, D. Guyomard, Solid-State Electrode Materials with Ionic-Liquid Properties for Energy Storage: the Lithium Solid-State Ionic-Liquid Concept, Adv. Funct. Mater. 21 (2011) 4073–4078.

[27] F. Wu, G. Tan, R. Chen, L. Li, J. Xiang, Y. Zheng, Novel Solid-State Li/LiFePO4 Battery Configuration with a Ternary Nanocomposite Electrolyte for Practical Applications, Adv. Mater. 23 (2011) 5081–5085.

[28] A. Vioux, B. Coasne, From Ionogels to Biredox Ionic Liquids: Some Emerging

Opportunities for Electrochemical Energy Storage and Conversion Devices, Adv. Energy Mater. 7 (2017) 1700883.

[29] N. Chen, H. Zhang, L. Li, R. Chen, S. Guo, Ionogel Electrolytes for High-Performance Lithium Batteries: A Review, Adv. Energy Mater. 8 (2018)

[30] M. Pratap Singh, R. Kumar Singh, S. Chandra, Ionic liquids confined in porous matrices: Physicochemical properties and applications, Prog. Mater. Sci. 64 (2014) 73–120.

[31] X. Chen, B. Put, A. Sagara, K.B. Gandrud, M. Murata, J.A. Steele, H. Yabe, T. Hantschel, M. Roeffaers, M. Tomoyama, H. Arase, Y. Kaneko, M. Shimarda, M. Mees, P.M. Vereecken, Silica gel solid nanocomposite electrolytes with interfacial conductivity promotion exceeding the bulk Li-ion conductivity of the ionic liquid electrolyte filler, Sci. Adv. 6 (2020) eaav3400.

[32] R. Hayes, G.G. Warr, A. Rob, At the interface: solvation and designing ionic liquids, Phys. Chem. Chem. Phys. 12 (2010) 1709.

[33] M. Mezger, H. Shiröder, H. Reichert, S. Schramm, J.S. Okasinski, S. Schöder, V. Honkimäki, M. Deutsch, B.M. Ocko, J. Ralston, M. Rohwerder, M. Stratmann, H. Dosch, Molecular Layering of Fluorinated Ionic Liquids at a Charged Sapphire (0001) Surface, Sicence. 322 (2008) 424–428.

[34] F. Federici Canova, H. Matsubara, M. Mizukami, K. Kurihara, A.L. Shluger, Shear dynamics of nanoconfined ionic liquids, Phys. Chem. Chem. Phys. 16 (2014) 8247–8256.

[35] K. Sakai, K. Okada, A. Uka, T. Misono, T. Endo, S. Sasaki, M. Abe, H. Sakai, Effects of water on solvation layers of imidazolium-type room temperature ionic liquids on silica and mica, Langmuir. 31 (2015) 6085–6091.

[36] D.B. Asay, S.H. Kim, Evolution of the Adsorbed Water Layer Structure on

Silicon Oxide at Room Temperature, J. Phys. Chem. B. 109 (2005) 16760–16763.

[37] A. Verdaguer, C. Weis, G. Oncins, G. Ketteler, H. Bluhm, M. Salmeron, Growth and Structure of Water on SiO2 films on Si Investigated by Kelvin Probe Microscopy and in Situ X-ray Spectroscopies, Langmuir. 23 (2007) 9699–9703.

[38] I.I. Slowing, B.G. Trewyn, S. Giri, V.S.-Y. Lin, Mesoporous Silica Nanoparticles for Drug Delivery and Biosensing Applications, Adv. Funct. Mater. 17 (2007) 1225–1236.

[39] I.I. Slowing, J.L. Vivero-Escoto, B.G. Trewyn, V.S.-Y. Lin, Mesoporous silica nanoparticles: structural design and applications, J. Mater. Chem. 20 (2010) 7924–7937.

[40] Z. Li, J.C. Barnes, A. Bosoy, J.F. Stoddart, J.I. Zink, Mesoporous silica nanoparticles in biomedical applications, Chem. Soc. Rev. 41 (2012) 2590–2605.

[41] M. Sun, C. Chen, L. Chen, B. Su, Hierarchically porous materials: Synthesis strategies and emerging applications, Front. Chem. Sci. Eng. 10 (2016) 301–347.

[42] L.L. Hench, J.K. West, The Sol-Gel Process, Chem. Rev. 90 (1990) 33–72.

[43] R. Ciriminna, A. Fidalgo, V. Pandarus, F. Béland, L.M. Ilharco, M. Pagliaro, The Sol-Gel Route to Advanced Silica-Based Materials and Recent Applications, Chem. Rev. 113 (2013) 6592–6620.

[44] C. T. Kresge, M. E. Leonowicz, W. J. Roth, J. C. Vartuli, J. S. Beck, Ordered mesoporous molecular sieves synthesized by a liquid-crystal template mechanism, Nature. 359 (1992) 710–712.

[45] B.T. Holland, C.F. Blanford, A. Stein, Synthesis of Macroporous Minerals with Highly Ordered Three-Dimensional Arrays of Spheroidal Voids, Science (80-.). 281 (1998) 538–540.

[46] D. Zhao, J. Feng, Q. Huo, N. Melosh, G.H. Fredrickson, B.F. Chmelka, G.D. Stucky, Triblock Copolymer Syntheses of Mesoporous Silica with Periodic 50 to 300 Angstrom Pores, Science (80-.). 279 (1998) 548–552.

[47] A. Feinle, M.S. Elsaesser, N. Hüsing, Sol-gel synthesis of monolithic materials with hierarchical porosity, Chem. Soc. Rev. 45 (2016) 3377.

[48] T. Welton, Room-Temperature Ionic Liquids. Solvents for Synthesis and Catalysis, Chem. Rev. 99 (1999) 2071–2083.

[49] J.P. Hallett, T. Welton, Room-Temperature Ionic Liquids: Solvents for Synthesis and Catalysis. 2, Chem. Rev. 111 (2011) 3508–3576.

[50] S. Dai, Y.H. Ju, H.J. Gao, J.S. Lin, S.J. Pennycook, C.E. Barnes, Preparation of silica aerogel using ionic liquids as solvents, Chem. Commun. (2000) 243–244.

[51] Y. Zhou, J.H. Schattka, M. Antonietti, Room-Temperature Ionic Liquids as Template to Monolithic Mesoporous Silica with Wormlike Pores via a Sol−Gel Nanocasting Technique, Nano Lett. 4 (2004) 477–481.

[52] Y. Zhou, M. Antonietti, A Series of Highly Ordered, Super-Microporous, Lamellar Silicas Prepared by Nanocasting with Ionic Liquids, Chem. Mater. 16 (2004) 544–550.

[53] Y. Zhou, M. Antonietti, Preparation of Highly Ordered Monolithic Super-Microporous Lamellar Silica with a Room-Temperature Ionic Liquid as Template via the Nanocasting Technique, Adv. Mater. 15 (2003) 1452–1455.

[54] K. Zhu, F. Požgan, L. D'Souza, R.M. Richards, Ionic liquid templated high surface area mesoporous silica and Ru–SiO2, Microporous Mesoporous Mater. 91 (2006) 40–46.

[55] M.A. Klingshirn, S.K. Spear, J.D. Holbrey, R.D. Rogers, Ionic liquids as solvent and solvent additives for the synthesis of sol–gel materials, J. Mater. Chem. 15

(2005) 5174–5180.

[56] S.S. Çok, F. Koç, F. Balkan, N. Gizli, Exploring a new preparation pathway for the synthesis of silica based xerogels as crack-free monoliths, Ceram. Int. 45 (2019) 1616–1626.

[57] J. Zhang, Y. Ma, F. Shi, L. Liu, Y. Deng, Room temperature ionic liquids as templates in the synthesis of mesoporous silica via a sol–gel method, Microporous Mesoporous Mater. 119 (2009) 97–103.

[58] K.M.S. Meera, R.M. Sankar, S.N. Jaisankar, A.B. Mandal, Mesoporous and biocompatible surface active silica aerogel synthesis using choline formate ionic liquid, Colloids Surfaces B Biointerfaces. 86 (2011) 292–297.

[59] C.-M. Wu, S.-Y. Lin, H.-L. Chen, Structure of a monolithic silica aerogel prepared from a short-chain ionic liquid, Microporous Mesoporous Mater. 156 (2012) 189–195.

[60] K.S. Yoo, T.G. Lee, J. Kim, Preparation and characterization of mesoporous TiO2 particles by modified sol–gel method using ionic liquids, Microporous Mesoporous Mater. 84 (2005) 211–217.

[61] N. Žilková, A. Zukel, J. Čejka, Synthesis of organized mesoporous alumina templated with ionic liquids, Microporous Mesoporous Mater. 95 (2006) 176–179.

[62] K.S.W. Sing, D.H. Everett, R.A.W. Haul, L. Moscou, R.A. Pierotti, J. Rouquerol, T. Siemieniewska, Reporting Physisorption Data for Gas/Solid Systems with Special Reference to the Determination of Surface Area and Porosity, Pure Appl. Chem. 57 (1985) 603–619.

[63] Y. Wan, D. Zhao, On the Controllable Soft-Templating Approach to Mesoporous Silicates, Chem. Rev. 107 (2007) 2821–2860.

[64] R.W. Siegel, POSITRON ANNIHILATION SPECTROSCOPY, Annu. Rev. Mater. Sci. 10 (1980) 393–425.

[65] M.J. Puska, R.M. Nieminen, Theory of positrons in solids and on solid surfaces, Rev. Mod. Phys. 66 (1994) 841–897.

[66] F. Tuomisto, I. Makkonen, Defect identification in semiconductors with positron annihilation: Experiment and theory, Rev. Mod. Phys. 85 (2013) 1583–1631.

[67] A. Sagara, M. Hiraiwa, A. Uedono, N. Oshima, R. Suzuki, S. Shibata, Residual defects in low-dose arsenic-implanted silicon after high-temperature annealing, Nucl. Instruments Methods Phys. Res. B. 321 (2014) 54–58.

[68] D.W. Gidley, H.-G. Peng, R.S. Vallery, Positron Annihilation As a Method To Characterize Porous Materials, Annu. Rev. Mater. Res. 36 (2006) 49–79.

[69] C.J. Brinker, HYDROLYSIS AND CONDENSATION OF SILICATES: EFFECTS ON STRUCTURE, J. Non. Cryst. Solids. 100 (1988) 31–50.

[70] S. Brunauer, P.H. Emmett, E. Teller, Adsorption of Gases in Multimolecular Layers, J. Am. Chem. Soc. 60 (1936) 309–319.

[71] M. Thommes, K. Kaneko, A. V. Neimark, J.P. Olivier, F. Rodriguez-Reinoso, J. Rouquerol, K.S.W. Sing, Physisorption of gases, with special reference to the evaluation of surface area and pore size distribution (IUPAC Technical Report), Pure Appl. Chem. 87 (2015) 1051–1069.

[72] E.P. Barrett, L.G. Joyner, P.P. Halenda, The Determination of Pore Volume and Area Distributions in Porous Substances. I. Computations from Nitrogen Isotherms, J. Am. Chem. Soc. 73 (1951) 373–380.

[73] A. Uedono, S. Armini, Y. Zhang, T. Kakizaki, R. Krause-Rehberg, W. Anwand, A. Wagner, Surface sealing using self-assembled monolayers and its effect on metal diffusion in porous low-k dielectrics studied using monoenergetic positron

beams, Appl. Surf. Sci. 368 (2016) 272–276.

[74] H. Saito, T. Hyodo, Improvement in the gamma-ray timing measurements using a fast digital oscilloscope, Radiat. Phys. Chem. 68 (2003) 431–434.

[75] R.B. Gregory, Analysis of positron annihilation lifetime data by numerical Laplace inversion: Corrections for source terms and zero-time shift errors, Nucl. Instruments Methods Phys. Res. A. 302 (1991) 496–507.

[76] R.B. Gregory, Free-volume and pore size distributions determined by numerical Laplace inversion of positron annihilation lifetime data, J. Appl. Phys. 70 (1991) 4665–4670.

[77] R.B. Gregory, Y. Zhu, ANALYSIS OF POSITRON ANNIHILATION LIFETIME DATA BY NUMELICAL LAPLACE INVERSION WITH THE PROGRAM CONTIN, Nucl. Instruments Methods Phys. Res. A. 290 (1990) 172–182.

[78] S.W. Provencher, CONTIN: A GENERAL PURPOSE CONSTRAINED REGULATION PROGRAM FOR INVERTING NOISY LINEAR ALGEBRAIC AND INTEGRAL EQUATIONS, Comput. Phys. Commun. 27 (1982) 229–242.

[79] D.W. Gidley, W.E. Frieze, T.L. Dull, A.F. Yee, E.T. Ryan, H.-M. Ho, Positronium annihilation in mesoporous thin films, Phys. Rev. B. 60 (1999) R5157–R5160.

[80] T.L. Dull, W.E. Frieze, D.W. Gidley, J.N. Sun, A.F. Yee, Determination of Pore Size in Mesoporous Thin Films from the Annihilation Lifetime of Positronium, J. Phys. Chem. B. 105 (2001) 4657–4662.

[81] R. Zaleski, EELViS. http://sourceforge.net/projects/eelvis/ Accessed: February 20, 2015., (n.d.).

[82] A. Sagara, H. Yabe, X. Chen, P.M. Vereecken, A. Uedono, Pore structure

analysis of ionic liquid-templated porous silica using positron annihilation lifetime spectroscopy, Microporous Mesoporous Mater. 295 (2020) 109964.

[83] A.E. Ruark, Positronium, Phys. Rev. 68 (1945) 278.

[84] O.E. Mogensen, Spur reaction model of positronium formation, J. Chem. Phys. 60 (1974) 998–1004.

[85] S.J. Tao, Positronium Annihilation in Molecular Substances, J. Chem. Phys. 56 (1972) 5499–5510.

[86] R.L. Garwin, Thermalization of Positrons in Metals, Phys. Rev. 91 (1953) 1571–1572.

[87] S.Y. Chuang, S.J. Tao, Study of Various Properties of Silica Gel by Positron Annihilation, J. Chem. Phys. 54 (1971) 4902–4907.

[88] M.A. Misheva, N. Djourelov, F.M.A. Margaca, I.M.M. Salvado, G. Passage, A study of free-volume hole distributions in xTiO2·(1−x)SiO2 by positron annihilation spectroscopy, J. Phys. Condens. Matter. 8 (1996) 6313–6321.

[89] A. Uedono, S. Tanigawa, Positron annihilation in vitreous silica glasses, Jpn. J. Appl. Phys. 32 (1993) 2681–2691.

[90] S. Dannefaer, T. Bretagnon, D. Kerr, Vacancy-type defects in crystalline and amorphous SiO2, J. Appl. Phys. 74 (1993) 884–890.

[91] M. Misheva, N. Djourelov, F.M.A. Margaca, I.M.M. Salvado, Positronium study of porous structure of sol-gel prepared SiO2: influence of pH, J. Non. Cryst. Solids. 279 (2001) 196–203.

[92] A. Uedono, S. Watauchi, Y. Ujihira, O. Yoda, Defects in electron irradiated amorphous SiO2 probed by positron annihilation, Hyperfine Interact. 84 (1994) 225–230.

[93] M. Hasegawa, M. Saneyasu, M. Tabata, Z. Tang, Y. Nagai, T. Chiba, Y. Ito,

Positron and positronium studies of irradiation-induced defects and microvoids in vitreous metamict silica, Nucl. Instruments Methods Phys. Res. Sect. B Beam Interact. with Mater. Atoms. 166 (2000) 431–439.

[94] D. Dutta, B.N. Ganguly, D. Gangopadhyay, T. Mukherjee, B. Dutta-Roy, Microstructural Study of Silica Gel by Positron Annihilation, J. Phys. Chem. B. 108 (2004) 8947–8952.

[95] I. Mincov, M.P. Petkov, P. Thou, T. Troev, Porosity characterization of aerogels using positron annihilation lifetime spectroscopy, J. Non. Cryst. Solids. 350 (2004) 253–258.

[96] B.S. Cooper, J.-P. Boilot, C. Corbel, F. Guillemot, L. Gurung, L. Liszkay, D.B. Cassidy, Annihilation of positronium atoms confined in mesoporous and macroporous SiO2 films, Phys. Rev. B. 97 (2018) 205302.

[97] P.H. Tewari, A.J. Hunt, K.D. Lofftus, Ambient-temperature supercritical drying of transparent silica aerogels, Mater. Lett. 3 (1985) 363–367.

[98] S. Yoda, S. Ohshima, Supercritical drying media modification for silica aerogel preparation, J. Non. Cryst. Solids. 248 (1999) 224–234.

[99] P.H. Brauner, S, Emmett, Adsorption of Gases in Multimolecular Layers, J. Am. Chem. Soc. 407 (1936).

[100] P. Kirkegaard, M. Eldrup, O.E. Mogensen, N.J. Pedersen, Program system for analysing positron lifetime spectra and angular correlation curves, Comput. Phys. Commun. 23 (1981) 307–335.

[101] D.W. Gidley, H.-G. Peng, R.S. Vallery, Positron Annihilation as a Method to Characterize Porous Materials, Annu. Rev. Mater. Res. 36 (2006) 49–79.

[102] A. Sagara, H. Yabe, X. Chen, B. Put, T. Hantschel, M. Mees, H. Arase, Y. Kaneko, A. Uedono, P.M. Vereecken, Interfacial Conductivity Enhancement and

Pore Con fi nement Conductivity-Lowering Behavior inside the Nanopores of Solid Silica-gel Nanocomposite Electrolytes, ACS Appl. Mater. Interfaces. 13 (2021) 40543–40551.

[103] Y. Umebayashi, T. Mitsugi, S. Fukuda, T. Fujimori, K. Fujii, R. Kanzaki, M. Takeuchi, S.I. Ishiguro, Lithium ion solvation in room-temperature ionic liquids involving bis(trifluoromethanesulfonyl) imide anion studied by Raman spectroscopy and DFT calculations, J. Phys. Chem. B. 111 (2007) 13028–13032.

[104] S. Zhang, J. Zhang, Y. Zhang, Y. Deng, Nanoconfined Ionic Liquids, Chem. Rev. 117 (2017) 6755–6833.

[105] G.B. Appetecchi, M. Montanino, A. Balducci, S.F. Lux, M. Winterb, S. Passerini, Lithium insertion in graphite from ternary ionic liquid-lithium salt electrolytes. I. Electrochemical characterization of the electrolytes, J. Power Sources. 192 (2009) 599–605.

[106] S.F. Lux, M. Schmuck, G.B. Appetecchi, S. Passerini, M. Winter, A. Balducci, Lithium insertion in graphite from ternary ionic liquid-lithium salt electrolytes: II. Evaluation of specific capacity and cycling efficiency and stability at room temperature, J. Power Sources. 192 (2009) 606–611.

[107] A.S. Best, A.I. Bhatt, A.F. Hollenkamp, Ionic Liquids with the Bis(fluorosulfonyl)imide Anion: Electrochemical Properties and Applications in Battery Technology, J. Electrochem. Soc. 157 (2010) A903–A911.

[108] A. Guerfi, S. Duchesne, Y. Kobayashi, A. Vijh, K. Zaghib, LiFePO4 and graphite electrodes with ionic liquids based on bis(fluorosulfonyl)imide (FSI)- for Li-ion batteries, J. Power Sources. 175 (2008) 866–873.

[109] I.A. Shkrob, T.W. Marin, Y. Zhu, D.P. Abraham, Why Bis(fluorosulfonyl)imide Is a “Magic Anion” for Electrochemistry, J. Phys. Chem. C. 118 (2014) 19661–

19671.

[110] H. Zhang, W. Feng, J. Nie, Z. Zhou, Recent progresses on electrolytes of fluorosulfonimide anions for improving the performances of rechargeable Li and Li-ion battery, J. Fluor. Chem. 174 (2015) 49–61.

[111] K. Matsumoto, E. Nishiwaki, T. Hosokawa, S. Tawa, T. Nohira, R. Hagiwara, Thermal, Physical, and Electrochemical Properties of Li[N(SO2F)2]-[1-Ethyl-3-methylimidazolium][N(SO2F)2] Ionic Liquid Electrolytes for Li Secondary Batteries Operated at Room and Intermediate Temperatures, J. Phys. Chem. C. 121 (2017) 9209–9219.

[112] E.O. Stejskal, J.E. Tanner, Spin Diffusion Measurements: Spin Echoes in the Presence of a Time Dependent Field Gradien, J. Chem. Phys. 42 (1965) 288–292

[113] A. Sagara, X. Chen, K.B. Gandrud, M. Murata, M. Mees, Y. Kaneko, H. Arase, P.M. Vereecken, High-Rate Performance Solid-State Lithium Batteries with Silica-Gel Solid Nanocomposite Electrolytes using Bis(fluorosulfonyl)imide-Based Ionic Liquid, J. Electrochem. Soc. 167 (2020) 070549.

[114] C.J.F. Solano, S. Jeremias, E. Paillard, D. Beljonne, R. Lazzaroni, A joint theoretical/experimental study of the structure, dynamics, and Li+ transport in bis([tri]fluoro[methane]sulfonyl)imide [T]FSI-based ionic liquids, Jounal Chem. Phys. 139 (2013) 034502.

[115] M. Kerner, N. Plylahan, J. Scheers, P. Johansson, Ionic liquid based lithium battery electrolytes: fundamental benefits of utilising both TFSI and FSI anions?, Phys. Chem. Chem. Phys. 17 (2015) 19569–19581.

[116] O. Borodin, W. Gorecki, G.D. Smith, M. Armand, Molecular Dynamics Simulation and Pulsed-Field Gradient NMR Studies of Bis(fluorosulfonyl)imide (FSI) and Bis[(trifluoromethyl)sulfonyl]imide (TFSI)-Based Ionic Liquids, J.

Phys. Chem. B. 114 (2010) 6786–6798.

[117] K. Fujii, H. Hamano, H. Doi, X. Song, S. Tsuzuki, K. Hayamizu, S. Seki, Y. Kameda, K. Dokko, M. Watanabe, Y. Umebayashi, Unusual Li+ Ion Solvation Structure in Bis(fluorosulfonyl)amide Based Ionic Liquid, J. Phys. Chem. C. 117 (2013) 19314–19324.

[118] Z.P. Rosol, N.J. German, S.M. Gross, Solubility, ionic conductivity and viscosity of lithium salts in room temperature ionic liquids, Green Chem. 11 (2009) 1453–1457.

[119] T. Sugimoto, Y. Atsumi, M. Kikuta, E. Ishiko, M. Kono, M. Ishikawa, Ionic liquid electrolyte systems based on bis(fluorosulfonyl)imide for lithium-ion batteries, J. Power Sources. 189 (2009) 802–805.

[120] S. Seki, Y. Kobayashi, H. Miyashiro, Y. Ohno, Y. Mita, N. Terada, P. Charest, A. Guerfi, K. Zaghib, Compatibility of N-methyl-N-propylpyrroIidinium cation room-temperature ionic liquid electrolytes and graphite electrodes, J. Phys. Chem. C. 112 (2008) 16708–16713.

[121] B. Philippe, R. Dedryvèire, M. Gorgoi, H. Rensmo, D. Gonbeau, K. Edström, Improved Performances of Nanosilicon Electrodes Using the Salt LiFSI: A Photoelectron Spectroscopy Study, J. Am. Chem. Soc. 135 (2013) 9829–9842.

[122] A.P. Lewandowski, A.F. Hollenkamp, S.W. Donne, A.S. Best, Cycling and rate performance of Li-LiFePO4 cells in mixed FSI-TFSI room temperature ionic liquids, J. Power Sources. 195 (2010) 2029–2035.

[123] H. Matsumoto, H. Sakaebe, K. Tatsumi, M. Kikuta, E. Ishiko, M. Kono, Fast cycling of Li/LiCoO2 cell with low-viscosity ionic liquids based on bis(fluorosulfonyl)imide [FSI]-, J. Power Sources. 160 (2006) 1308–1313.

[124] Y. Matsui, S. Kawagushi, T. Sugimoto, M. Kikuta, T. Higashizaki, M. Kono, M.

Yamagata, M. Ishikawa, Charge-Discharge Characteristics of a LiNi1/3Mn1/3Co1/3O2 Cathode in FSI-based Ionic Liquids, Electrochemistry. 80 (2012) 808–811.

[125] A.K. Padhi, K.S. Nanjundaswamy, J.B. Goodenough, Phospho-olivines as Positive-Electrode Materials for Rechargeable Lithium Batteries, Jounal Electrochem. Soc. 144 (1997) 1188–1194.

[126] X. Li, S. Li, Z. Zhang, J. Huang, L. Yang, S. Hirano, High-performance polymeric ionic liquid-silica hybrid ionogel electrolytes for lithium metal batteries, J. Mater. Chem. A. 4 (2016) 13822–13829.

[127] A. Guyomard-Lack, J. Abusleme, P. Soudan, B. Lestriez, D. Guyomard, J. Le Bideau, Hybrid Silica–Polymer Ionogel Solid Electrolyte with Tunable Properties, Adv. Energy Mater. 4 (2014) 1301570.

[128] F. Wu, N. Chen, R. Chen, L. Wang, L. Li, Organically modified silica-supported ionogels electrolyte for high temperature lithium-ion batteries, Nano Energy. 31 (2017) 9–18.

[129] N. Chen, Y. Dai, Y. Xing, L. Wang, C. Guo, R. Chen, S. Guo, F. Wu, Biomimetic ant-nest ionogel electrolyte boosts the performance of dendrite-free lithium batteries, Energy Environ. Sci. 10 (2017) 1660–1667.

List of Achievements

Peer-reviewed Journal publications

1. Xubin Chen, Brecht Put, Akihiko Sagara, Knut Gandrud, Mitsuhiro Murata, Julian A. Steele, Hiroki Yabe, Thomas Hantschel, Maarten Roeffaers, Morio Tomiyama, Hidekazu Arase, Yukihiro Kaneko, Mikinari Shimada, Maarten Mees, and Philippe M. Vereecken, Silica-gel Solid Nanocomposite Electrolyte with Interfacial Conductivity Promotion Exceeding the Bulk Li-ion Conductivity of the Filler, Science Advances 6, eaav3400 (2020).

2. Akihiko Sagara, Hiroki Yabe, Xubin Chen, Philippe M. Vereecken, and Akira Uedono, Pore structure analysis of ionic liquid-templated porous silica using positron annihilation lifetime spectroscopy, Microporous and Mesoporous Materials 295 109964 (2020).

3. Akihiko Sagara, Xubin Chen, Knut B. Gandrud, Mitsuhiro Murata, Maarten Mees, Yukihiro Kaneko, Hidekazu Arase, and Philippe M. Vereecken, High-rate Performance Solid-State Lithium Batteries with Silica-gel Solid Nanocomposite Electrolytes using Bis(fluorosulfonyl)imide-based Ionic Liquid, Journal of the Electrochemistry 167 070549 (2020).

4. Akihiko Sagara, Hiroki Yabe, Xubin Chen, Brecht Put, Thomas Hantschel, Maarten Mees, Hidekazu Arase, Yukihiro Kaneko, Akira Uedono, and Philippe M. Vereecken,

Interfacial Conductivity Enhancement and Pore Confinement Conductivity-Lowering Behavior inside the Nanopores of Solid Silica-gel Nanocomposite Electrolytes, ACS Applied Materials and Interfaces 13 40453-40551. (2021).

Conferences and Seminars

1. 村田充弘, 相良暁彦, 富山盛央, 嶋田幹也, Xubin Chen, Knut Gandrud, Maarten Mees, Philippe M. Vereecken, メソポーラスシリカからなるナノコンポジット固体電解質のリチウムイオン電導性と内部構造, 第 58 回電池討論会, 2E07 (2017)

2. Xubin Chen, Knut Gandrud, Maarten Mees, Akihiko Sagara, Mitsuhiro Murata, Morio Tomiyama, Mikinari Shimada, Philippe M. Vereecken, Mechanism analysis of Li-ion conductivity enhancement in porous silica-based solid nanocomposite electrolytes, The 58th Battery Symposium in Japan, 3H16 (2017).

3. Akihiko Sagara, Mitsuhiro Murata, Morio Tomiyama, Mikinari Shimada, Xubin Chen, Knut Gandrud, Maarten Mees, Philippe M. Vereecken, Enhancement of Li-Ion Conductivity in a Mesoporous Silica-Based Solid Nanocomposite Electrolyte, 2017 Materials Research Society (MRS) Fall Meeting & Exhibit, ES04.14.25 (2017).

4. Maarten Debucquoy, Maarten Mees, Xubin Chen, Knut B. Gandrud, Brecht Put, Christine De Nooijer, Jos F. M. Oudenhoven, K. Van Nieuwenhuysen, Nathalie. Hendrickx, Nick. Clerckx, Akihiko Sagara, Mitsuhiro Murata, Morio Tomiyama, Mikinari Shimada, Philippe M. Vereecken, A novel solid nanocomposite electrolyte

for high performance batteries, 8th International Advanced Automotive Battery Conference (AABC) Europe, (2018).

5. Xubin Chen, Knut Gandrud, Maarten Mees, Akihiko Sagara, Mitsuhiro Murata, Morio Tomiyama, Mikinari Shimada, Philippe M. Vereecken, Mechanisum analysis of Li-ion conducitivity enhancement in porous silica-based solid nanocomposite electrolytes, European Materials Research Society (E-MRS) 2018 Spring Meeting, R.7.2 (2018).

6. Philippe M. Vereecken, Xubin Chen, Knut Bjarne Gandrud, Brecht Put, Akihiko Sagara, Mitsuhiro Murata, Morio Tomiyama, Yukihiro Kaneko, Mikinari Shimada, Julian Steele, Maarten Roeffaers, Maarten Debucquoy and Maarten J. Mees, Mechanism Analysis of Enhanced Li-Ion Conductivity in Mesoporous Silica-Based Solid Nano-composite Electrolytes, Americas International Meeting on Electrochemistry and Solid State Science (AiMES) 2018, A06-0470 (2018).

7. Akihiko Sagara, Knut B. Gandrud, Xubin Chen, Mitsuhiro Murata, Maarten Mees, Yukihiro Kaneko, Hidekazu Arase, Mikinari Shimada, Philippe M. Vereecken, High-Power Solid State Batteries with Silica-gel Solid Nanocomposite Electrolytes using FSI-based Ionic Liquids, 9th Advanced Automotive Battery Conference (AABC) Europe, (2019).

8. Maarten Debucquoy, Maarten Mees, Akihiko Sagara, Xubin Chen, Knut B. Gandrud, Brecht Put, Hidekazu Arase, Yukihiro Kaneko, Philippe M. Vereecken, Solid-State Lithium and Li-ion Batteries with Silica-gel Solid Nanocomposite Electrolytes, 9th

Advanced Automotive Battery Conference (AABC) Europe, (2019).

9. Maarten J. Mees, Akihiko Sagara, Maarten Debucquoy, Xubin Chen, Knut Bjarne Gandrud, Brecht Put, Hidekazu Arase, Yukihiro Kaneko, Philippe M. Vereecken, Solid-State Lithium and Li-ion Batteries with Silica-gel Solid Nanocomposite Electrolytes, 235th ECS Meeting, A02-0148 (2019).

10. Xubin Chen, Knut Bjarne Gandrud, Akihiko Sagara, Brecht Put, Mitsuhiro Murata, Hiroki Yabe, Morio Tomiyama, Hidekazu Arase, Yukihiro Kaneko, Mikinari Shimada, Julian Steele, Maarten Roeffaers, Maarten Debucquoy, Maarten J. Mees, Philippe M. Vereecken, Solid Nano-Composite Electrolytes (nano-SCE) with Ion Conductivity Promotion at an Interfacial Ice Layer on the Mesoporous Silica Matrix, 235th ECS Meeting, A02-0285 (2019).

11. Simon Hollevoet, Brecht Put, Akihiko Sagara, Nouha Labyedh, Yukihiro Kaneko, Hidekazu Arase, Maarten Mees, Philippe M. Vereecken, Conductivity enhancement at the thin-film ionic liquid electrolyte/SiO2 interface, European Materials Research Society (E-MRS) 2019 Spring Meeting, C.5.1 (2019).

12. Brecht Put, Simon Hollevoet, Akihiko Sagara, Nouha Labyedh, Nick Clerckx, Nathalie Hendrickx, Yukihiro Kaneko, Hidekazu Arase, Maarten J. Mees, Philippe M. Vereecken, Direct Measurement of Enhanced Ion Conductivity at an Ionic Liquid Electrolyte (ILE)/SiO2 Interface with Interdigitated Electrode Array, Electrochemical Conference on Energy and the Environment: Bioelectrochemistry and Energy Storage (ECEE) 2019, A03-0163 (2019).

13. Xubin Chen, Knut Bjarne Gandrud, Akihiko Sagara, Brecht Put, Mitsuhiro Murata, Hiroki Yabe, Morio Tomiyama, Hidekazu Arase, Yukihiro Kaneko, Mikinari Shimada, Julian Steele, Maarten Roeffaers, Maarten Debucquoy, Maarten J. Mees, Philippe M. Vereecken, Solid Nano-Composite Electrolytes (nano-SCE) with Ion Conductivity Promotion at an Interfacial Ice Layer on the Mesoporous Silica Matrix, Electrochemical Conference on Energy and the Environment: Bioelectrochemistry and Energy Storage (ECEE) 2019, A06-0314 (2019).

14. Maarten Debucquoy, Maarten J. Mees, Akihiko Sagara, Sergey Remizov, Xubin Chen, Knut Bjarne Gandrud, Brecht Put, Yukihiro Kaneko, Philippe M. Vereecken, Solid-State Lithium and Li-Ion Batteries with Solid Nano-Composite Electrolytes, Electrochemical Conference on Energy and the Environment: Bioelectrochemistry and Energy Storage (ECEE) 2019, A06-0354 (2019).

15. Maarten J. Mees, Knut Bjarne Gandrud, Akihiko Sagara, Xubin Chen, Nathalie Hendrickx, Mitsuhiro Murata, Yukihiro Kaneko, Hidekazu Arase, Philippe M. Vereecken, A Novel Material Class of Solid-State Nano-Composite Electrolytes with High Li-Ion Conductivity, Electrochemical Conference on Energy and the Environment: Bioelectrochemistry and Energy Storage (ECEE) 2019, A06-0358 (2019).

16. Akihiko Sagara, Hiroki Yabe, Xubin Chen, Brecht Put, Thomas Hantschel, Maarten Mees Hidekazu Arase, Yukihiro Kaneko, Akira Uedono, Philippe M. Vereecken, Pore Structure Analysis of Silica-Gel Solid Nanocomposite Electrolytes with Surface

Conduction Enhancement, 236th ECS Meeting, A02-0075 (2019).

17. Akihiko Sagara, Simon Hollevoet, Brecht Put, Nouha Labyedh, Hidekazu Arase, Yukihiro Kaneko, Maarten Mees, Philippe M. Vereecken, Direct Measurement of Enhanced Ion Conductivity at the Thin-Film Ionic Liquid Electrolyte (ILE)/SiO2 Interface, The 60th Battery Symposium in Japan, 3G20 (2019).

18. 矢部裕城, 相良暁彦, 村田充弘, 荒瀬秀和, 富山盛央　メソポーラスシリカ複合ゲル電解質におけるマグネシウムイオン伝導の検証, 化学工学会 第 85 年会　K206　(2020).

19. 相良暁彦, ゾル-ゲル法によるナノコンポジット電解質の開発とその応用, 日本ゾル-ゲル学会 第 17 回セミナー　(2020).

20. Fanny Bardé, Xubin Chen, Knut. B. Gandrud, Brecht Put, Akihiko Sagara, Hiroki Yabe, Mitsuhiro Murata, Hidekazu Arase, Yukihiro Kaneko, Julian Steele, Maarten Roeffaers, Maarten J. Mees, Philippe M. Vereecken, Mechanism of Conduction in the Novel Nano-Solid Composite Electrolytes with High Li-Ion Conductivity, Pacific RIM meeting on electrochemical and solid state science (PRiME) 2020, A05-0960 (2020).

Patents

1. Xubin Chen, Philippe M. Vereecken, Maarten Mees, Knut. B. Gandrud, Mitsuhiro Murata, Akihiko Sagara, Yukihiro Kaneko, Morio Tomiyama, Mikinari Shimada,

SOLID ELECTROLYTE, ELECTRODE, ELECTRIC POWER STORAGE ELEMENT, AND METHOD FOR MANUFACTURING SOLID ELECTROLYTE, WO2019/088196 A1, 09.05.2019

2. Philippe M. Vereecken, Maarten Mees, Knut. B. Gandrud, Akihiko Sagara, Mitsuhiro Murata, Yukihiro Kaneko, Morio Tomiyama, Mikinari Shimada, SOLID ELECTROLYTE, ELECTRODE, ELECTRICITY STORAGE ELEMENT AND METHOD FOR PRODUCING SOLID ELECTROLYTE, WO2019/088197 A1, 09.05.2019

3. Philippe M. Vereecken, Knut. B. Gandrud, Maarten Mees, Akihiko Sagara, Mitsuhiro Murata, SOLID ELECTROLYTE, ELECTRODE AND CAPACITOR ELEMENT, WO2019/239631 A1, 19.12.2019

Acknowledgements

First and foremost, I would like to thank my principal supervisor, Prof. Dr. Yukiharu Uraoka, for his guidance throughout my doctoral course. He illuminated the path to a Ph.D. degree with appropriate guidance for me.

I would like to thank my supervisors, Prof. Dr. Mutsunori Uenuma, Prof. Dr. Tsumoru Morimoto, and Prof. Dr. Hideaki Adachi, for their critical advice and valuable suggestions for refining this dissertation.

I would like to express my sincere gratitude to Prof. Dr. Philippe M. Vereecken and Prof. Dr. Akira Uedono for in-depth discussions on my research and their passionate guidance in publishing research papers.

I would like to express my greatest appreciation to Mr. Hiroki Yabe, Mr. Mitsuhiro Murata, Dr. Xubin Chen, Dr. Knut B. Gandrud, Dr. Brecht Put, and Dr. Thomas Hantschel for their assistance with experiments, sharing of results, and engaging discussion. The time spent together in both the laboratory and in the office was a source of happiness.

I am deeply grateful to Dr. Yukihiro Kaneko, Dr. Hidekazu Arase, Mr. Morio Tomiyama, Mr. Mikinari Shimada, and Dr. Maarten Mees for their general support and warm encouragement.

I would like to offer my special thanks to Dr. Maarten Debucquoy, Ms. Nathalie Hendrickx, Mr. Nick Clerckx, Ms. Christine de Nooijer, Ms. Megumi Matsuyama, and Mr. Takashi Kozaki for their experimental support and productive discussions.

I would like to give heartfelt thanks to Dr. Hidekazu Ichikawa, Dr. Alfonso Sepulveda, Dr. Jos F. M. Oudenhoven, Mr. Simon Hollevoet, Ms. Nouha Labyedh, Dr.

Louis De Taeye, and Ms. Eva Vandaele for their enormous contribution to the imec-Panasonic collaboration project.

I wish to thank the ESTORE group members in imec for offering heartwarming friendship and an irreplaceable experience.

I would like to acknowledge my great debt to Dr. Eiji Fujii and Dr. Masa-aki Suzuki for giving me the opportunity to start this research in Belgium.

I am indebted to Ms. Yukiko Morita and all the staff of NAIST for their professional support in my office work.

Last but not the least, words cannot express how grateful I am to my wife, Mami, and my daughter, Saki, for their moral support. Without their continuous support and persistent help, this dissertation would not have been completed. I appreciate what they have done for me. I give my deepest love for them, with all that I am.

September, 2021

Akihiko SAGARA